

Technical Supplement to the LIGO Construction Proposal (1989) May 1993

The technical basis for LIGO is described in the proposal to NSF entitled, "The Construction, Operation and Supporting Research and Development of a Laser Interferometer Gravitational-Wave Observatory (LIGO)," dated December 1989. LIGO was approved for construction by the National Science Board in May 1990. This document is intended to supplement the December 1989 proposal (referred to in this document as "the Proposal") with current descriptions and development status of several technical topics selected by NSF for in-depth review. These topics are:

- A. Lasers and Input Optics
- B. Interferometer Topology and Control Systems
- C. Optics
- D. Seismic Isolation and Suspensions
- E. Vacuum System
- F. LIGO Systems and System Integration

Management Plan Context

An in-depth review of the organization and management of the LIGO Project took place in November 1992. Selected key elements of these topics are provided here in order to provide context for the June 1993 technical review.

Work Breakdown Structure (WBS)

The attached WBS (Fig. 1) is identical to that provided in the Proposal, Volume 2, Fig. VI-1 (p. 79); the definitions of the WBS elements are provided there, beginning on p. 78. WBS elements 1100-1700, 2100-2400, and 3100-3400, which account for the buildings and major vacuum system components of LIGO, will be implemented by industrial contractors, as discussed in the Proposal (Volume 2, Section VI-D "Subcontracting Plan," p. 84 ff.). The remaining tasks will be implemented by the LIGO in-house team, concurrent with project R&D activities.

Organization

The relationships between the LIGO project and various reporting/oversight mechanisms is illustrated in Fig. 2a; the internal LIGO organization is illustrated in Fig. 2b. The LIGO organization and responsibilities are described in the Proposal, Volume 1, Section IX (p. 90) and Volume 2, Section VI-B (p. 80). Planned organizational enhancements are shown in Fig. 2b. Positions for a Deputy Director, Project Scientist and Deputy Chief Engineer have been added. Referring to the Proposal, Volume 2, Fig. VI-2 (p. 81) and Fig. 2b, the Instrumentation and Data Systems Manager position has been replaced with the Data and Control Group. The Facilities, Vacuum Equipment, Beam Tube and Interferometer Development functions will be consolidated into a Facility/Equipment Group; subcontracts and financial management functions have been consolidated into an Administrative Group; and optical, mechanical, electronics and computer support functions will be consolidated into an Engineering Support Group. Recruitment for a Deputy Chief Engineer and a Data and Control Group leader is underway. The leaders of the remaining functional groups are expected to be appointed from within the existing staff after the above key positions have been filled.

Research and Development Work Plan

A flow plan for the LIGO R&D activities is shown in Fig. 3. The center line of the figure represents integration of the output of various R&D activities into the LIGO interferometer baseline design; the nodes labeled 11, 12, 13, & 14 represent adoption and integration of baseline functionality for principal LIGO interferometer technologies (pre-stabilized lasers, optical topology, vibration isolation, and test masses and suspensions, respectively). The nodes labeled 21-24 represent adoption and integration of advanced developments in these same areas. The ordering of the nodes is not critical (except that 2x must come after 1x, since an "advanced" version must by definition follow, and utilize the experience gained from, an earlier version), but all R&D needed to fulfill the functions denoted by nodes 1x is required before the design freeze of the initial LIGO interferometers. If advanced technologies become available from the R&D program before the design freeze, they will replace earlier technologies in the initial interferometer baseline design. The LIGO strategy is to freeze the design of the initial interferometer, based upon technology then in hand, about two years before the facilities are ready for occupancy. This will allow us to build the first interferometer and

install it at the earliest possible time, yielding the earliest information about the behavior and properties of a 4 km interferometer.

Construction of LIGO Facilities

A summary flow plan is shown in Fig. 4. Site development, facility design and construction, and beam tube and vacuum equipment design, fabrication and installation are represented for each of the two LIGO sites (WBS elements 1100–1700, 2100–2400, 3100–3400). The flow plan displays the principal activities and their precedence relationships. The upper part of the figure reflects planned activities for the LIGO site at Hanford, WA, while the lower part shows activities at the Livingston, LA LIGO site. Site investigations, land acquisition and environmental assessments are underway at both sites, and the subcontract for beam tube design and qualification testing is expected to be awarded shortly.

Schedule

The current master schedule for LIGO facilities construction and initial interferometer integration is shown in Fig. 5.

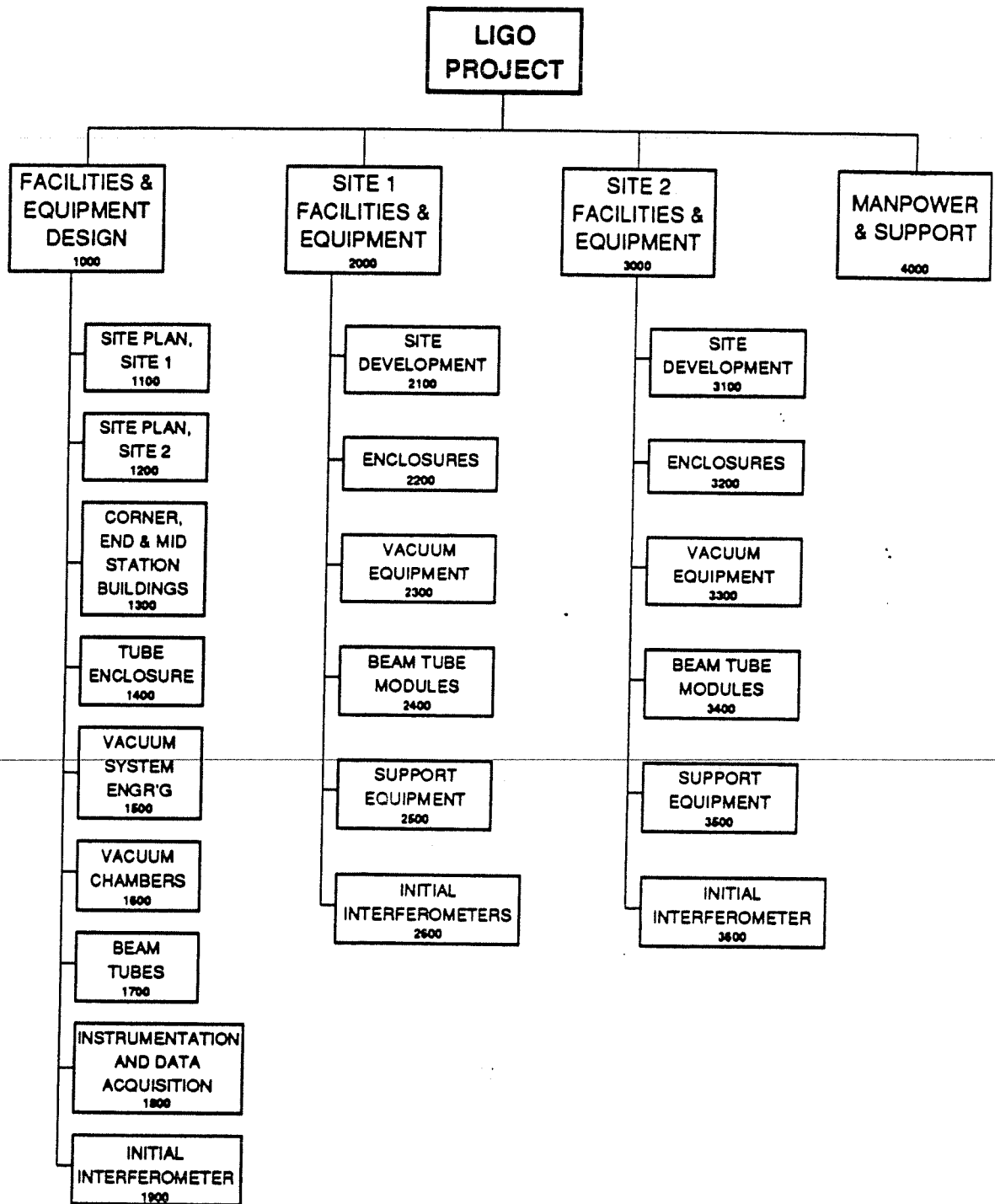


Figure 1. LIGO Work Breakdown Structure

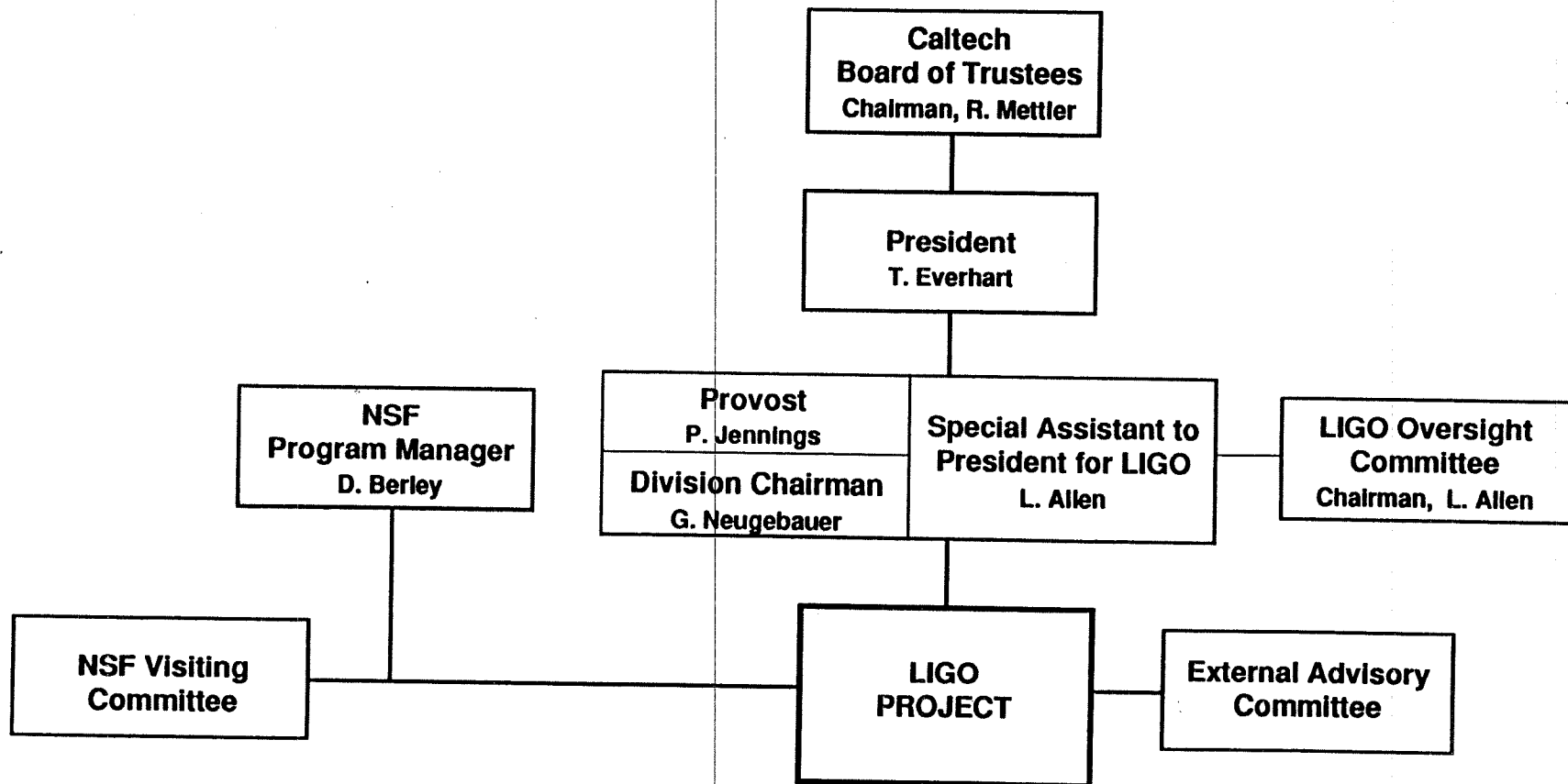


Figure 2a. LIGO Organizational Relationships

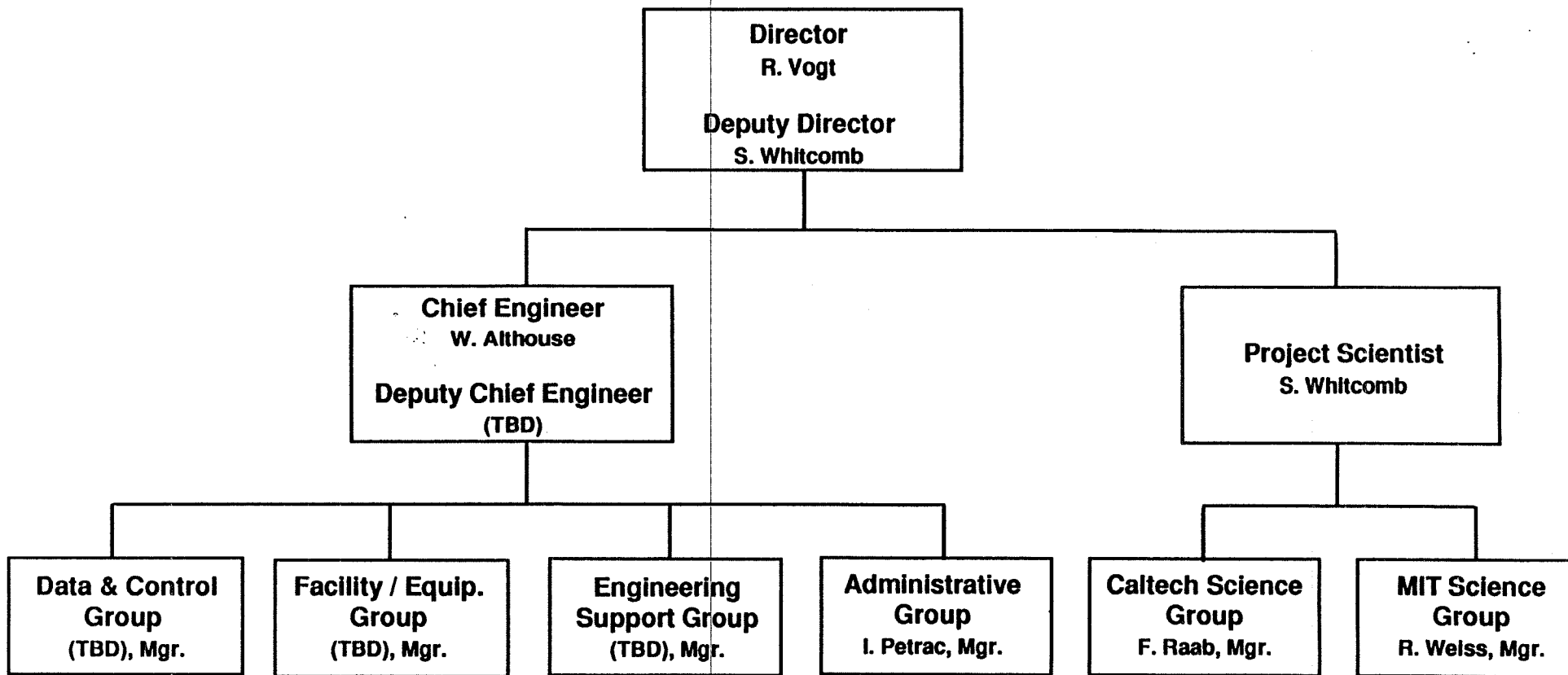


Figure 2b. LIGO Organization

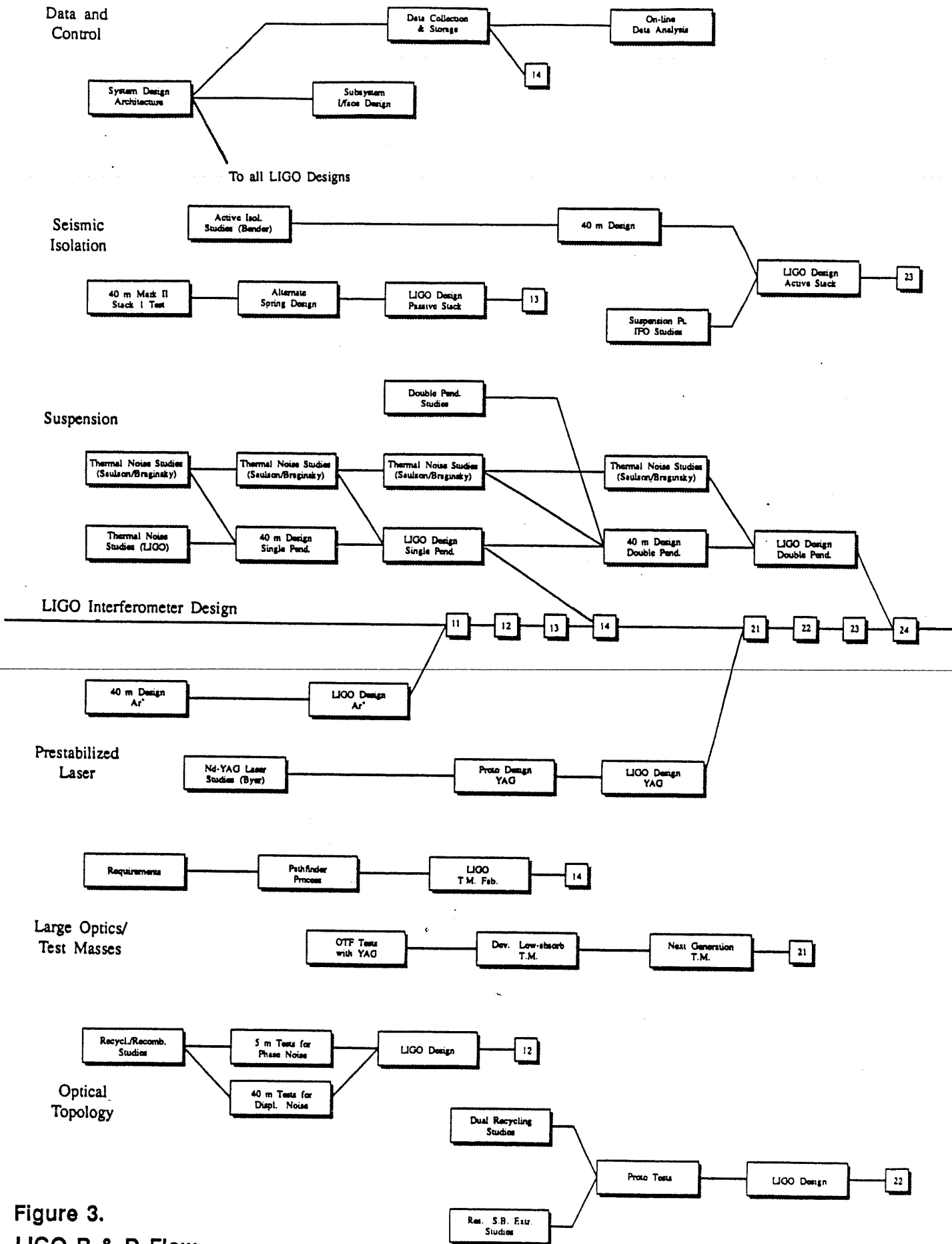


Figure 3.
LIGO R & D Flow

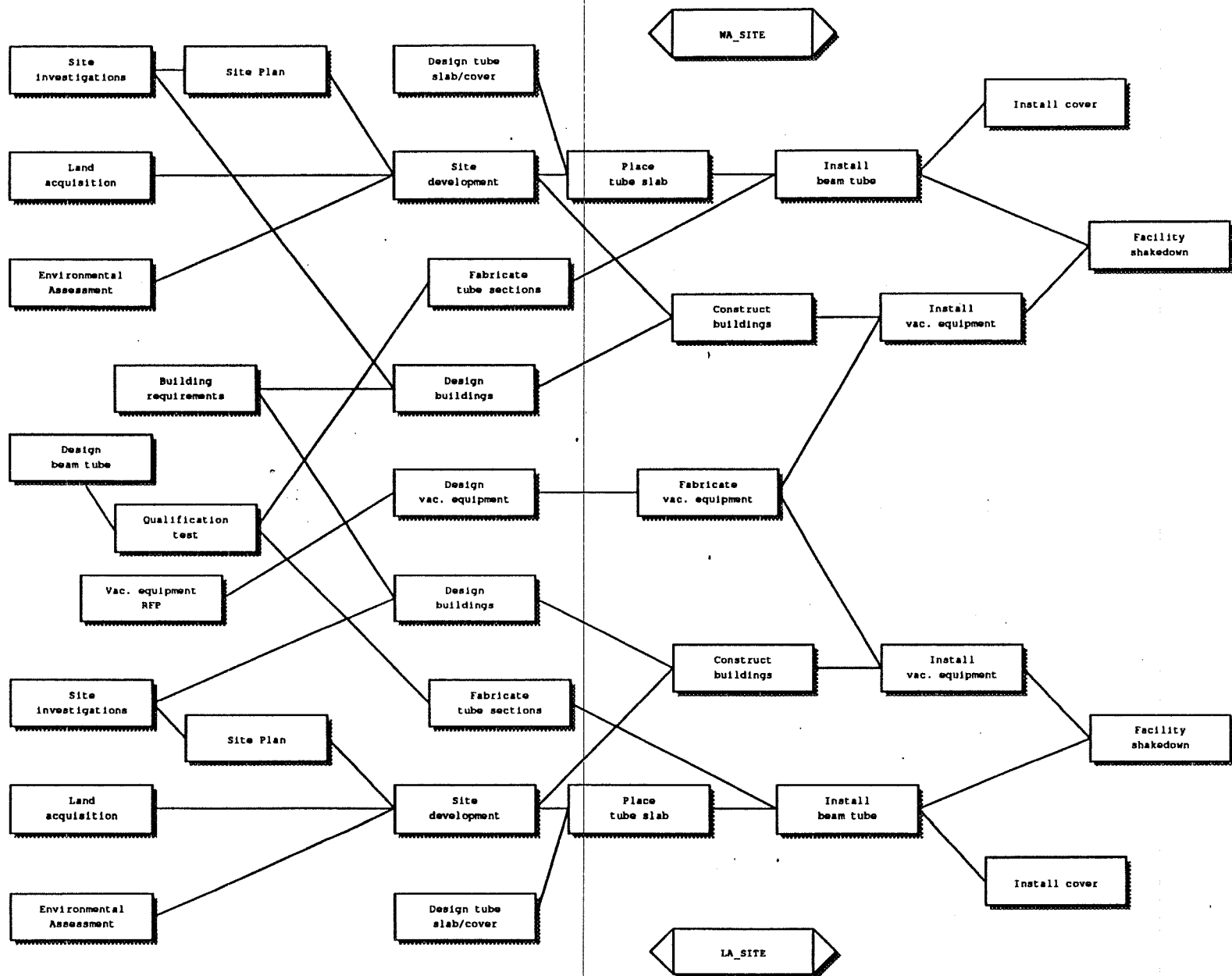


Figure 4. LIGO Facilities Design / Construction Flow

LIGO PROJECT SCHEDULE

5/93

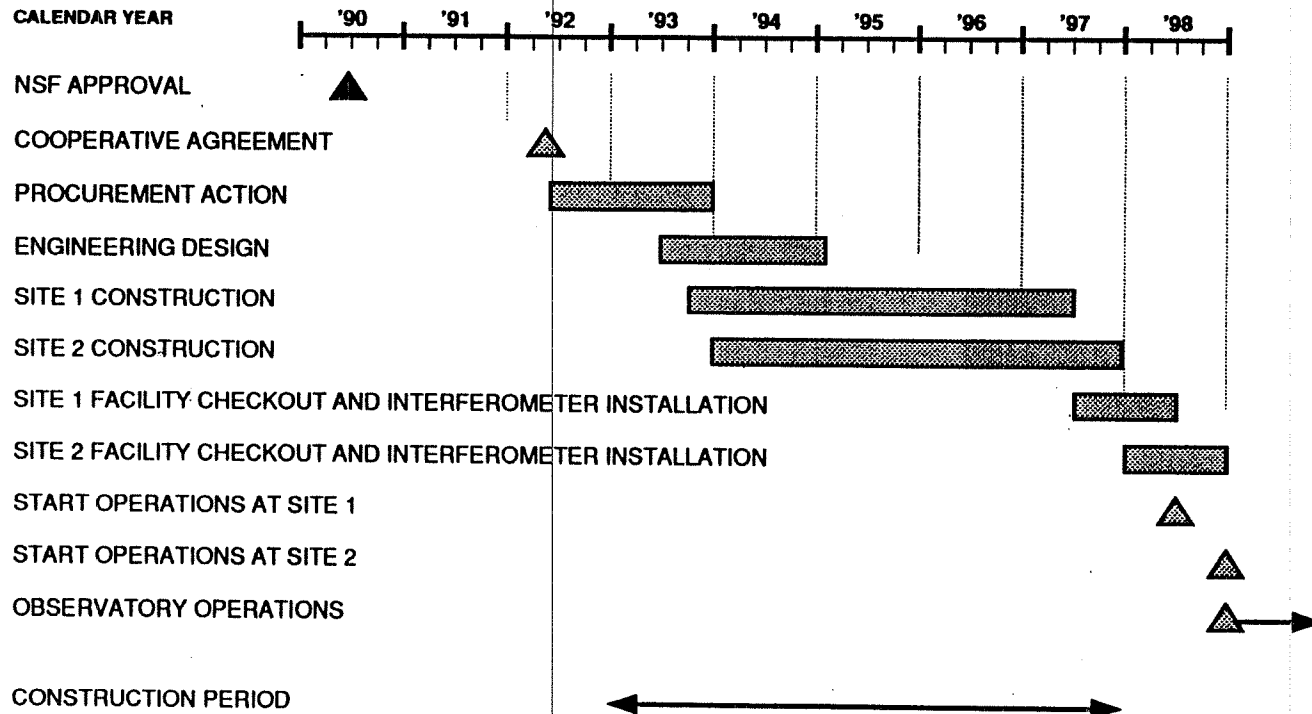


Figure 5



Lasers and Input Optics

Introduction

The noise budgets of the early and advanced LIGO interferometers are shown in the Proposal, Volume 1, Figures V-3 (p. 48) and V-4 (p. 56). The Input Optics Subsystem is designed to present a filtered, stabilized light beam to the interferometer. Fluctuations in the beam that might produce noise in the interferometer output must be suppressed well below the total noise from other sources shown in the figures. The input light for initial interferometers will be generated by commercial high power Argon ion lasers; advanced interferometers will use high power Nd:YAG lasers currently under development. The light must be stable in frequency, intensity and geometry. Frequency and intensity stabilization has been achieved in prototype interferometers at a level compatible with the requirements of the initial interferometer, while demonstration of spatial stabilization at this level awaits testing of a newly constructed mode cleaner.

This note gives the requirements on the light, describes the designs chosen to meet those requirements, and summarizes the progress to date.

Input Light Requirements

This section discusses the requirements on the light at the initial interferometer input.

Input Light Power

The accuracy of an optical phase measurement at the interferometer output is limited by statistical fluctuations or shot noise in the photon detection. The design output power of the input optics is approximately 3 W; after inefficiencies in the subsequent optics and in the photodetection, this power (at the design wavelength of 514 nm) results in the strain-equivalent shot noise shown in Figure V-3 (Proposal, Volume 1, p. 48).

Input Light Stability

Temporal fluctuations in the beam incident on the interferometer affect both cavities and cancel to first order; thus the following noise sources appear in second order, coupled to mismatches between the cavities. The design goal is to suppress associated noise below the shot noise limit.

Frequency Noise Variations in the light frequency $\Delta\nu$ result in strain noise Δh proportional to a mismatch in τ , the cavity storage time of the interferometer arms:

$$\Delta h \sim \left(\frac{\Delta\tau}{\tau}\right) \left(\frac{\Delta\nu}{\nu}\right)$$

The storage times will be matched to 1%; the corresponding requirement on frequency stability (in terms of $\nu(f)$, the amplitude spectral density of frequency fluctuations) is

$$\nu(f) < 6 \cdot 10^{-7} \text{ Hz}/\sqrt{\text{Hz}} \text{ at } 100 \text{ Hz for the initial interferometer.}$$

Spatial Fluctuations Fluctuations in the angle, lateral position, or diameter of the beam incident on the interferometer register as frequency fluctuations. These spatial fluctuations correspond to a small admixture of high-order resonant modes of the interferometer arms. The degree of admixture is characterized by ϵ , the summed amplitude of the higher order modes. A finesse of ~ 200 for the LIGO cavities and the requirement on frequency noise gives

$$\epsilon(f) < 2 \cdot 10^{-6} / \sqrt{\text{Hz}} \text{ at } 100 \text{ Hz for the initial interferometer.}$$

Intensity Noise The interferometer arms may not be in perfect resonance with the input light, due to slow motion of the test masses and limited servo gain. The mismatch in resonance, in terms of departures x_0 from the length corresponding to perfect resonance, couples to intensity fluctuations $\Delta I/I$, resulting in equivalent displacement noise

$$\Delta x \sim (\Delta I/I) x_0$$

With $x_0 \sim 1 \cdot 10^{-13} \text{ m}$, typical for the prototype, we have the requirement

$$I(f)/I < 4 \cdot 10^{-7} / \sqrt{\text{Hz}} \text{ at } 100 \text{ Hz for the initial interferometer.}$$

$$\text{BS } x_0 \approx \frac{2(\text{BN})}{2(\text{BAN})} (1 \cdot 10^{-13}) \leq 1.3 \times 10^{-11} \text{ m}$$

Input Optics Development for Initial Interferometer

This section discusses the plans to achieve the above requirements with a prestabilized Argon ion laser and mode cleaner. The prestabilized laser system has been built and tested. The mode cleaner is close to final assembly.

Figure A1 shows the input optics layout. The laser output is stabilized in frequency and intensity ("pre-stabilized") and is directed through the mode cleaner for spatial filtering. A Faraday isolator inhibits resonant parasitic coupling of the two systems. Photodiodes provide control signals for locking the laser to the mode cleaner and for stabilizing the mode cleaner output power.

The optical components (including Pockels cells, polarizing beam splitter, quarter and half-wave retardation plate, mode-matching lenses, and alignment mirrors) have been tested for optical performance at the necessary power and beam size and have been demonstrated to have adequate power handling capability, transmission and aperture.

Prestabilized Laser

The Argon ion laser (nominally 20 W output, all lines) produces a 5 W single line, single mode beam of 514 nm wavelength. The commercial unit has a line width of ~ 1 MHz, due mainly to mirror vibration caused by turbulence in the water cooling lines. These perturbations also cause beam jitter and intensity noise. The passive stability is improved by mounting the laser mirrors on a high mass optical table; vibration isolation of the laser body from the table is provided with a lead-rubber stack.

Significant further stabilization is achieved with active feedback to the laser mirrors. Fig A2 shows a block diagram of the Argon laser pre-stabilization system. Approximately 10% of the beam power is directed to a reference cavity. The laser frequency is then compared with a resonant frequency defined by the stable length of a quartz spacer between the reference cavity mirrors. The reference cavity is isolated from vibration and housed in a vacuum chamber.

The phase difference between the laser light and the light stored in the reference cavity, measured by photodiode PD1, is minimized by control of the laser beam frequency and phase: the frequency is controlled by piezoelectric displacement transducers on the laser cavity mirrors, and the phase by Pockels cell PC1. The resulting frequency fluctuation is $\nu(f) \leq 1 \text{ Hz}/\sqrt{\text{Hz}}$ at 100 Hz. Trim of the frequency and phase is provided by photodiodes monitoring the

resonances in the mode cleaner and in the interferometer arms, which provide phase references of much higher accuracy than the reference cavity. Together, the three servo paths are designed to reduce $\nu(f)$ to the required level.

The measured intensity variation is $I(f)/I \leq 3 \cdot 10^{-5} / \sqrt{Hz}$ at 100 Hz. Use of an acousto-optic modulator to provide amplitude stabilization is expected to reduce this variation by a factor of 100 or more.

The beam jitter parameter ϵ has been measured at the laser output. We have $\epsilon(f) \sim 1.5 \cdot 10^{-4} / \sqrt{Hz}$ at 100 Hz, corresponding to a maximum lateral displacement of 10^{-6} m. This variation is further reduced by the mode cleaner to well below the initial interferometer requirement.

Mode Cleaner

Fig. A1 shows the layout of the mode cleaner, which reduces spatial fluctuations in the laser beam at all frequencies, and frequency and intensity fluctuations at frequencies above the mode cleaner bandwidth (8 kHz). Light from the prestabilized laser is injected into a 12 m long, triangular cavity. The free spectral range is 12 MHz to allow the phase modulation sidebands to be transmitted. This allows the modulation Pockels cell to be placed before the mode cleaner so that noise associated with the electrooptic modulation is filtered. The ring geometry establishes a directional sense to the light propagation, improving spatial isolation. The mode cleaner mirrors are suspended from individual isolation stacks to reduce seismic and acoustic excitations. Control and damping of the mirrors are provided through affixed magnets. The frequency error between the incident light and the mode cleaning cavity resonance is fed back to the prestabilized laser to further reduce the frequency noise.

The suppression factor for the amplitude of the non-fundamental modes is determined by the choice of mirror reflectivity and the ratio of mirror radius to mode cleaner length. A reflectivity of 0.998 for the flat mirrors limits the cavity circulating power to < 2 kW, ensuring freedom from distorting thermal effects. We expect an amplitude attenuation >1000 for most non-fundamental modes.

Future Development and Plans

Continued Development for Initial Interferometer

The pre-stabilized laser has been tested as the light source for the 40 m prototype interferometer. Frequency and amplitude stability are compatible with the initial interferometer requirements.

The 12 m mode cleaner is close to final assembly. In the next several months we expect to measure its performance by measuring beam jitter at input and output and the associated frequency noise. It will then be tested in operation on the 40 m interferometer.

Development of Solid-State Laser for Advanced Interferometer

The strain-equivalent shot noise level of the advanced interferometer (Proposal, Volume 1, Figure V-4, p. 56) requires 60 W input light power. A collaboration has been established between LIGO and the Byer research group at Stanford University to develop a solid-state laser suitable for use with the advanced interferometer. The following describes their work.

10 W laser As a first step, the Stanford group is constructing a 10-watt, TEM_{00} , single-axial-mode, diode-laser-pumped Nd:YAG laser, with the power, frequency and amplitude stability and spatial mode properties necessary for the initial interferometer. This laser has been designed with the potential to operate at 10% electrical efficiency and to scale to greater than 100 watts of optical power. Stable, single-axial-mode, unidirectional oscillation will be obtained by injection locking the high-power slave laser with a low power (300 mW) diode-laser-pumped nonplanar ring oscillator (NPRO) master laser. The output of the 10-watt laser will then be frequency doubled with greater than 50% conversion efficiency in a monolithic resonant harmonic generator to produce 5 watts of green light with the same temporal coherence as the injecting NPRO laser. The amplitude, phase and beam wobble noise of the frequency doubled laser will then be characterized.

The laser pump system consists of 60 one-watt laser diodes, coupled to the active medium by optical fibers. This arrangement reduces the brightness of the pump source, but also leads to a simplified diode mounting system. It also allows

the replacement of a failed pump diode while the solid state laser is operating and so makes possible a laser design that is very reliable and maintainable.

The most important consideration in building a diode-laser-pumped, solid-state laser is efficient use of pump radiation. Colinear longitudinal pumping, otherwise known as end pumping, uses pump radiation very efficiently since the overlap between pump and signal beams can be excellent. However, end pumping suffers from a very important limitation: it requires a high brightness pump. Non-uniform side pumping is used in the design due to the low brightness of the fiber-coupled pump source, and a rectilinear geometry reduces thermally induced depolarization losses.

Experiments have demonstrated 7.7 W of output power for an input power of 50.4 W (31.4 W available out of the fiber bundle). The output has been measured to be linearly polarized with an extinction ratio of at least 100:1. The laser spot size, measured using a razor blade scan, shows that the output beam is close to diffraction limited, astigmatic, and elliptical, as expected.

100 W laser Work toward building a diode-laser-pumped laser to meet the requirements of the advanced interferometer is underway. A 100 watt, single-axial-mode Nd:YAG laser is being built under DARPA support. In the design of such a high-power, cw, solid-state laser, thermal management is the most critical design issue. The construction of several lower power lasers between 10 and 50 watts is planned before the building of the 100 watt laser. Injection locking will be used to provide single frequency operation of the high power oscillator. The 100 Watt laser will be pumped with fifty 15 watt Spectra Diode Labs (SDL) diode lasers coupled through optical fibers. Collaboration with SDL on the development of these pump laser packages has taken place over the last two years and at the current production rate the first 25 lasers are expected by June 1993. This laser has high enough gain so that an unstable resonator is possible, making good power extraction possible. The output will be spatially filtered and frequency doubled in an external resonant cavity with a projected conversion efficiency of 70%.

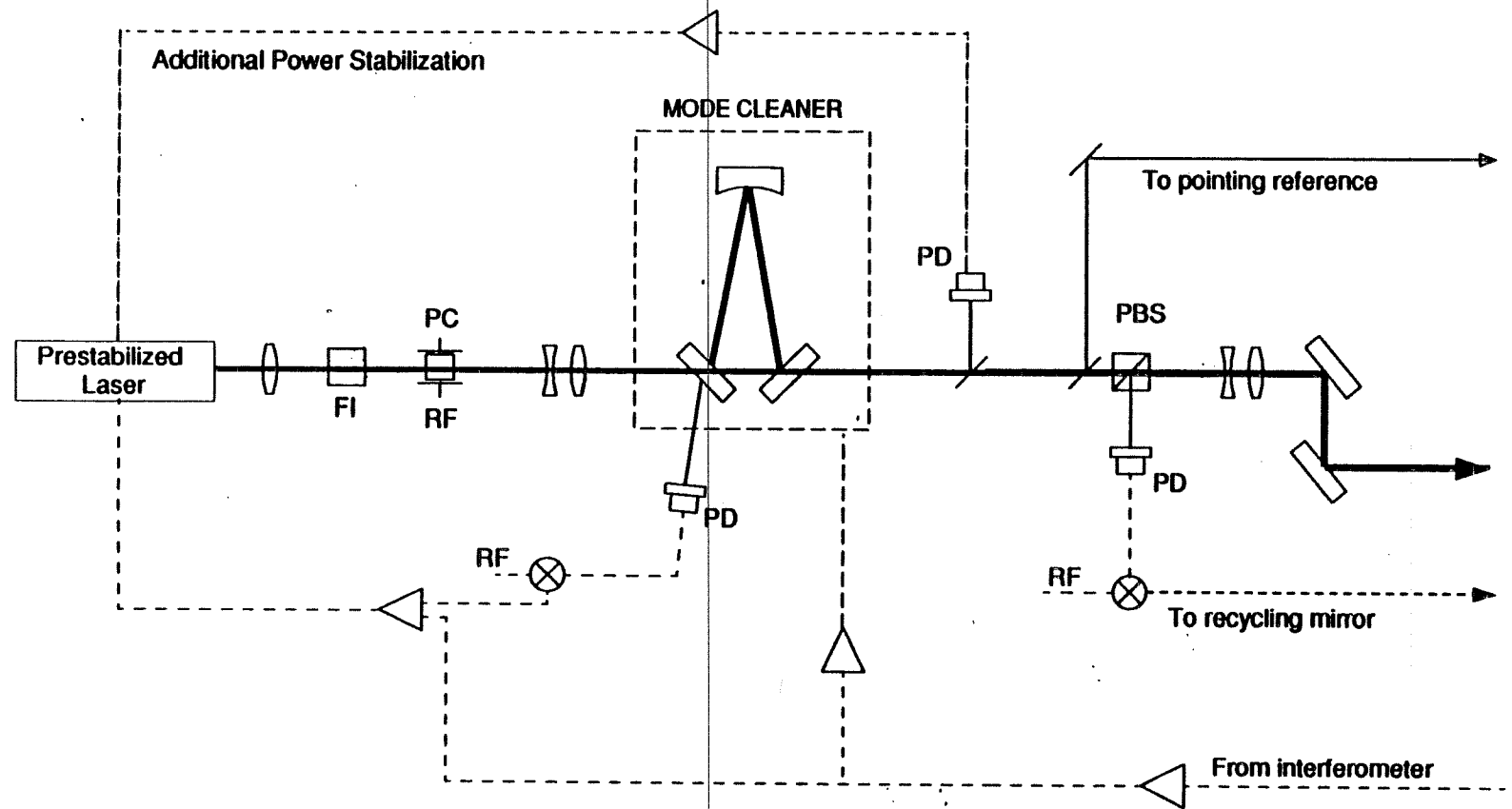
Harmonic Generation The goal of frequency doubling high power cw Nd:YAG lasers efficiently, using resonant harmonic generation, is being pursued. This involves placing the doubling crystal inside an optical resonator that multiplies the pump power.

The results of earlier investigations on external cavity doubling have shown the importance of low loss mirrors and nonlinear materials. Previously, the highest efficiency, high power CW doubling obtained was 36% with a doubled output of an 18 Watt injection locked, lamp pumped Nd:YAG laser to 6.5 Watts of TEM_{00} , single frequency, 532 nm radiation.

Recently a lithium borate crystal with reduced losses was obtained. This resulted in 5.8 W of 532 nm output for 11.5 W of 1064 nm incident power, for a conversion efficiency of 50.4%. The doubling cavity has operated for several hundred hours with no loss of conversion efficiency or degraded spatial mode quality in the harmonic beam.

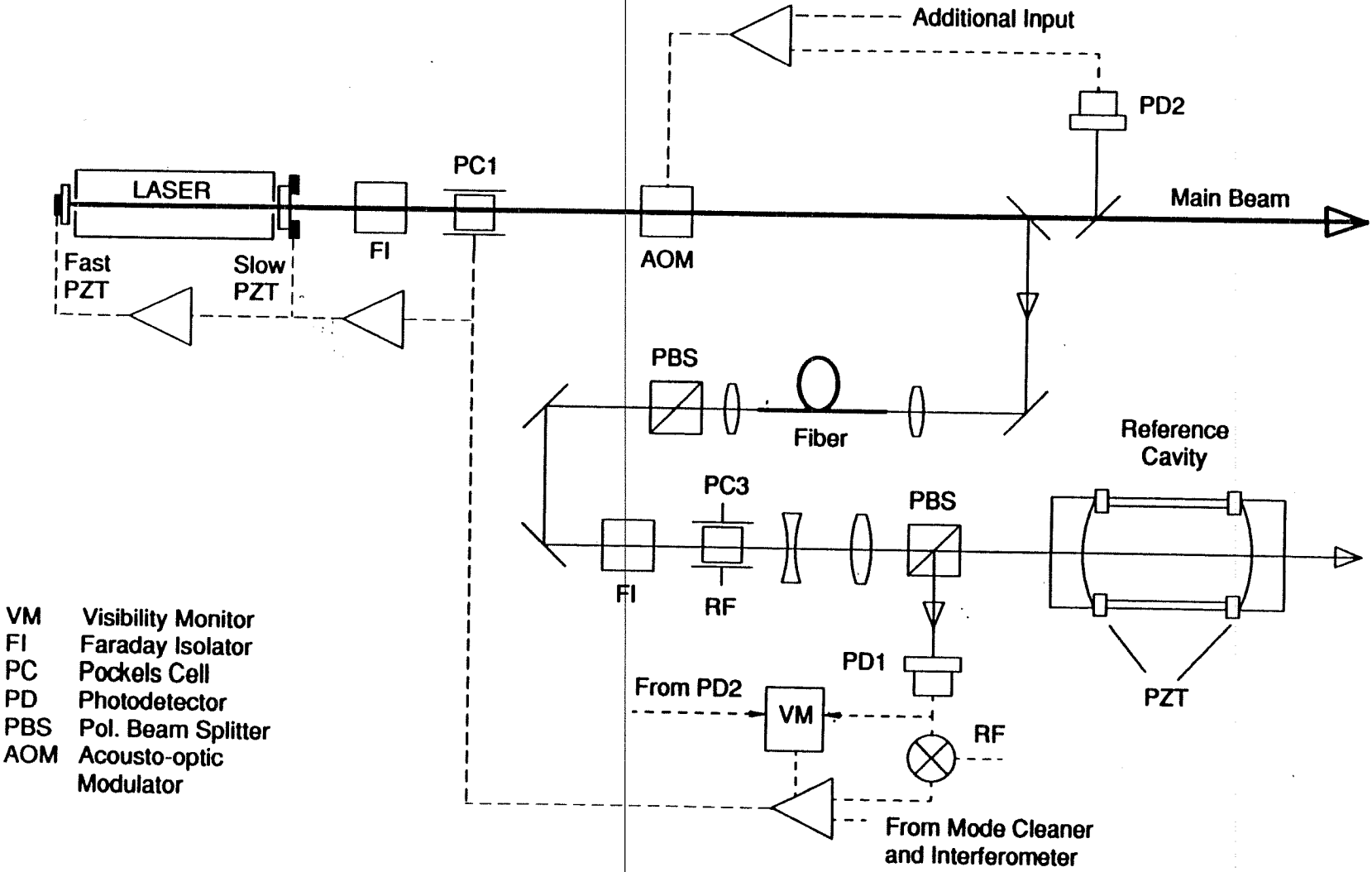
Center for Nonlinear-Optical Materials The development of solid-state lasers for LIGO will benefit from the establishment of the Center for Nonlinear-Optical Materials (CNOM) at Stanford University. The goal of CNOM is to support research on the development of nonlinear optical materials. CNOM will establish a Facility for optical materials characterization to improve and standardize measurement of nonlinear-optical materials. The CNOM Optical Materials Characterization Facility will have the flexibility to handle a wide range of optical samples including mirrors, phase modulators, optical isolators, beamsplitters, solid-state laser media and nonlinear optical crystals.

FIGURE A1 LIGO INPUT OPTICS LAYOUT



- FI Faraday Isolator
- PC Pockels Cell
- PD Photodetector
- PBS Pol. Beam splitter

FIGURE A2 PRESTABILIZED LASER



Interferometer Topology and Control Systems

Introduction

This section describes the LIGO interferometer optical layout and the control systems needed to maintain the interferometer at the correct operating point. These include length control (holding an optical cavity on resonance) and alignment (holding a cavity optic axis co-linear with its input beam). Length and alignment control systems are designed to operate nearly independently of each other. Imperfections in the alignment may allow the alignment system to inject excess noise into length controls, although they do not affect the control systems' stability or dynamics. We treat control of alignment and length independently, with the requirement that the alignment system be configured so that it does not induce excess noise in the interferometer length.

Interferometer Length Control

The concepts for the interferometric detection of gravitational waves are discussed in Volume 1, Sections II-A (pp. 5) and III-A (pp. 13), and Appendix B of the LIGO construction proposal. The initial LIGO interferometer optical configuration is shown in Figure B1: a Michelson interferometer, with suspended test masses which form Fabry-Perot cavities in the 4 km long arms, and with 'recycling' of the input light.

The recycled interferometer has four fundamental length degrees of freedom which must be controlled to keep the interferometer at its proper operating point: the lengths of the two Fabry-Perot cavities (L_A and L_B) and the lengths of the two Michelson arms measured from the recycling mirror (ℓ_A and ℓ_B). Gravitational waves induce differential motion in the two arm cavities ($L_A - L_B$), which is sensed at the output of the interferometer (the "antisymmetric port" of the beamsplitter). This sensor must achieve shot-noise-limited sensitivity at the full laser power listed in the LIGO specifications. A major challenge is thus to extract this and other signals, and apply the necessary feedback, without corrupting it with excess noise.

Optical path lengths are sensed by detecting the relative phase between laser beams as they are interfered. This phase is measured by inducing a

sinusoidal radio frequency phase modulation in one of the beams and detecting the interference with a photodiode. The photocurrent produced is demodulated at the modulation frequency and averaged; this process yields a nearly linear signal which, for small excursions from optimum, is proportional to the phase difference between the beams. The RF modulation technique is required to allow working at a "dark fringe" (destructive interference, which conserves circulating laser power inside the interferometer) and to circumvent intrinsic low-frequency laser intensity fluctuations. We refer to the entire ensemble comprising an RF modulating system (which is rather complex in some variants discussed below, and may be shared by multiple control loops), photodetector, and demodulator as a *sensor or readout* for each controlled degree of freedom.

The symmetry of the interferometer makes it convenient to describe the interferometer in a 'common mode–differential mode' basis, where the four sensed variables are the gravitational wave signal, the arm cavity common mode length, $((L_A + L_B)/2)$, the Michelson differential mode length, $(\ell_A - \ell_B)$, and the recycling cavity length $((\ell_A + \ell_B)/2)$. Since the feedback signals are used to control the positions of individual masses, the interferometer is intrinsically a multivariable control problem. Couplings between these four degrees of freedom vary according to the specific interferometer optical design.

Once we have the control requirements (usually specified as a maximum allowed rms deviation from an operating point and a maximum in-band noise in the controlled length) and the noise input $N(f)$ to the system (principally the seismically induced motion of the interferometer optical elements for the rms deviation and the sensor shot noise for the in-band noise), we can calculate the needed gain $G(f)$. Noise in the sensor or actuator electronics often places a limit on the gain to avoid introducing unintentional motion of the test masses at frequencies outside the control bandwidth.

Acquisition of the required operating state (referred to as "locking the interferometer") is an additional challenge for the control system design. In general, usable control signals are present only when the interferometer is in resonance. Since before acquisition the test masses will swing freely through distances 100 to 10,000 times the width of a cavity resonance, the control signals are correct for only a small fraction of the time. Important time constants are also a function of the interferometer state; for example, a pole in the optical phase transfer function of each arm cavity moves from 90 Hz to 5 Hz as the recycling mirror is brought

into resonance. Such features can demand unusually broad stability margins and dynamic reserves; separate compensation networks for acquisition and steady state operation are also needed, with automatic switching between modes.

The actuators planned for both interferometer length and alignment control are simple coils fixed to a mechanical reference and permanent magnets attached to the mirrors. Sets of coils working in unison will control lengths, while differential forces between coils will provide torques to the test masses and control angles. The mechanical characteristics of these actuators (maximum force, possible excitation of mechanical resonances) must be taken into account in the control system design.

Optical length control requirements

The control systems must maintain the optical components at the correct operating points, which can be summarized as follows (the main criterion, and the allowed RMS deviation it dictates, are listed in parentheses):

- Individual arm cavity lengths (resonance condition, 3×10^{-13} m)
- The Michelson path length difference (dark fringe, 3×10^{-2} rad)
- The recycling cavity length (resonance condition, 3×10^{-10} m)

In addition, we require that acquisition of the correct operating state be reliable and quick.

Candidate initial LIGO interferometer topologies

We are engaged in a research program to choose from a limited number of possibilities for the optical topology; we can break these choices down into two categories.

Gravitational-wave readout system: This is the main differential arm motion sensor. One scheme (asymmetry or Schnupp modulation, Figure B2-b) requires a difference in the distances ℓ_A and ℓ_B from the beamsplitter to the near mirrors of the arm cavities, which in conjunction with a phase modulation on the light input to the interferometer produces an effective modulation of the Michelson interferometer path length difference, and allows phase detection as described above. An alternative is to interfere the light from the antisymmetric interferometer port with a reference beam derived from the symmetric port in a parallel-beam

Mach-Zehnder interferometer which contains a phase-modulation element (Figure B2-a).

Auxiliary length control: The other three lengths do not influence the gravitational wave signal to lowest order, but must be controlled to maintain the proper operating point. One scheme for sensing these lengths uses the asymmetry mentioned above, as well as differences in the finesses (or optical Q) of the recycling cavity for the phase modulation sidebands and the carrier light, to develop error signals which are linear combinations of the desired quantities. An alternative scheme under study uses a frequency-shifted subcarrier which is chosen to probe only the front mirrors of the arm cavities; the subcarrier does not resonate with the 4 km arm cavities, and allows independent and sequential control over the two degrees of freedom associated with the cavity near mirrors and the recycling mirror.

Present status

The topologies sketched above have been analytically and numerically modeled, and both are capable in the locked state of meeting the requirement for sensitivity to gravitational waves. To verify the models, and to obtain information on acquisition and sensitivity to some imperfections, experimental prototypes have been constructed and are currently yielding results (for a more detailed discussion, see the attached reprints "Prototype Michelson Interferometer with Fabry-Perot Cavities" and "Demonstration of Light Recycling in a Michelson Interferometer with Fabry-Perot Cavities"). The mirror parameters and modulation/demodulation systems are those planned for LIGO, but the prototypes are built on optical breadboards with fixed (not suspended) test masses, and use piezoelectric mirror actuators instead of the electromagnetic ones described above. This allows these experiments to proceed rapidly without the complications of suspension and alignment and vacuum chambers. Comparison of measurements with model predictions for the relationship between component motion and sensor outputs has yielded good agreement. Various acquisition strategies have also been developed and tried.

Development Programs

Experimental study of phase noise: Prototype measurements to date have used circulating powers much smaller than those planned for the initial LIGO. It is important to gain experience with interferometers which make a shot-noise limited detection with the roughly 50 W of beamsplitter-incident optical power required for advanced interferometers. For this reason, we are starting a research project to investigate this high power, high phase sensitivity regime.

A 5 meter interferometer is being designed at MIT especially for this research. It will intentionally have limited position sensitivity, so that seismic motion of the mirrors will not contribute to the measured noise spectrum. This interferometer will use many of the optical and control techniques discussed above to attain this sensitivity, although it will not initially demonstrate the complete LIGO optical and control topology. Noise sources, such as scattered light, which become more important with increasing phase sensitivity will be investigated, as will technical developments such as high-power photodetection systems.

Prototyping the complete LIGO topology: An integrated test and demonstration of the complete topology and control systems is also planned. This requires an optical system which is topologically equivalent to the LIGO (although using a laboratory-scale interferometer requires some parameter modification). The 40 m prototype at Caltech will be used for this program. Ultimately, a similar optical system will be installed in the interferometer at MIT, giving useful information on scaling and noise characteristics.

Interferometer Alignment

Requirements and control systems

The angular orientation of the interferometer mirrors must be controlled to a high precision. For instance, to maintain the Michelson contrast and thus the recycling gain, the angles of the arm cavity mirrors must be held to 2×10^{-7} radian RMS. In addition, the beam must be correctly positioned on the optical components to minimize undesired mechanical coupling from angular rotations to motion along the beam axis (incorrect positions are a potential source of coupling between alignment and length; see the preprint "Mirror Orientation Noise in a

Fabry-Perot interferometer Gravitational Wave Detector”). The alignment control has only moderate gain and bandwidth requirements. This low bandwidth permits the alignment control signals to be strongly filtered out of the measurement band, preventing noise contamination of the length signals.

LIGO will use a hierarchy of sensor systems having successively higher sensitivities (and correspondingly less dynamic range) to bring the system from the misaligned state to normal low-noise operation. Initially, suspended mass motion is sensed by a set of local position detectors in five degrees of freedom. The resulting coarse alignment control has a large dynamic range and is effective at damping large motions. However, noise and long-term drift from local sensors will exceed operational requirements.

A more sensitive angular reference is derived from an optical lever. An auxiliary low-power laser beam is directed to the component to be sensed, and the reflection falls on a position-sensitive photodiode, giving signals proportional to the two critical angles of the component. These sensors can be used during lock acquisition and interferometer operation, but act as only secondary references; they do not sense the proper alignment, which must be initially set (and periodically refined) by iteration.

Local position detectors and optical lever sensors are well understood and have been successfully demonstrated in the suspended 40 meter interferometer. Initial LIGO sensitivity goals can be obtained using just these two types of control sensor, but the operational penalty of periodic, iterative readjustment of the reference alignment are highly undesirable. A third level of sensor, based directly on optimizing the match between interfering wavefronts, is under development.

This third-level alignment sensor (called *automatic alignment*) will allow continuous optimization of interferometer alignment, but only operates while the length control systems are locked. Second- and first- level systems are still needed for lock acquisition. Optical phase gradients of the light at various points will be sensed to derive information needed to align the mirrors. The same system can also optimize the matching of the beam waist size and position.

Automatic Alignment Development Program

The wavefront sensing technique has been modeled and successfully demonstrated on single Fabry-Perot cavities. When multiple cavities are coupled together, as in the LIGO interferometer, analysis of the system becomes more

challenging. The complexity of the analysis for coupled cavity systems has led to development of two modeling approaches.

One completely numerical model uses a Fourier transform wavefront propagation technique. A more intuitive model based on modal decomposition has also been developed. The perfectly aligned interferometer resonates in only the fundamental (TEM_{00}) spatial mode; any small misalignment of the mirrors can be described as an excitation of higher-order spatial modes (in particular the TEM_{01} and TEM_{10} modes). This model delivers the coefficients of excitation of the higher modes as a function of misalignment for simple and coupled cavities.

The two models agree for simple and coupled cavities. An experimental testbed, using fixed mirrors, has been assembled and has numerically verified the models for simple cavities. The test-bed is now configured to test the simplest coupled cavity arrangement (three mirrors in series). Future modeling for the alignment question will focus on the modal decomposition approach; it is currently being extended to situations with beamsplitters.

The experimental program will be transferred to the existing fixed-mass prototype of a complete LIGO interferometer for tests on more complicated optical systems. We will demonstrate a complete interferometer alignment on that testbed, and will also develop and test engineering solutions to the phase-front readout. Independently, a program to automatically align a simple cavity with suspended mirrors is underway to give experience with the dynamics of the suspended mirror in the control system. This will lead to an integration with one of the suspended-mass interferometers.

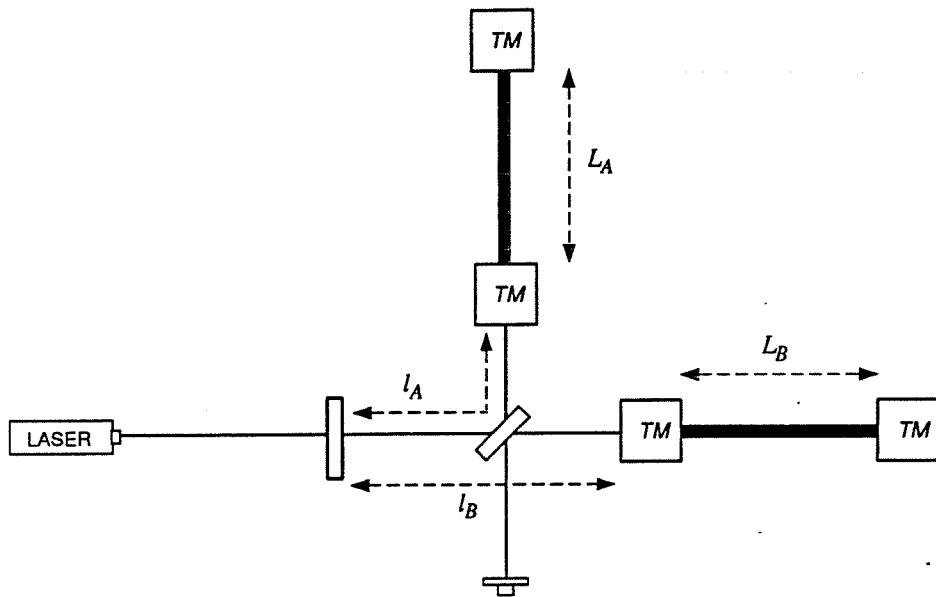


Figure B1 Basic recycled interferometer, showing the four independent optical lengths L_A , L_B , ℓ_A , and ℓ_B to be controlled.

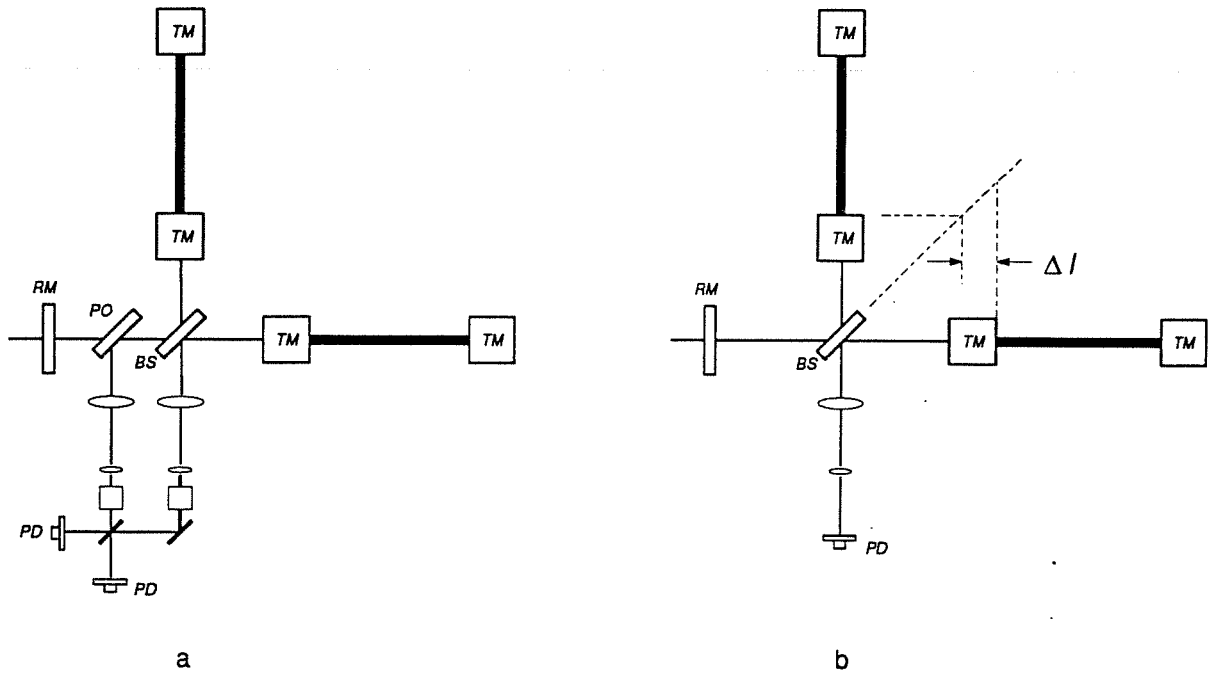


Figure B2 Candidate topologies for initial LIGO interferometer gravitational wave readout system. The Mach-Zehnder system, with its reference beam supplied by beam sampler *PO*, is shown in a. The asymmetry modulation variant, showing the deliberate offset Δl , is shown in b. In both diagrams *TM* denotes a test mass, *PD* a photodetector, *BS* the beamsplitter, and *RM* the recycling mirror.

Optics

Introduction

One of the most critical aspects of the LIGO design is the development of suitable optical components, and an active program in this area, starting with initial interferometer requirements, is underway. There have been substantive advances in our understanding and consequent changes in the design of several aspects of the LIGO, including the optical design. The initial LIGO interferometer is now planned to be a more robust and simplified configuration (compared with what was described in the Proposal) using external modulation and power recycling. The optical designs of the initial LIGO interferometers are based on direct experience with the suspended prototypes and on research in special purpose interferometers and ancillary test apparatus. Many of the optical components have been successfully operated at the required optical power and intensity. The development of optics for advanced interferometers will in large part be an extension of that for initial interferometers.

Since the Proposal was written, the specification of critical large diameter optics has been refined. A central issue in current research is the dimensional scaling of the optics. The beam sizes will change from 4 millimeters diameter in the 40 meter interferometer to 4 centimeters in the 4 km LIGO; the angles subtended by the beams will change from 50 microradians to 5 microradians. The increase in scale from laboratory interferometers to LIGO sets new limits on the permitted perturbations of mirror surfaces and coatings. The LIGO requirements are similar to those for high-quality low-scattering small optical telescopes, but carry the additional requirement of low loss.

An important issue is the control of scattered light from the interferometer, especially the small angle scattering from the cavity mirrors, which can interact with the vacuum system and introduce additional noise. (This topic is discussed in the Proposal, Volume 1, Appendix F.) The baffle design presented in the Proposal (Volume 2, Section IV-C-2-b-iii, p. 29) is the result of analytical calculations applied to simple models for scattering from optical components and beam tube walls. These calculations have been augmented by computer modeling of the

LIGO beam tubes and baffles and by measurements of scattering from the tube and from sample baffle materials. This research has confirmed the substance of the initial model and has shown additional margin in the current design of the baffles and beam tubes.

Optics for Initial LIGO Interferometers

An optical schematic diagram of the initial LIGO interferometer is shown in Figure C-1. The principal elements of the interferometer are the following:

- *Input optics subsystem:* Light from the pre-stabilized laser is conditioned by passing through a Pockels cell phase modulator, a Faraday isolator, a mode cleaning cavity (consisting of mirrors M_{TC1} , M_{TC2} and M_{TC3}) that passes the phase modulation sidebands, and beam expanding telescope (mirrors M_{T11} and M_{T12}).
- *Power recycling cavity:* The recycling cavity is comprised of M_{RC} and the front mirrors of the 4 km interferometer arm cavities, M_{11} and M_{21} . The cavity is resonant at the phase modulation sidebands and, when both arm cavities are resonant on the optical carrier, is also resonant at the optical carrier. With the interferometer held at a dark fringe at the antisymmetric port of the main beam splitter, the anticipated total loss due to absorption, large angle scattering, diffraction from large spatial scale wavefront distortion, birefringence and incomplete interference at the antisymmetric port is expected to be about 3–4%. With the transmission of M_{RC} chosen at this value the power circulating in the cavity is approximately 30 times the input power, and the entire interferometer reflects little power back to the laser.
- *4 km arm cavities:* The two cavities, made up of M_{11} , M_{12} and M_{21} , M_{22} , convert the gravitational wave metric perturbations into antisymmetric optical phase changes on reflection by the cavities. The cavity storage time (and thereby the gravitational wave frequency response of the interferometer) is determined by the input mirror (M_{11} and M_{21}) transmission, chosen to be 3% for the initial interferometer, giving cavity storage times of approximately 1 millisecond. The rear mirrors (M_{12} and M_{22}) have a high reflectivity. The two cavities are made as identical as possible to reduce sensitivity to laser frequency and amplitude fluctuations. Currently, the input mirrors are planned to be flat while the rear mirrors are polished to a 6 km radius. The cavity losses in the TEM_{00} mode are expected to be approximately 1%, dominated

by diffraction from large spatial scale wavefront distortions. The combined resonance of the arm and recycling cavity has a width of a few Hertz.

- Photodetector and matching optics: The photodetectors used in the prototypes and planned for the initial LIGO interferometer are discrete large area (1 cm^2) silicon photodiodes operated in a photoconductive mode. The photocurrent at the phase modulation sideband frequencies is detected. The detectors are oriented at the Brewster angle for Silicon; their quantum efficiency is approximately 0.8, and they are exposed to tens of milliwatts average power. The photodetection noise is dominated by the shot noise in the incident light.

The parameters for the initial LIGO interferometer, other than the size of the optics and the Gaussian beams in the main interferometer and the combined cavity width, are used in current laboratory research. The largest circulating power in the system is 4 kW, occurring in the arm cavities on resonance, while the greatest intensity, 70 kW/cm^2 , is developed in the mode cleaner cavity.

Optical Component Specification and Testing

Large diameter optics specification

Material: The large diameter optical components are fabricated from annealed high purity fused silica with a homogeneity better than 5×10^{-7} and an intrinsic birefringence less than 1 nanometer/cm. The arm cavity mirrors, which are the test masses, are 25 cm in diameter and 10 cm thick, with a mass of 10 kg. The main beam splitter and the recycling mirror have a thickness of 5 cm. Fused silica has been chosen for its small mechanical and optical losses. The dimensions of the test masses have been chosen to move the internal vibrational frequencies above 10 kHz to minimize thermal noise.

Modeling: The specification of large diameter optics is based on diffraction modeling and wavefront perturbation measurements on individual components. Analytic techniques have been developed to relate wavefront distortion—induced by imperfections such as mirror figure error, coating inhomogeneity and birefringence—to cavity loss and interferometer contrast defect. The analytic techniques are based on cavity modal field expansions excited by wavefront distortions expressed in terms of Zernike functions. The large aperture optical components are specified by the permitted wavefront distortions in terms of Zernike components and associated spatial power spectra. The analytic techniques have been validated by a numerical Fourier transport code.

Results of the modeling indicate that to maintain cavity diffraction loss and interferometer contrast defect to less than 1% will require that wavefront perturbations, expressed as Zernike amplitudes over the 25 cm optics, be less than $10^{-3} \lambda$ over an average of the components with radial indices between 8 to 25 and low angular order. In effect, over the region of the Gaussian beam diameter, the wavefront distortion induced per optical component must be less than $-\lambda/300$.

Research and development program

Measurement capabilities: Commercial Fizeau wavefront interferometers operated in environmentally controlled facilities have the capability to measure wavefront perturbations and, when suitably modified, the birefringence at the specified level. Measured wavefront perturbations, limited by errors in reference flats and uncontrolled thermal gradients, approach the required specification. Industrial fabrication and measurement capabilities appear to be close to meeting the requirements of the initial LIGO interferometer, but additional research in industrial capability is necessary.

Industrial pathfinder process: The project has acquired high grade fused silica test mass blanks as full scale samples for the initial LIGO interferometer. In the coming year, these samples will be polished to LIGO specifications by several vendors, and the wavefront distortions will be measured by an independent metrology laboratory. Concurrently, the substrate and coating absorption and scattering, as well as the substrate mechanical Q, will be measured in the LIGO optics test facility. The test mass samples will be coated with both high reflectivity and transmissive coatings by the ion beam sputtering techniques that have been used to make the low loss coatings used in the mirrors of the prototype interferometers. Currently, we plan to work with PMS (Boulder, Col.), the coating vendor that has made the prototype mirrors, to help them develop the techniques to improve uniformity over larger apertures. Later in the pathfinder process, we intend to develop this capability at other coating houses to avoid the potential difficulties of relying on a single vendor.

VIRGO/LIGO/industry cooperative research on coating technology: In recognition of the dependence of interferometric gravitational wave research on the industrial capability to make high quality coatings, the LIGO and VIRGO projects have joined in a cooperative program with PMS and the optical coating group at the University of Lyon to develop and test coating techniques.

Optical model of the interferometer: The optical modeling up to now has concentrated on the effect of wavefront distortions induced by imperfect optics in single cavities. The interferometer contrast defect and total loss has been inferred by statistical arguments. Research, to be completed in the coming year, will use the Fourier transport code to model the influence of imperfect optics in the entire initial LIGO interferometer.

Test of interferometry with LIGO beam diameters: Interferometry with beam diameters on LIGO scales will be part of the program to develop the electronic and optical instrumentation to attain the initial LIGO phase noise on the suspended 5 meter prototype.

Optical Testing

Special purpose optical test apparatus has been developed by LIGO to establish the properties of the optical components under power and intensity levels that will be encountered in the initial LIGO interferometer. The results of these tests include the following:

Power and intensity tests: Faraday isolators, acousto-optic modulators, and electro-optic modulators have been tested at 4 watts of optical power (beam diameters about 2 mm), and exhibit less than $\lambda/30$ wavefront distortion. This distortion is small enough to maintain good optical coupling efficiency into the mode cleaner cavity. Superpolished mirrors with high reflectivity PMS coatings have been incorporated into evacuated cavities and operated at a circulating power of 4 kW and incident intensity greater than 6 MW/cm². Upper limits on the loss degradation of the mirrors are less than 5 parts per million over 100 hours of exposure. At the maximum power and intensity of the initial LIGO interferometer, the mirrors show no evidence of thermal distortion.

Contamination and endurance tests: Mirror degradation proportional to the incident intensity and exposure time has been experienced in the contaminated vacuum system of the earlier 40 meter Mark I prototype. The project has an ongoing program to evaluate the possible mirror contamination from materials to be used in the LIGO vacuum system under controlled conditions. The test apparatus consists of high finesse evacuated cavities in which samples of the test material are placed in proximity to the mirrors. To date "Viton" and RTV elastomers, candidate materials for the vibration isolation stacks, have been tested

and show no degrading effects. In the future, tests of “Teflon” and vacuum compatible adhesives are planned.

Development of optical component measurement and screening facilities: In the next two years the project will enhance the capabilities in the LIGO optics test facility in several ways. The current apparatus to test contamination and total loss in the optics will be duplicated, and procedures will be automated to increase the measurement throughput. A wavefront interferometer operating at 514 nm will be acquired to characterize electro-optic modulators, Faraday isolators, and other small aperture optical components. At present, the project plans to continue testing large aperture optics with industrial facilities.

LIGO Vacuum System Optical Properties

The LIGO is being designed to carry out a long term program in gravitational wave research. Thus, the specification of the optical properties of the LIGO vacuum system is driven by the anticipated needs for the most sensitive gravitational wave interferometers. Among the most critical issues in planning the LIGO are the optical properties of the 4 km beam tubes and of the associated baffling. The beam tubes constitute one of the major costs of the facility, and would virtually be impossible to modify once the facilities are constructed. Consequently, most of the planning effort has gone into this, and less work has been done on the optical properties of the more accessible instrumentation chambers and associated tubing. Appendix F (Volume 1) of the Proposal presents an overview of the issues involved with stray light in the LIGO, based on earlier analysis. Scientists at the Breault Research Organization, who have made a computer model of the stray light in the LIGO, and members of the VIRGO project, who independently reformulated the problem, concur in the methods being used.

The analytical method for calculating the effect of stray light in the LIGO has the following steps.

- Light is scattered by imperfections in the optics.
- The scattered light traverses the beam tube via a range of possible paths and receives a phase modulation as it interacts with the seismically driven baffles
- The scattered light recombines with the main beam either by scattering at a mirror or through imperfections in the photodetector.
- The scattered light is summed incoherently before recombination with the main beam.

The analytic techniques have led to a set of scaling relations and estimates for phase noise from various paths in the LIGO which depend on: the mirror scattering function, the number and placement of baffles, the diffraction by baffles, the scattering function of the tube and baffle surfaces, the motion of the tube and baffles, and the recombination mechanism. An error in the original calculations used in estimating the amplitude of the scattered radiation due to buildup in the resonant cavity was discovered recently by the VIRGO group. This has reduced the benefit that can be gained by placing a resonant cavity between the detector and the interferometer mentioned in Appendix F (Volume 1) of the Proposal. On the other hand, measurements of the tube surface roughness, baffle back scattering and detector nonuniformity indicate that the original estimates referred to in the Appendix F were too pessimistic.

The Breault Research Organization (BRO), under contract to the LIGO project, has made a numerical stray light analysis of the LIGO beam tubes and baffles using a directed Monte Carlo technique. The result of the computation are stray light brightness maps (scattered power/solid angle) at the ends of the LIGO beam tube due to light scattered from the beam tubes. The output includes the path history of each scattered ray, which is used to estimate the phase noise for that ray. The goal of baffling is to reduce the noise due to scattering to less than 1/10 the noise associated with the standard quantum limit of an interferometer with 1 ton test masses. The principal results of the study are:

- The LIGO baffling and tube optical properties can meet the requirement.
- The dominant paths for producing phase noise are due to backscatter from baffles.
- Serrating the baffle edges is effective in reducing diffraction.
- Analytic and Monte Carlo methods using the same parameters agree.

BRO was asked to iterate the stray light calculation to vary the surface roughness of the tubes, the position of the first baffle and the position of the main beam in the tube. These iterations did not reveal any major changes that could not have been anticipated by analytic reasoning. They also performed an unprejudiced Monte Carlo calculation to look for additional scattering paths in a critical region.

During the next year a decision will be made on the final baffle design. "Martin Black", a deeply anodized aluminium, has been identified as a candidate material for the baffles and other structures to control stray light in the instrumentation chambers. The factors in the decision will include the results of ongoing analytic

stray light trade off studies, vacuum compatibility measurements and cost. The baffles themselves were originally planned as sheet metal 45 degree isosceles triangles, placed into the tubes after assembly and held by friction. The baffle design has been changed to a 55 degree surface facing the nearest mirror; an attractive alternative structure consisting of a single rolled sheet is being considered.

Control of stray light in instrumentation chambers remains to be addressed. The stray light conditions in the chambers depend on the interferometer layout and on the large and small angle scattering properties of the optical components. A design to control stray light depends on the type of absorbers that may be used in the vacuum. The engineering design of the initial interferometer will include a stray light analysis.

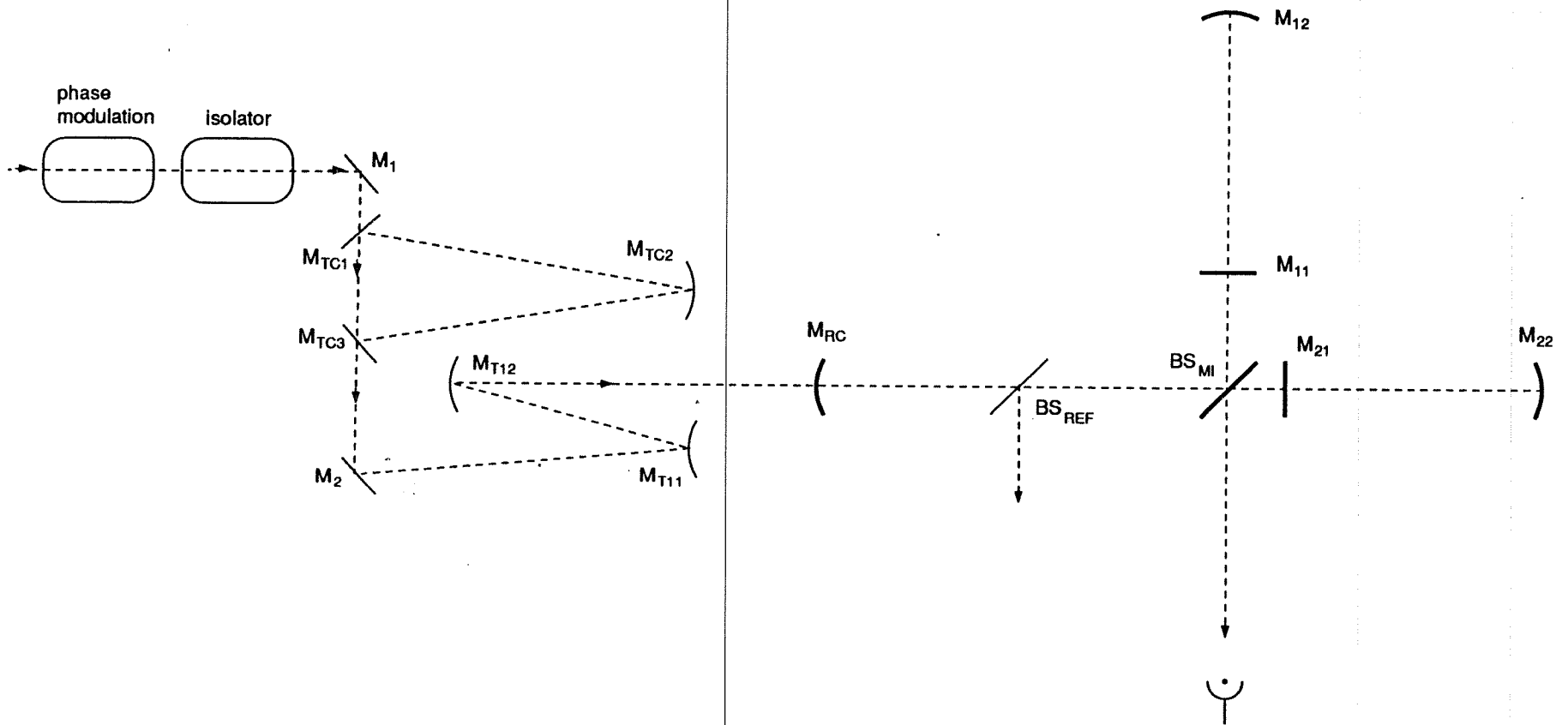


Figure C - 1: Initial interferometer optical schematic



Seismic Isolation and Suspension

Introduction

Each test mass in a LIGO gravitational-wave detector is suspended as a pendulum hanging from a platform connected to a vibration-isolation stack. The pendulum suspension allows the test mass to move freely in response to a gravitational wave; both the suspension and the vibration-isolation stack strongly attenuate seismic motion and other external vibrations. The Proposal defined target noise levels for the initial LIGO interferometers in Volume 1, Figure V-3 (p. 48). Below about 40 Hz, the sensitivity of the initial LIGO interferometers was expected to be limited by the transmission of ambient ground motion through the stack and suspension (labeled “Seismic Noise”). Between about 40 Hz and 200 Hz, random thermal motion of the suspended test masses (labeled “Suspension Thermal”), was expected to limit the sensitivity of initial interferometers. Above approximately 200 Hz, photon shot noise was expected to define the sensitivity. The transmission of seismic noise to the test masses and the thermal noise from the wings of the resonances of the test mass and the suspension are expected to play a large role in the strategy for detecting neutron star coalescences.

Seismically induced motion of test masses is equal to the ambient seismic noise multiplied by the transmission of the stacks and the wire suspensions. The vibration isolation stack consists of cascaded mass/spring stages which provide attenuation of vibrations above the resonant frequencies of the stack. Good low frequency vibration isolation favors the use of soft spring materials to obtain low resonant frequencies, subject to constraints on drift, load capacity, and vacuum compatibility. The suspension further attenuates horizontal vibrations above its pendulum-mode resonance, typically near 1 Hz. The materials for the suspension and the test mass itself are chosen to have the highest possible mechanical Q , in order to concentrate the thermal energy of each mode into its resonance peak, thus minimizing the broad band contribution of thermal noise.

These resonant mechanical filters include damping to limit the rms motion of the components. Damping of the stack resonances is provided by the use of elastomer springs and the pendulum motion of the test mass is electronically damped by an optical sensing and feedback technique.

More advanced interferometers will result from progress in lowering the seismic cutoff frequency by improvements to the stacks and suspension. More advanced stack designs may incorporate both active and passive features¹ to provide attenuation at lower frequencies. Double pendulum suspensions will provide better vibration isolation in the suspension of the test mass. Reduction of the thermal noise of the suspension and the test mass will come from understanding the losses in these structures and reducing them, both by designing structures which avoid the introduction of excess losses and by developing materials which exhibit low intrinsic losses.

Performance Targets for Vibration Isolation and Thermal Noise Suppression

The initial LIGO interferometer seismic noise target corresponds to a displacement noise of about $10^{-18} \text{ m}/\sqrt{\text{Hz}}$ at 40 Hz. The steep increase of the transmitted seismic noise below this frequency creates an effective cutoff to the interferometer sensitivity. To keep the interferometer operating in a linear, well-balanced regime, the separation between test masses should be stable to better than 10^{-13} m , and the alignment of each mass should be stable to about 10^{-7} rad . Servomechanisms are used to maintain the position and alignment requirements with occasional coarse adjustments to remove long term drifts. The noise contribution from these servos above 40 Hz must be kept below other sources of noise in the interferometers.

The initial LIGO interferometer thermal noise target corresponds to a displacement noise of about $2 \times 10^{-19} \text{ m}/\sqrt{\text{Hz}}$ at 100 Hz, with an f^{-2} dependence on frequency between 40 Hz and 200 Hz.

LIGO R&D on Seismic Noise

Characterization of Seismic Noise in the 40-meter Interferometer In a series of experiments, we have measured the transmission functions for the stacks and suspensions in the 40-meter Mark I interferometer, and have compared spectra of the ambient seismic noise with the interferometer noise. From this work we

¹ Active isolation refers to the use of servomechanisms, built into the isolation system to improve its performance.

concluded that seismic noise limited the interferometer sensitivity below about 200 Hz.

A replica of the stack used in the earlier 40-meter Mark I interferometer was analyzed by finite element modeling and shaker/accelerometer measurements. It was found that mechanical resonances in the U-shaped intermediate masses of this stack compromised vibration isolation at frequencies above about 30 Hz.

It was also found that the control block suspension system used in the 40-meter Mark I interferometer (shown in the Proposal, Volume 1, Figure III-5, p. 25) degrades the isolation relative to that of a simple pendulum, because its complex structure has too many mechanical resonances.

Reduction of Seismic Noise

Through an extensive program of finite-element modeling and performance testing, we have developed new passive stacks.² These stacks consist of four layers of masses separated by elastomer springs (Figure D-1). This prototype design for the initial LIGO interferometers will be tested as part of the initial operation of the 40-meter Mark II interferometer.

We predict the contribution of seismic noise to the 40-meter Mark II interferometer spectrum will be less than $10^{-19} m/\sqrt{Hz}$ above 150 Hz. At 100 Hz, the test mass motion is expected to be reduced by approximately two orders of magnitude compared with the Mark I interferometer. Using the ground noise expected at the LIGO sites, we estimate that this stack design, coupled with a simple pendulum suspension, should achieve a seismic cutoff frequency of about 90 Hz.

Further improvements in isolation may result from incorporating softer springs into the current stack design. We are in the process of vacuum qualifying procedures for cleaning silicone rubber springs. Measurements indicate that replacing the Viton springs with silicone rubber in the above example could further lower the seismic cutoff to very near the 40 Hz target envisioned in the proposal.

More advanced stacks will likely benefit from improvements to passive stack designs,³ evolving into designs which incorporate both active and passive isolation features.

² J. Giaime, P. Saha, D. Shoemaker, and L. Sievers, manuscript in preparation (enclosed).

³ Such as the use of suspended stages and cantilever springs, which are being developed by the VIRGO and AIGO projects.

Advanced interferometers will likely use double pendulum suspensions. Although this type of suspension is more complicated, it can have better isolation properties than a simple pendulum suspension. Once the properties of a simple pendulum suspension are well understood,⁴ we will resume our investigation of double suspension systems.

LIGO R&D on Thermal Noise

Characterization of Thermal Noise in the 40-Meter Interferometer

Thermal noise for a mechanical system can be predicted from the normal modes of the system and the damping behavior. We have studied the suspension wires in the 40-meter Mark I interferometer, using the violin modes of the wires to parametrize losses in the wires. Thermal noise was observed at the violin resonances and the damping in the wires was found to be nearly independent of frequency.⁵

Measurements of damping of internal vibrational modes of the test masses have shown anomalously high losses in the compound test masses used in the 40-meter interferometer. Since the damping mechanism is not yet clear, we cannot yet make a firm prediction of the thermal noise contributed by these modes, but this could explain some of the observed background noise in the interferometer at frequencies of several hundred hertz.

Thermal Noise Reduction

We are conducting table-top investigations to develop a phenomenological understanding of the factors which influence thermal noise in suspended test masses. An immediate goal of this research is to develop test masses and suspensions for the 40-meter Mark II interferometer with much higher mechanical Q values. We have found that a simple heuristic model gives a reasonable approximate description of the damping of the violin and pendulum modes of

⁴ Although the transfer function of a point mass on a massless string is well understood, a practical pendulum has a large number of resonant modes encompassing the many degrees of freedom of not only the mass, but the support fibers, the fiber connections, and the supporting structure. Both the spectrum of these modes and the parametrization of losses in each mode will determine the noise in the suspended test mass.

⁵ A Gillespie and F. Raab, "Thermal Noise in the Test Mass Suspensions of a Laser Interferometer Gravitational-Wave Detector Prototype," submitted to *Physics Letters A* (enclosed).

a test suspension in terms of a single, easily measurable, parameter. Using this model and the measured properties of actual suspension wires, the thermal noise contribution from the suspension wires can be obtained. We are now confident that the suspension thermal noise performance target for the initial LIGO detector can be achieved in the 40-meter interferometer. We have started investigating how the damping depends on such factors as suspension length, wire thickness, and wire tension, so that we can optimize the performance of initial and advanced detectors in LIGO.⁶ We also plan to evaluate new materials which may have improved thermal noise properties.

We have developed detailed models to predict the thermally induced motion associated with internal vibrations of the test masses once the losses in various modes are characterized, and to aid in diagnosing sources of damping. We have fabricated monolithic mirrored test masses⁷ to eliminate the mechanical joint between mirrors and test masses (which could introduce additional noise). We have begun studying how details of the suspension and control of these masses will affect their thermal noise contribution and have identified some features which can cause excess damping in the masses. Vibrational mode Q's in excess of 10^5 have been obtained, similar to results obtained with fused silica substrates by the VIRGO and Moscow groups.

Research in Collaboration with LIGO

Research at Syracuse University

The research program of Peter Saulson's group at Syracuse University is aimed at understanding the sources of thermal noise, finding the best ways to characterize the relevant parameters of test mass suspensions, and developing methods to minimize the amplitude of the thermal noise spectrum in gravitational wave interferometers.

Several investigations have been undertaken at Syracuse to elucidate the nature of thermal noise in pendulum suspensions. A direct experimental check of the fluctuation-dissipation theorem's prediction for the thermal noise power spectrum

⁶ The 40-meter Mark II vacuum system and stacks are suitable for testing suspensions and masses that are nearly identical to those intended for the initial LIGO interferometers.

⁷ Monolithic refers to the fact that the mirror surfaces are polished and coated directly onto the test mass itself.

in an oscillator dominated by internal friction⁸ is being done, using a small torsion pendulum constructed with a lossy fiber. Measurements have also been made to check whether internal friction necessarily has a strong first-order dependence on DC stress; such a dependence was suggested by some earlier ways of modeling the behavior of a pendulum, but would lead to dramatically lower Q than had been predicted. The thermal noise of a pendulum has been calculated, including both the fundamental mode and the violin modes, using the elastic equation of a thin beam under tension. An experiment to demonstrate the predicted scaling of violin mode Q with tension (here in the low tension range) has been started.

The thermal noise from the internal modes of the test mass itself has been harder to predict, because it is much more difficult to construct similar oscillators with resonance frequencies low enough to allow Q measurements in the frequency range of interest. The feasibility of measuring these losses at the relevant frequencies in actual test masses, using time domain (non-resonant) measurements of the impulse response or step response to compressional stress, is being studied.

Research at Moscow State University

V. B. Braginsky and his colleagues at Moscow State University are developing construction and measurement techniques that may help guide the design of suspensions for LIGO test masses. The focus has been to obtain the highest possible Q in suspension wires in order to minimize thermal noise.

Within the past year Braginsky's group has built and measured pendula made entirely of fused silica with Q's exceeding 1.3×10^8 (corresponding to an e-folding time for the 0.9 Hz period pendulum of 4.4×10^7 sec, or 1.4 yr). This is the result of improvements in materials processing, assembly, and surface treatment, including reduction of bulk impurities, high-temperature annealing and surface cleaning, and development of low-loss welding. Several pendula were constructed and measured, all with fiber diameter approximately 150 micrometers and pendulum mass approximately 30 gm. The measurements were made with a readout system that distinguishes between several translational and rotational oscillation modes.

Further experimental work in Braginsky's lab will include the construction of pendula with greater mass and different support fiber geometries. The measure-

⁸ The classic measurements all involved velocity damping, either from gas friction or electrical dissipation.

ments and analyses will elucidate the details of loss mechanisms (for example, determining the range of parameters for which thermoelastic damping is significant), and will provide scaling information for the design of both initial (10 kg) and advanced (100 kg) LIGO test masses.

Research at JILA, University of Colorado

P. L. Bender and his colleagues at JILA are developing a 6 axis seismic isolation system whose operating frequency band is 1 to 100 hertz. The goal is to design an isolator with a factor of 10^4 attenuation. Isolation in this frequency band is a challenging goal due to the magnitude of the seismic noise, the inability of passive systems to perform at the lower frequencies, and the low noise requirements in the hertz range.

The design consists of a 2 stage isolation system with a combination of both passive and active elements. Each stage consists of a spring-mounted platform on which sensors and actuators for motion in all six degrees of freedom are mounted. The active servo loops provide isolation below the resonant frequencies of each platform. Special sensors have been developed in-house for low noise detection of motion in the hertz range.

The first stage of the 2 stage system has been built and tested with all 6 degrees of freedom controlled. Significant attenuation was achieved in the 1 to 100 hertz band. Further experimental work will include the addition and testing of the second stage. A modeling program is also in place for doing analysis of the interaction between the two stages.

CONCEPTUAL DESIGN OF PROTOTYPE STACK

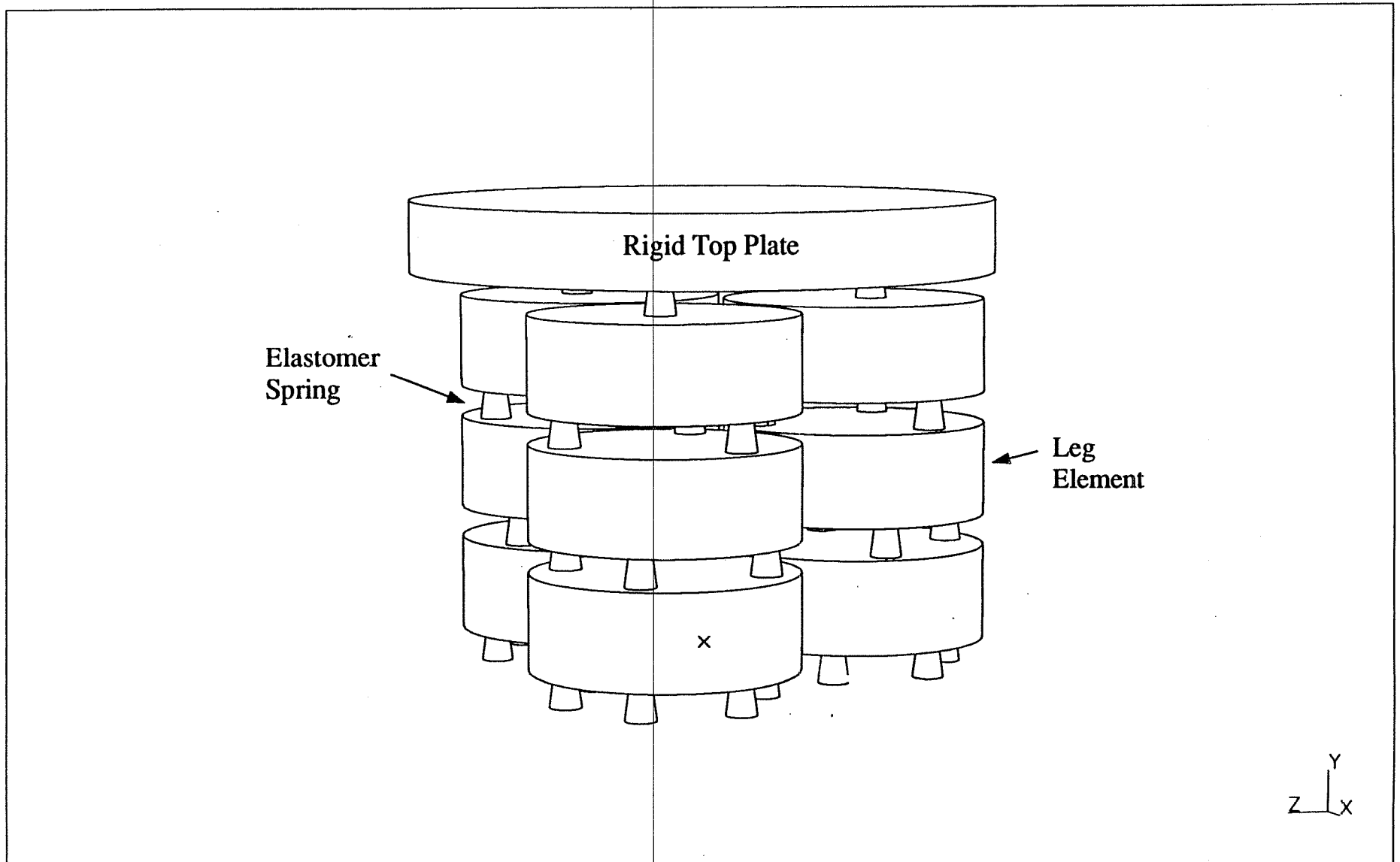


Figure D-1

LIGO Vacuum System

The LIGO vacuum system described in the Proposal, Volume 2, Sections IV-C (Mechanical Design, pp. 25) and IV-D (Vacuum Design, pp. 49), continues as the basis of our current design. In particular, the system requirements are unchanged and the degassing process has been modeled and experimentally verified. We present a listing of the principal differences between current plans and the description provided in the Proposal.

Requirements:

The LIGO design calls for reducing the gas pressure within the beam tubes and chambers to the level where interferometer noise caused by residual gas molecules is below other noise levels, such as those projected for seismic noise and shot noise in the laser beam. This requirement determines the gas pressure specifications tabulated on p. 49, Volume 2, of the Proposal.

The specifications are driven by the effect of gas molecules crossing the interferometer beams throughout the 4-km arms. Each molecule contributes to a phase shift in the beam that depends on the velocity and polarizability of the molecule. The phase noise arising from the statistical effect of many molecules crossing the beam during the measurement time has a flat spectrum over the LIGO gravitational-wave frequency band.

Molecular hydrogen is expected to be the dominant source of residual gas noise; a partial pressure of H_2 of 10^{-9} torr or lower assures that the residual gas effect is insignificant, even for the most sensitive detectors contemplated in the lifetime of the LIGO. Figure III-2, Volume 1, of the Proposal (p. 18) shows the effect of 10^{-6} torr of H_2 (equivalent to 10^{-7} torr H_2O), relative to the expected performance of initial interferometers: the gas noise is approximately an order of magnitude or more below the combined effect of thermal noise, seismic noise, and shot noise throughout the spectrum. At 10^{-9} torr H_2 , the phase noise due to the residual gas is below the optical quantum limit for 1 ton test masses (the largest masses contemplated) when the interferometers are optimized for searches for periodic signals, the most sensitive observations anticipated for LIGO.

A residual gas pressure of 10^{-6} torr of H_2 is sufficiently low to ensure that gas damping will not degrade the mechanical performance of the suspensions of the most sensitive interferometers contemplated for LIGO.

Outgassing Studies:

The strategy to obtain low residual gas levels in the LIGO vacuum systems has been to reduce material outgassing. Extensive outgassing studies have been carried out in order to achieve these reduced levels economically.

1. Hydrogen outgassing from the steel walls of the vacuum system is expected to dominate the ultimate pressure. Three years of R&D in collaboration with industry have resulted in the development of a treatment that reduces the hydrogen outgassing of 304L stainless steel. Simple and accurate methods for measuring the hydrogen outgassing of steel were also developed. The outgassing level of the steel after special annealing is about 10^{-13} torr·l·s⁻¹·cm⁻², which should allow LIGO to reach hydrogen pressures adequate for the advanced detectors, with pumping at the ends of the beam tube modules only. In a related study, we proved that the welds used in making the tubes are sufficiently impermeable to atmospheric hydrogen, and do not appear to have significantly higher outgassing than the tube wall.
2. The LIGO Project has developed and tested (on a 40 m section of 0.6 m diameter spiral weld tube) an economical method of reducing water outgassing. The method consists of wrapping the tube with inexpensive thermal insulation, then heating it for 30 days to 140 C, by passing a high current through the tube walls. This bake reduced water outgassing to $<2 \times 10^{-16}$ torr·l·s⁻¹·cm⁻², which will allow reaching water pressures adequate for the advanced LIGO detectors with pumping at the end of the beam tube modules only.
3. The presence in the vacuum system of heavy molecules, such as hydrocarbons, is of particular concern, since contamination of mirror coatings can lead to increased scattering and higher absorption. The latter can cause mirror heating when high optical power levels are present, further degrading the performance of the mirrors, and ultimately leading to irreversible damage. The LIGO Project has addressed mirror contamination along several lines:
 - Mass spectral measurements of outgassing products were used as a tool for certifying materials and components to be used with mirrors in vacuum. Calculations, as well as the analysis of past contamination events were used to define realistic certification criteria, based on outgassing measurements.
 - In conjunction with the outgassing measurements, a program is underway to expose mirrors to high intensity laser light (up to 400 kW/cm²) in the

presence of material samples for extended periods. These tests are used to qualify materials and components of interest for LIGO. On the basis of early results, we have qualified specially processed viton springs for use in seismic isolation stacks in the Mark II 40 m prototype.

- The LIGO project has defined and implemented cleaning and acceptance criteria for all parts that are intended for use in vacuum. These procedures have been used in the assembly of the Mark II vacuum system, as an intermediate step towards their use for LIGO construction.

Vacuum System Design Changes Since the Proposal:

The following material amplifies or modifies the description given in the Proposal, in sequential order. Section and page number references given below are to the Proposal, Volume 2.

Mechanical design:

1. General characteristics (Section IV-C-1, p. 25)
 - The proposed plan was to use low hydrogen stainless steel for all internal parts of the vacuum system; standard stainless steel is now being considered for non-beam tube portions of the system.
 - ~~In addition to the proposed ion pumps and liquid nitrogen pumps, provisions will be made for the future addition of getter pumps.~~
 - The proposed plan was to install ion pumps along the beam tube modules at 250 m intervals; this will now be delayed until need is determined, with ports and blanked valves installed initially. The pump ports will be 25 cm (10 in) instead of 18 in diameter.
2. Beam tube design and fabrication (Section IV-C-2-b, p. 27 ff.)
 - Negotiations are nearly complete with Chicago Bridge & Iron Technical Services Company to design and qualify the LIGO beam tubes, with fabrication and installation to follow. The beam tube specification is written as a performance specification, covering clear aperture, leakage, cleanliness, and alignment. The contractor has chosen to follow the Caltech specification for processing low hydrogen stainless steel tube material, so Caltech is responsible for the outgassing performance. The contractor is free to develop changes in the beam tube design concept detailed

in the Proposal, as long as performance requirements are met. Anticipated changes include longer tube sections and stainless steel (instead of carbon steel) stiffening rings.

3. Vacuum chambers — corner station (Section IV-C-3-a, p. 35 ff.)
 - The diagonal chamber type of design has been replaced with a unit identical to the Type 2 test mass chamber. This has several advantages: its “above beam” position of the isolation stack eliminates trenches in the floor, allows for more flexibility in isolation stack development and provides better access when servicing optical components.
 - The air suspension units supporting the support beams and isolation stacks for all chambers are not required for the initial LIGO; chamber assemblies will use removable frames in place of air suspension units to accommodate possible later installation.
 - A port has been added to the top of each HAM chamber to provide for ion pump installation, in place of installation at the former diagonal chamber position.

Vacuum design:

1. Beam tube vacuum design concept (Section IV-D-3, p.52)
 - ~~Individual tube section leak check criteria will be determined by the beam tube contractor, not necessarily at the 1/10 LIGO system specification stated in the Proposal.~~
 - The beam tube sections may be cleaned at a temporary building at the site instead of at the manufacturing plant, at the discretion of the contractor.
 - Subsequent measurements of hydrogen outgassing of the four chamber samples and other samples since the Proposal was written has revealed a marked increase in outgassing after baking of the wall material (such as a bake to remove water). Because of this, the material degassing process has been modified to improve its effectiveness. The design value for hydrogen outgassing is now 10^{-13} torr·l·s⁻¹·cm⁻².
 - LIGO specifications now prohibit the use of filler wire on vacuum welds.
 - The procedure planned for beam tube bakeout has been changed. We will vacuum bake a beam tube module as a complete unit by flowing current (2300 A) through the thermally insulated tube wall, heating the wall to 140°C by resistive heating. This will be accomplished using a

1 MW portable generator with long return cables. This technique has been demonstrated on the 40 m length of 0.6 m diameter tube at Caltech. Each bellows will be left free of insulation to equalize the elevated temperature caused by the increased resistance of the thin wall.

2. Chamber vacuum design concept (Section IV-D-4, p. 56)
 - Standard stainless steel may be used for chamber fabrication without the high temperature bake mentioned in the Proposal.

LIGO Systems and System Integration

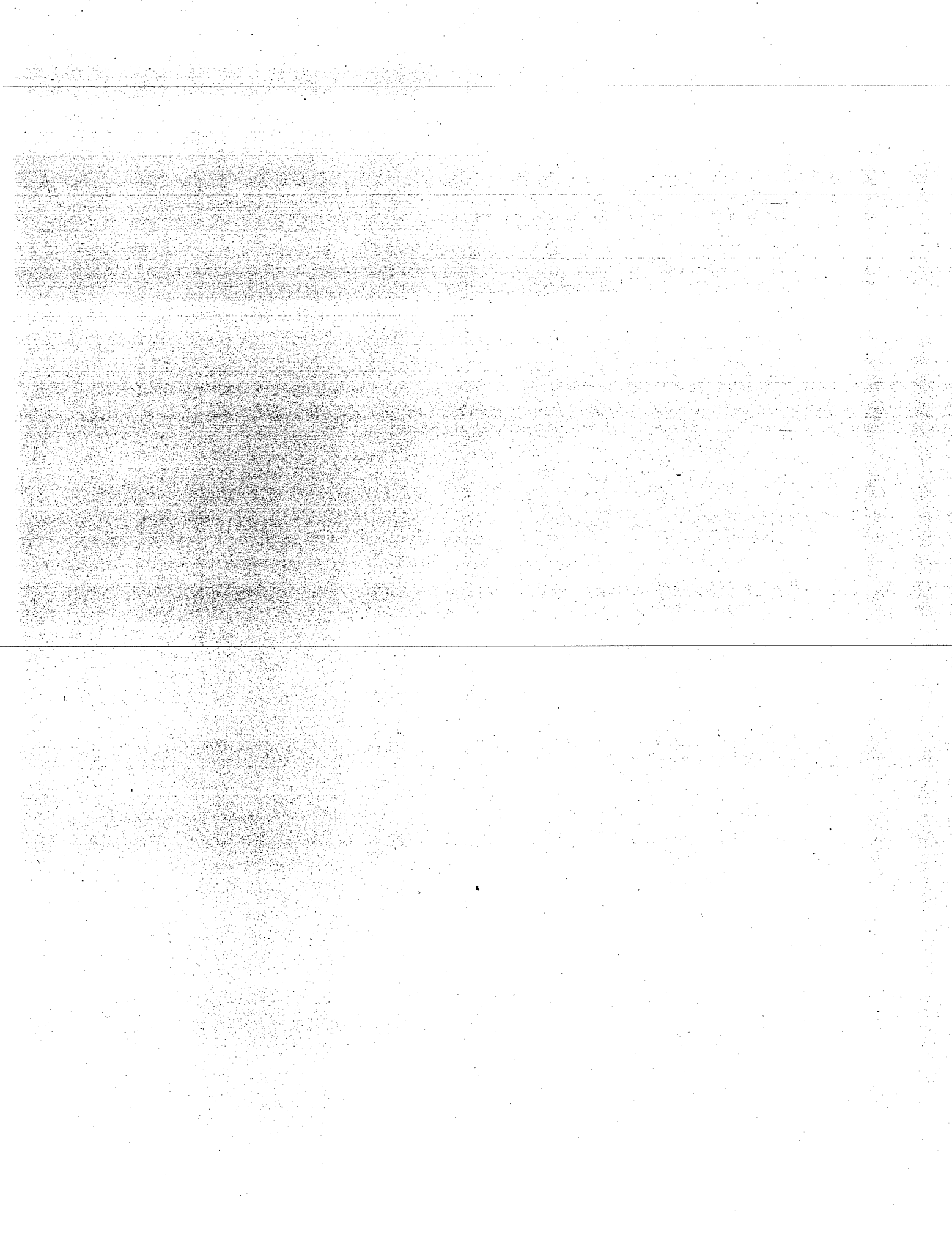
LIGO systems requirements follow from the LIGO Concept described in the Proposal, Volume 1, Section IV (pp. 31). Key requirements, specifications and goals for the LIGO facilities are summarized in the Proposal, Volume 2, Section II (pp. 2). LIGO includes a number of significant challenges in the area of system integration. Chief among these is the fact that it is the first time a sensitive interferometer will be built on such a scale, and thus there are no direct precedents which can be used. The buildings and the vacuum system need to accommodate multiple interferometers and future generations of increasingly advanced interferometers that have not yet been designed. These factors drive the LIGO design toward maintaining the greatest possible flexibility in the interfaces between the interferometers and the facilities.

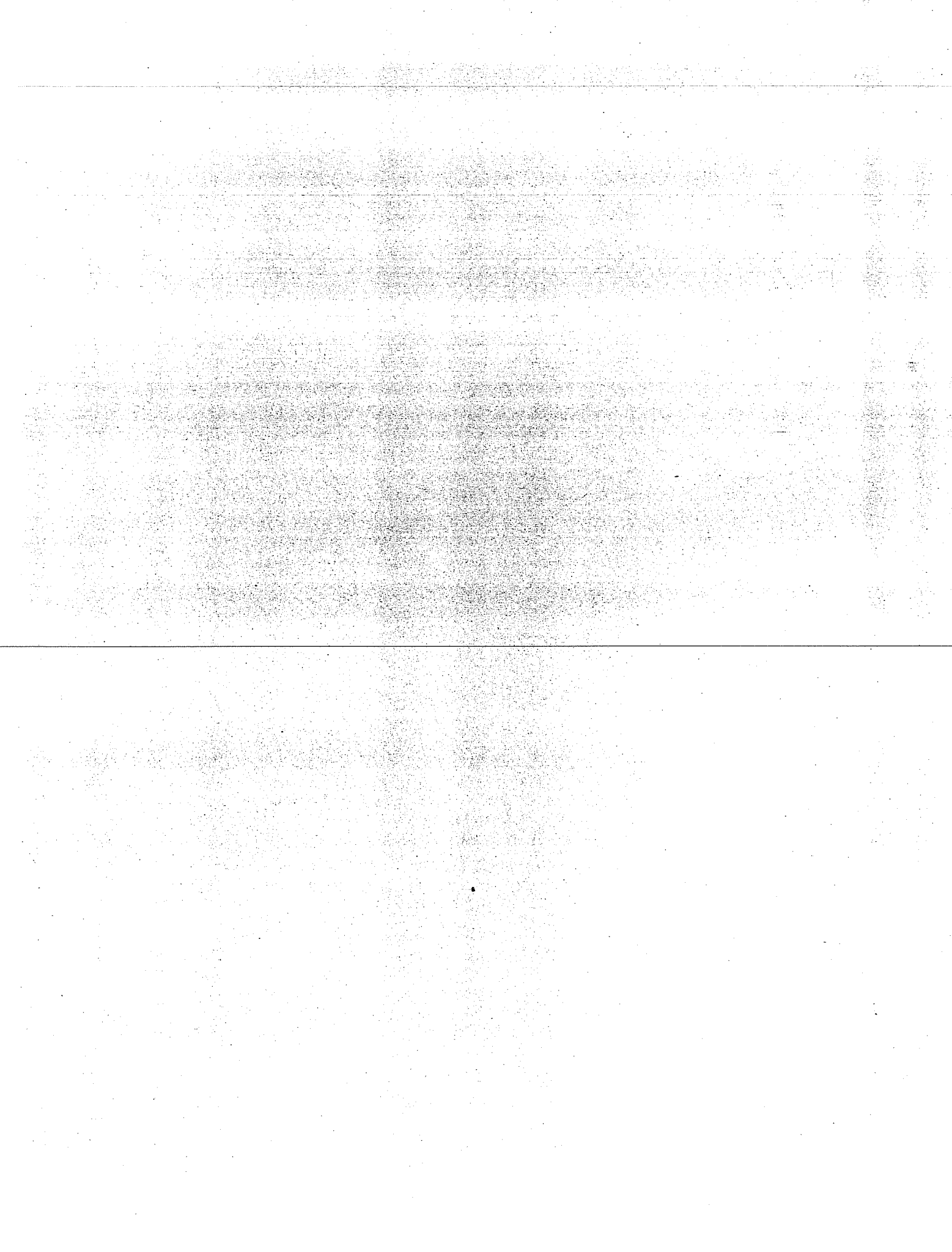
Because of the unprecedented nature of LIGO, system organization and design is necessarily a “bootstrapping” endeavor, where optimization depends on the outcome of R&D activities currently underway. Our approach is to develop the system design concurrently with the interferometer R&D program, taking full advantage of the facilities construction schedule which currently gives us four years (minimum) to fully define and implement the initial LIGO system.

During the technical review, we will discuss the current system development status of the full range of topics under consideration:

- Facilities/vacuum system modularity and expansion capability (discussed in the Proposal, Volume 2, Sections III and IV and Appendix A)
- Interferometer/vacuum system interfaces
- Interferometer subsystem organization, development and testing, and subsystem integration
- Control and Data System (discussed in the Proposal, Volume 2, Section IV–F) including observing strategies, calibration techniques and on- and off-line development and diagnostic capabilities
- Data analysis requirements, techniques and international coordination







Attachments to the Technical Supplement to the LIGO Construction Proposal (1989)

Section B:

D. Shoemaker, P. Fritschel, J. Giame, N. Christenson, and R. Weiss, "Prototype Michelson interferometer with Fabry-Perot cavities." (reprint)

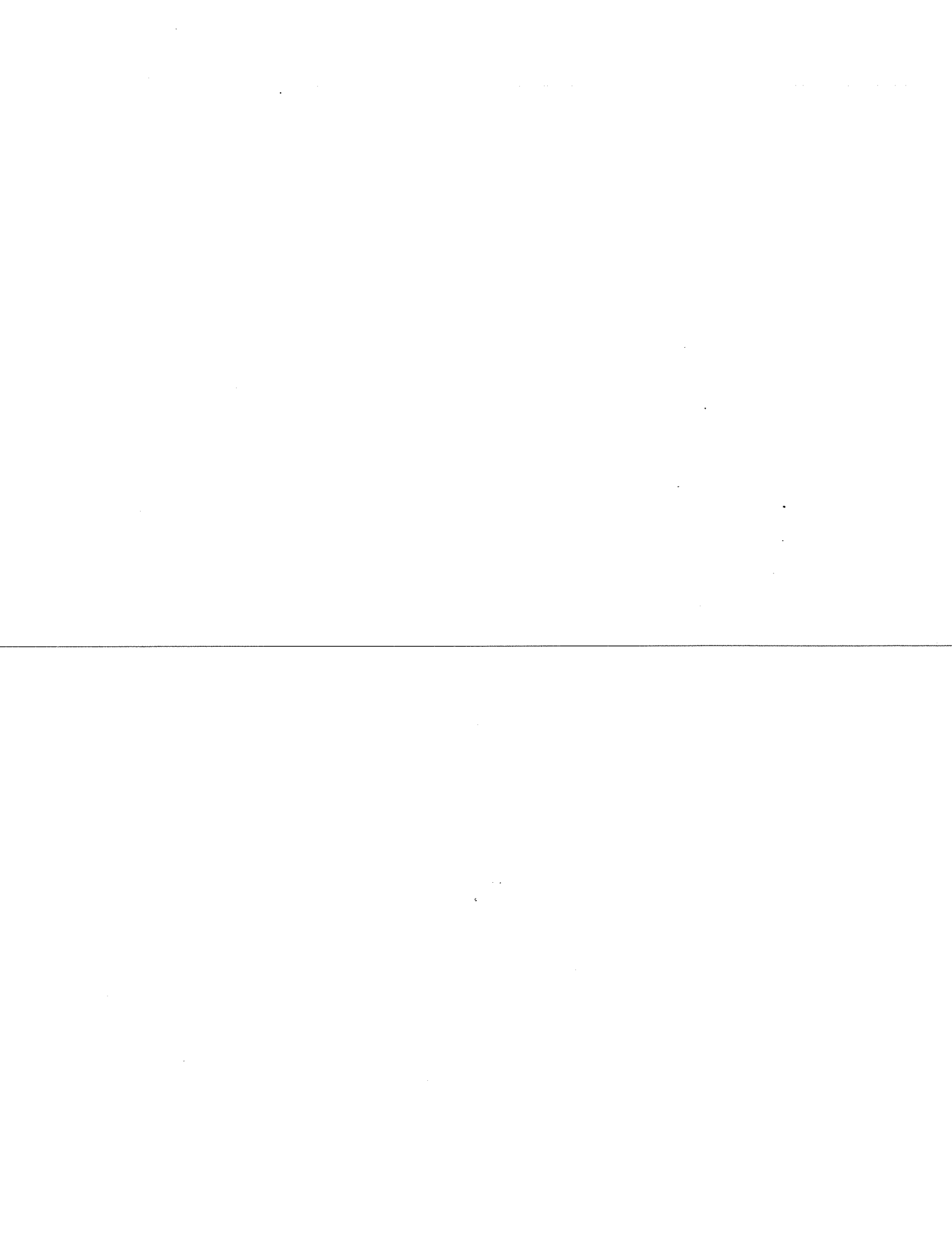
P. Fritschel, D. Shoemaker, and R. Weiss, "Demonstration of light recycling in a Michelson interferometer with Fabry-Perot cavities." (reprint)

S. Kawamura and M. Zucker, "Mirror orientation noise in a Fabry-Perot interferometer gravitational wave detector." (preprint)

Section D:

J. Giame, P. Saha, D. Shoemaker, and L. Sievers, "A passive vibration isolation stack for LIGO: design, modeling, and testing." (draft)

A. Gillespie and F. Raab, "Thermal noise in the test mass suspensions of a laser interferometer gravitational-wave detector prototype." (preprint)



Prototype Michelson interferometer with Fabry-Perot cavities

David Shoemaker, Peter Fritschel, Joseph Giaime, Nelson Christensen, and Rainer Weiss

We describe a rigid, internally modulated Michelson interferometer with Fabry-Perot cavities in the interferometer arms. The high contrast (0.986) and the small cavity losses (2.7%) permit efficient use of the light power available. The measured shot-noise-limited displacement sensitivity for 35 mW of light power is 2.5×10^{-17} m/ $\sqrt{\text{Hz}}$, in good agreement with the calculated signal-to-noise ratio. *Key words:* Interferometry, Michelson, Fabry-Perot, techniques for gravitational radiation detection.

I. Introduction

Interferometric measurements of small displacements have a number of applications, among them the detection of gravitational radiation (Refs. 1 and 2 and references therein). Techniques for increasing the sensitivity of such measurements involve increases in the effective light power through higher laser power^{3,4} or recycling,⁵ squeezing of the light field,⁶ and folding the light path in the arms of the interferometer. Two folding methods are favored: the Herriott delay line⁷ and the Fabry-Perot cavity. As part of the research and development program in support of the Caltech/MIT Laser Interferometer Gravitational Wave Observatory project,⁸ we built a small, rigid, prototype Michelson interferometer with Fabry-Perot cavities in the arms to determine realistic parameters for, and to aid in the design of, full-scale interferometers. Several free-mass prototype gravitational wave detectors have been built with Fabry-Perot cavities,^{9,10} but these do not employ optically recombined beams from the two orthogonal arms. Earlier efforts at rigid recombined-beam interferometers have not employed state-of-the-art optics¹¹ or cavity finesse similar to those to be used in the full-scale antennas¹⁰ and have not illuminated some critical points for the extrapolation to a full-scale system.

We chose to perform this research on a rigid, fixed-mass interferometer at atmospheric pressure because it allows us to concentrate our attention on the optical

configuration. The complexities associated with suspended, seismically isolated masses are avoided. One of the implications of this approach, however, is that our measurements must be made at frequencies higher than ambient acoustic and mechanical excitations. Thus the target measurement frequency for this research is 80 kHz, whereas the full-scale interferometers are sensitive in the region around 1 kHz.

In this paper we describe the optical system and its static characteristics (contrast, losses, etc.), the servo systems and synchronous modulation fringe detection, and finally the sensitivity of the complete interferometer and its limits.

II. Optics

A. Layout

The layout is shown in Fig. 1. The interferometer is constructed with commercial mirror mounts on small optical tables bolted to the circular bottom plate of a 1.5-m diam vacuum tank. This bottom plate is isolated from seismic ground motion with rubber-damped springs, giving horizontal and vertical resonances of ≈ 4 Hz. The vacuum tank is closed, but not pumped out, during the experiment. The entire tank is overpressured with filtered air. The cavity mirrors and the space between them are protected by glass tubes filled with very clean (filtered to 0.1- μm particle size with 99.99% efficiency) boiloff from liquid N₂ or with He gas. Sound absorbing material (Sonex 1) inside the tank is used to absorb acoustic noise.

Light from the laser (which is on a separate table) is coupled into a single-mode fiber, and this fiber is led into the vacuum system and is terminated in the block labeled fiber-grin; the output of this fiber-grin lens assembly is a nearly collimated beam. It is mode matched to the Fabry-Perot (FP) cavities with a single positive lens and isolated by two Faraday isolators in series. The light falls on a disk beam splitter (BS) and

The authors are with the Department of Physics and Center for Space Research, Massachusetts Institute of Technology, Cambridge, Massachusetts 02139.

Received 13 June 1990.

0003-6935/91/223133-06\$05.00/0.

© 1991 Optical Society of America.

ability to align the system; remote controls (PZT's) and misalignment information (phase front analysis) are necessary to determine the intrinsic limits.

III. Servo and Measurement Systems

Synchronous modulation-demodulation at $f_1 = 5.38$ MHz is used to detect the lengths of the two cavities (by means of the reflected light) and the Michelson fringe (by means of the light leaving the antisymmetric port). The modulation is impressed on the laser light by the Pockels cell (PCA, PCB) in each arm of the interferometer. The laser frequency is stabilized to the length of cavity A, cavity B is held on resonance by means of an actuator PZTB mounted on one of the cavity mirrors, and the Michelson is held on the dark fringe through voltages applied (in addition to the modulation) to the Pockels cells.

A. Frequency Stabilization

The laser is stabilized to cavity A using the reflection technique.¹² An error signal is derived by demodulating a fraction of the reflected light with 5.38 MHz. It is sent through a servo compensation network (CNA), which is a simple pole at 100 Hz for initial locking; for normal operation, another pole-zero pair (100 Hz and 100 kHz) is used. Finally, a Sallen-Key circuit can be added to give extra gain in the vicinity of 80 kHz (at the expense of a reduced gain around 40 kHz). The signal is amplified by a high-frequency high-voltage (± 85 V) amplifier and applied to a Pockels cell (PCFS) in the laser cavity. The unity-gain frequency is ≈ 700 kHz with a simple pole as compensation; with the normal compensation filter in place, the unity-gain frequency is ≈ 300 kHz. Long-term drifts are countered by a second loop (with compensation CNPZT) using a piezoelectric transducer actuator on the laser output coupling mirror.

B. Arm B Cavity Locking

The second arm is locked to the stabilized laser light frequency with the same reflection and demodulation technique as above. The basic servo compensation (CNB) is similar to that for cavity A, except that the pole-zero pair for the normal operating condition is at 1 Hz and 3 kHz. The actuator for the servo system is a piezoelectric transducer (PZTB) on the input coupling mirror of cavity B, which has a pronounced (24 kHz, $Q = 15$) resonance; to allow a higher unity-gain frequency in the servo loop, a passive antiresonance circuit in the compensation network (CNB) is used to cancel this resonance. The unity-gain frequency thus achieved is 4.5 kHz, which is sufficient to make the excursions from the cavity resonance acceptably small.

With the normal light intensities used for measurements, the unity signal-to-noise (shot and electronic noise limited) for the frequency detection is ≈ 0.3 Hz/ $\sqrt{\text{Hz}}$. For frequencies between 6 and 100 kHz, the gain in the servo loop is sufficient to hold the frequency noise to < 1 Hz/ $\sqrt{\text{Hz}}$; with the Sallen-Key circuit in place, the frequency noise at 80 kHz is held to the shot-noise limit of 0.3 Hz/ $\sqrt{\text{Hz}}$.

C. Michelson Locking and Detection

The Michelson path-length difference is modulated by the same Pockels cells that are used to apply the modulation to the cavities. However, the level of the modulation is significantly reduced by the optical arrangement that has light passing two times through the Pockels cells.

In the first pass through the Pockels cells, the carrier has two sidebands at $\pm f_1 = \pm 5.38$ MHz put on it. This falls on a cavity; the sidebands are largely outside the resonance curve of the FP, and thus are shifted by ≈ 0 and 2π rad after reflection. The carrier, which is held on the cavity resonance, is shifted by π rad after reflection. The reflected light now undergoes a second interaction with the modulator; new sidebands are put on the reflected carrier, which are out of phase with the sidebands that were put on in the first pass through. Thus, there is a cancellation of the modulation.

The quality of the cancellation is a function of several parameters. First, the visibility of the cavity fringes: in the current cavities, all but 2.5% of the light is reflected. The linewidth of the cavity compared to the modulation frequency is relevant; for the FP cavities and 5.38-MHz modulation, the two reflected sidebands are not at 0° and 360° but at 13° and $(360^\circ - 13^\circ)$. Finally, the distance between the modulator and the cavity input coupling mirror: the transit time causes an additional phase shift between the original and second sidebands, contributing $\approx 3^\circ$ of phase delay. A calculation shows the ratio of the signal at the modulation frequency in the double-passed configuration I^{dp} to the signal for a single pass through the modulator I^{sp} to be

$$\frac{I^{dp}(\omega_m)}{I^{sp}(\omega_m)} = J_0^2(\Gamma) \{ (1 - \sqrt{A})^2 + [\sin(2\omega_m l/c + \phi_{cav})]^2 \}^{1/2}.$$

This is derived for the case of unity contrast. Here Γ is the modulation index for a single pass through the modulator, A is the intensity reflection coefficient of the cavity on-resonance, l is the distance from the modulator to the cavity, and ϕ_{cav} is the phase shift added to the $\omega_0 \pm \omega_m$ sidebands after reflection from the cavity. In our case, the amplitude term, $(1 - \sqrt{A})^2 = (1 - 0.987)^2 = 1.7 \times 10^{-4}$, is very small, and our signal comes almost entirely from the phase shift term, $[\sin(16^\circ)]^2 = 7.6 \times 10^{-2}$. This gives a signal ratio of $I^{dp}/I^{sp} = 1/3.7$ for a typical Γ of 0.16. Our observations of this reduction compare the ω_m signal (monitored at the radio frequency output of the PDC) of the FP MI and the one-bounce MI. In the one-bounce MI the modulation is nearly doubled on the second pass, and we would predict a signal ratio, in the region where $J_1(\Gamma)$ is linear with Γ , of $I^{FPMI}/I^{MI} = 1/7.4$, which is in fair agreement with our directly observed ratio of 1/9. The result of this cancellation is that the optimum modulation depth in the recombined beam FP MI cannot be reached; note that the cavity lock (for which the signal is picked off before the second pass through the modulator) does not suffer from this cancellation.

However, sufficient signal is available to hold the Michelson to a dark fringe and to make measurements

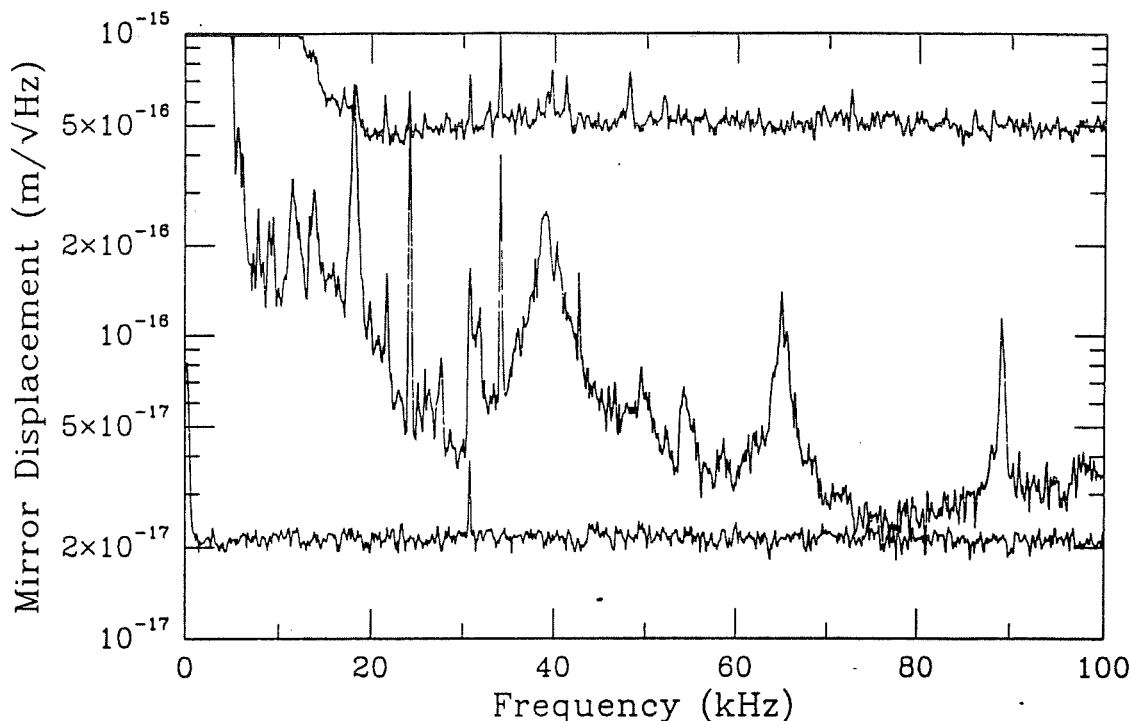


Fig. 2. Interferometer spectrum: top curve, the simple one-bounce Michelson interferometer; middle curve, the recombined-beam FP MI; bottom curve, the shot noise for the recombined-beam Fabry-Perot Michelson measurement.

of the resulting signal-to-noise ratio. The demodulated signal from the photodiode receiving light from the antisymmetric output of the interferometer is put through a compensation network CNM similar to those above, with a pole at 160 Hz for initial locking and a pole-zero pair at 1 Hz and 3 kHz for normal operation. The filtered signal is amplified with a fast high-voltage amplifier and sent to one of the Pockels cells. A unity-gain frequency of 5 kHz is attainable and sufficient. We analyzed the error signal of this loop above the unity-gain frequency to obtain the displacement noise spectrum. It is calibrated in displacement using a second piezoelectric transducer (PZTB') mounted on the B arm cavity input coupling mirror: the signal for a given applied 35-kHz signal can be seen in both the recombined-beam FP Michelson and in the simple interferometer, where the absolute magnitude can be determined either from the known sensitivity of the Pockels cell or from the calibration signal size directly compared with the Michelson output fringe amplitude.

IV. Signal Sensitivity, Noise Sources

Figure 2 shows the spectrum, expressed as equivalent mirror displacement noise of a single-cavity mirror in $m/\sqrt{\text{Hz}}$, of the interferometer. The photocurrent on the Michelson light fringe for these measurements is 8 mA (which corresponds to ≈ 35 mW of incident light power). The top flat curve is the spectrum of the demodulated signal from the Michelson antisymmetric output of the simple one-bounce Michelson with a modulation depth of $\Gamma = 0.32$; note the lack of features

at frequencies above ≈ 10 kHz. This noise level is at the shot-noise limit for the measurement. This curve assures us that the electronic systems are working correctly.

The spectrum with the two FP cavities locked is the middle, rapidly falling, curve in Fig. 2. At low frequencies (up to 30 kHz) acoustic noise is dominant. This source of noise determines the servo loop characteristics that are required, as it is against these large fluctuations that the system must be held on-resonance or on the dark fringe. In the 30–100-kHz band, a number of resonances can be seen. These are probably thermally driven resonances in the FP cavity mirror supports and are consistent with masses and resonance Q 's in the system. This noise source is the practical limit to the obtainable sensitivity with this interferometer constructed of mirrors in conventional mounts. In a full-scale interferometer, the mechanical suspension and isolation of the optical components reduces these noise sources to a level such that at astrophysically interesting frequencies (around 1 kHz) the requisite sensitivity is achieved.

In a region between 70 and 85 kHz, the spectrum closely approaches the shot noise associated with the photocurrent of the measurement. This is determined by replacing the laser light on the antisymmetric photodetector with an incandescent light source that produces the same photocurrent; this results in the noise level shown as the bottom trace in Fig. 2. This corresponds to a sensitivity of $\approx 2.5 \times 10^{-17}$ $m/\sqrt{\text{Hz}}$. We note that the increase in sensitivity obtained by adding the cavities is of the order of 25; this sensitiv-

ity is reduced from the ideal factor of $2(\text{finesse})/\pi \approx 140$ because of the reduction in modulation depth discussed above.

We have measured the sensitivity of the complete recombined-beam interferometer to frequency fluctuations of the incoming light to be 2.5×10^{-17} m/Hz. This can be interpreted as a difference in storage times of the two cavities of one part in 2000. The calculated position noise that results, given our frequency noise at 80 kHz of $0.3 \text{ Hz}/\sqrt{\text{Hz}}$, is at a level of 7.5×10^{-18} m/ $\sqrt{\text{Hz}}$. This is somewhat below the shot-noise-limited position sensitivity of the recombined-beam interferometer of 2.5×10^{-17} m/ $\sqrt{\text{Hz}}$.

A thorough calculation of the sensitivity of this instrument that properly takes into account contrast imperfections and the double passing of the modulator is quite involved. However, for small modulation, where $J_1(\Gamma)$ is linear with Γ , the double-passing is approximately equivalent to reducing the modulation depth, and we can use the simple sensitivity formula for a single-passed recombined-beam FP MI, replacing the single-pass modulation index with our reduced index. In the limit where the measurement frequency is small compared to the linewidth $c/2lF$ of the FP cavities in the arms of the interferometer, for sensitivity \bar{x} , where \bar{x} is the motion of one interferometer mirror, this gives

$$\bar{x} = \left(\frac{\lambda}{8F}\right) \left(\frac{2e}{I_{\max} + I_{\min}}\right)^{1/2} \times \left\{ \frac{[1 - CJ_0(2\Gamma_{\text{net}}) + 2I_{\text{det}}/(I_{\max} + I_{\min})]^{1/2}}{MJ_0(\Gamma_{\text{net}})J_1(\Gamma_{\text{net}})} \right\}$$

Here $\lambda = 0.514 \times 10^{-6}$ m is the wavelength of light, F is the arm cavity finesse, e is the electronic charge, and M is the fraction of the incident power that is coupled into the TEM₀₀ mode; I_{\max} is the photocurrent on the bright fringe, and I_{\min} is the photocurrent on the dark fringe without modulation, both measured at the interferometer output; I_{det} is the current that would produce a shot noise equal to the electronic noise contribution of the photodiode-amplifier combination; $J_0(\Gamma)$ and $J_1(\Gamma)$ are Bessel functions; the depth of modulation Γ_{net} is the net modulation, after cancellation. To model the interferometer contrast C , the two beams returning from the cavities are analyzed as having interfering and noninterfering components, as would be the case if wave-front distortion were the primary cause of the contrast defect. Spatial analysis of the interferometer output intensity shows that this cause is dominant. Other models for the contrast give negligibly different values for the signal-to-noise ratio.

The first factor in the sensitivity formula is the change in phase of the interferometer arm ϕ for a change in length x of the arm; for our cavities, with a finesse of $F = 220$, this has a value of 2.9×10^{-10} m/rad. The second factor is the phase uncertainty $\bar{\phi}$ caused by the shot noise of the photocurrent. For the measurement presented here, we have $I_{\max} = 8$ mA and $\bar{\phi} = 6.3 \times 10^{-9}$ rad/ $\sqrt{\text{Hz}}$. The first two factors together give the ideal shot-noise-limited unity signal-to-noise ratio,

which for the measurement presented here gives a possible sensitivity of 1.8×10^{-18} m/ $\sqrt{\text{Hz}}$. The third factor takes into account the imperfections in the optical and detection systems and has a value of 2 for a perfect system. Given the measured parameters $I_{\text{det}} = 0.016$ mA and $I_{\text{mod}} = 0.220$ mA, the electronic noise caused by the photodiode-amplifier combination is negligible. With the finite contrast ($C = 0.95$ for the measurement presented) but with optimal modulation for this contrast ($\Gamma = 0.54$), the third factor would be 2.42. However, using the largely canceled modulation ($\Gamma_{\text{net}} = 0.036$, which has been reduced by the measured factor of $I^{\text{FPMI}}/I^{\text{MI}} = 1/9$) and the measured contrast gives a factor of 12.6, and thus a predicted sensitivity of 2.3×10^{-17} m/ $\sqrt{\text{Hz}}$. This is in good agreement with the measured value.

In a separate experiment to verify the increase in sensitivity because of the FP cavities in the interferometer arms, a fixed-level 60-kHz modulation was applied to the cavity B piezoelectric transducer (PZTB). Cavity A was blocked. With cavity B alternately on-resonance and off-resonance (and thus effectively blocked), the Michelson was swept through several fringes, and the antisymmetric output was demodulated with the 60-kHz modulation frequency. The demodulated signal on-resonance was 143 times greater than with the unlocked cavity, which is in excellent agreement with the expected result. This experiment, which does not suffer the reduction in modulation depth seen with the double-passed modulation scheme, is a direct confirmation of the expected increase in sensitivity to arm length changes when a cavity is used.

V. Conclusion

We have demonstrated a MI with internal modulation and with FP cavity arms with a finesse appropriate to a full-scale interferometer. Its optical characteristics are encouraging: the relatively small losses in the arms, the symmetry between the arms, and the high contrast between the recombined beams indicate that some aspects of the mirror technology for the full-scale interferometers are close at hand. The shot-noise-limited sensitivity of the interferometer, 2.5×10^{-17} m/ $\sqrt{\text{Hz}}$, agrees well with the calculated sensitivity for the experimental parameters.

The modulation technique used here, while convenient for initial prototyping efforts, has several disadvantages, the most important being that electro-optic modulators introduce contrast defects and cannot withstand the desired power levels in recycled interferometers without introducing considerable beam distortion. In addition, cancellation of the modulation in the Michelson reduces the sensitivity and complicates the interpretation of our experimental arrangement. A longer path length between the modulator and the cavity input mirror (of the order of 14 m for our present modulation frequency $f_1 = 5.38$ MHz) would provide a solution to the cancellation of modulation sidebands, but an alternative modulation scheme such as external modulation^{13,14} is a more attractive and complete solu-

tion. However, the in-line modulation system is a convenient starting point: there is substantial convenience in the optical simplicity of the scheme and the ease of phase control with the internal Pockels cells.

D. Shoemaker thanks D. Dewey and K. Strain for helpful discussions. This study is supported by National Science Foundation grant PHY-8803557.

References

1. R. Weiss, "Electromagnetically coupled broadband gravitational antenna," MIT Res. Lab. Electron. Q. Prog. Rep. 105, 54-76 (1972).
2. B. Buckingham, ed., *Proceedings of the Fifth Marcel Grossmann Meeting on General Relativity, Perth, 1988* (World Scientific, Singapore, 1989).
3. O. Crégut, C. N. Man, D. Shoemaker, A. Brillat, A. Menhert, P. Peuser, N. P. Schmidt, P. Zeller, and K. Wallmeroth, "18 W single frequency operation of an injection-locked, cw, Nd:YAG Laser," Phys. Lett. A 140, 294-298 (1989).
4. C. Nabors, A. Farina, T. Day, S. Yang, E. Gustafson, and R. Byer, "Injection locking of a 13-W cw Nd:YAG ring laser," Opt. Lett. 14, 1189-1191 (1989).
5. R. Drever, "Interferometric Detectors for Gravitational Radiation," in *Gravitational Radiation*, N. Deruelle and T. Piran, eds. (North-Holland, Amsterdam, 1983), pp. 321-338.
6. M. Xiao, L. Wu, and H. Kimble, "Precision Measurement Beyond the shot-noise limit," Phys. Rev. Lett. 59, 278-281 (1987).
7. D. Herriott, H. Kogelnik, and R. Kompfner, "Off-axis paths in spherical mirror interferometers," Appl. Opt. 3, 523-526 (1964).
8. R. Vogt, "The LIGO project—a progress report," presented at the Twelfth International Conference on General Relativity and Gravitation, Boulder, Colo., 1989.
9. R. Spero, "Status report on the Caltech 40-meter Fabry-Perot prototype gravitational wave detector," presented at Twelfth International Conference on General Relativity and Gravitation, Boulder, Colo., 1989.
10. B. Meers, "Status report on the Glasgow 10-meter Fabry-Perot prototype gravitational wave detector," presented at Twelfth International Conference on General Relativity and Gravitation, Boulder, Colo., 1989.
11. A. Brillat, "Progress at Orsay," presented at Second European Workshop on Gravitational Wave Detection, Chantilly, France, 1986.
12. R. Drever, J. Hall, F. Kowalski, J. Hough, G. Ford, A. Munley, and H. Ward, "Laser phase and frequency stabilization using an optical resonator," Appl. Phys. 31, 97-105 (1983).
13. R. Drever, "Prospects for laser interferometer gravitational radiation detectors," presented at Tenth International Conference on General Relativity and Gravitation, Padova, Italy, 4-9 July 1983.
14. N. Man, D. Shoemaker, M. Pham Tu, and D. Dewey, "External modulation technique for sensitive interferometric detection of displacements," Phys. Lett. A 148, 8-16 (1990).

Demonstration of light recycling in a Michelson interferometer with Fabry-Perot cavities

Peter Fritschel, David Shoemaker, and Rainer Weiss

We describe the first experimental demonstration of light recycling of a Michelson interferometer with Fabry-Perot cavities in the arms of the interferometer. Light recycling is a technique for efficiently using the light in long-baseline interferometers, such as those being proposed for the detection of gravitational radiation. An increase in the interferometer circulating power by a factor of 18 is observed, which is in good agreement with the expected gain given the losses in the system. Several phenomena associated with this configuration of coupled optical cavities are discussed.

Key words: Interferometry, Michelson, Fabry-Perot, techniques for gravitational radiation detection, light recycling, coupled cavities.

I. Introduction

The development of prototype laser interferometers for the detection of gravitational radiation has led to the ability to detect differential displacements on the order of 10^{-18} m/ $\sqrt{\text{Hz}}$ (10^{-18} m of rms motion in a 1-s integration time).¹ These interferometers sense a differential phase shift of the laser light in the two arms of a Michelson interferometer through the intensity change this phase shift produces when the two beams are recombined at the beam splitter. The output signal is proportional to the optical power in the interferometer for a given phase shift. The phase shift produced by a given mirror displacement can be increased by arranging for the light to make multiple passes in each arm, using either a resonant Fabry-Perot cavity or an optical delay line. Proposed techniques for further signal increase, capitalizing either on an increase in the optical power or an increase in the phase shift, include power, detuned, resonant, and dual recycling.²⁻⁵ In each case the smallest detectable signal is limited, at best, by photon-counting statistics; without the use of squeezed states of light, we find that the equivalent phase noise caused by these quantum fluctuations (expressed as spectral density ϕ_{noise} in units of rad/Hz^{1/2} is equal to

$$\phi_{\text{noise}} = (2h\nu/\eta P)^{1/2}, \quad (1)$$

where h is Planck's constant, ν is the light frequency, η is the photodetector efficiency, and P is the bright fringe optical power. The concepts of power recycling⁶

and dual recycling⁷ have recently been demonstrated on small-scale fixed-mass interferometers with simple one-bounce mirrors in the arms. As part of the research and development program in support of the Caltech/MIT Laser Interferometer Gravitational Wave Observatory (LIGO) project,⁸ we have built a small fixed-mirror interferometer with Fabry-Perot cavities in the arms. Here we report on the first experimental demonstration of power recycling of a such a system. To illuminate any practical difficulties with such a complex, coupled-cavity system and to verify the theory of recycling, this experiment is intended as a proof of principle.

II. Simplified Theory of Power Recycling

The basic optical arrangement for power recycling is shown in Fig. 1(a). The average power at the antisymmetric output of a Michelson interferometer is equal to

$$P_{\text{anti}} = \frac{1}{2} P_0 [1 - C \cos(\bar{\Phi}_d)], \quad (2)$$

where $\bar{\Phi}_d$ is the average phase difference between the two arms and $P_0 = P_{\text{max}} + P_{\text{min}}$, where P_{max} is the output power on the bright fringe ($\bar{\Phi}_d = \pi$) and P_{min} is the output power on the dark fringe ($\bar{\Phi}_d = 0$). The contrast is $C = (P_{\text{max}} - P_{\text{min}})/(P_{\text{max}} + P_{\text{min}})$. In principle the interferometer could be operated at any point on this fringe. To achieve the best signal-to-noise ratio in a real system, however, the optimal place to operate is at $\bar{\Phi}_d = 0$, i.e., the dark fringe. The fluctuating phase difference, $\phi_d(f)$, can then be measured either by differentially phase modulating the light in the two arms and then demodulating the output signal,⁹ or by interfering the output field with a phase-modulated reference field (i.e., external modulation).^{6,10} In a well-balanced interferometer, dark fringe operation implies that nearly all the light (to the extent that power is not lost because of imperfect

The authors are with the Department of Physics and Center for Space Research, Massachusetts Institute of Technology, Cambridge, Massachusetts 02139.

Received 10 June 1991.

0003-6935/92/101412-07\$05.00/0.

© 1992 Optical Society of America.

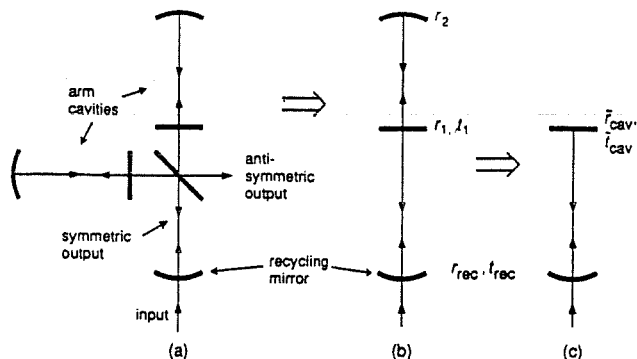


Fig. 1. (a) Optical elements of a recycled Michelson interferometer with Fabry-Perot cavities in the arms. (b) When the interferometer is operating at the dark fringe of the antisymmetric output, the two arms and beam splitter are modeled by one arm cavity, creating a three-mirror cavity. (c) The arm cavity is then modeled by a single mirror, having reflection and transmission coefficients of a Fabry-Perot cavity. The tilde denotes a complex quantity.

optics) exits through the symmetric output and travels back toward the light source. From the standpoint of the input laser beam, the interferometer looks like a mirror of reflectivity somewhat less than unity because of losses in the optics and an imperfect contrast. The power circulating in the interferometer can then be increased by making an optical cavity, with a recycling mirror at the input of the interferometer as the cavity-input mirror and with the interferometer forming the rear mirror [Fig. 1(b) and 1(c)].

For a simple two-mirror Fabry-Perot cavity on resonance, the ratio of the internal power to the input power is

$$P_{\text{int}}/P_0 = \frac{T_1}{[1 - (R_1 R_2)^2]^{1/2}} = \frac{T_1}{[1 - [(1 - A_1 - T_1)(1 - A_2)]^{1/2}]^2}, \quad (3)$$

where T_i , R_i , and A_i are the power transmission, reflection, and loss coefficients respectively of the input mirror ($i = 1$) or the rear mirror ($i = 2$). Any transmission of the rear mirror is included in the loss A_2 , so $1 - R_2 = A_2$. Applied to a recycled interferometer, T_1 is the transmission of the recycling mirror, R_2 is the reflectivity, and A_2 is the loss of the interferometer operating on the dark fringe. The ratio P_{int}/P_0 is dubbed the recycling gain, G_{rec} . For a given R_2 and input-mirror loss A_1 , the ratio P_{int}/P_0 is a maximum for

$$T_1 = (1 - A_1)[1 - R_2(1 - A_1)]. \quad (4)$$

With this simple Fabry-Perot model for recycling, we find that the maximum increase in the interferometer circulating power is then

$$G_{\text{rec}}^{\text{max}} = P_{\text{int}}^{\text{max}}/P_0 = \frac{1}{A_2 + A_1/(1 - A_1)} \approx \frac{1}{A_2 + A_1}. \quad (5)$$

The basic result is that the maximum recycling gain is equal to $1/(\text{total loss})$.

Power recycling thus gives an increase in the

output signal by a factor of G_{rec} and a corresponding reduction of the equivalent phase noise by a factor of $\sqrt{G_{\text{rec}}}$, as shown in Eq. (1). The signal, proportional to the phase difference between the arms, exits directly through the antisymmetric output; it is therefore not recycled and experiences only a single-arm storage time. The consequence is that the frequency response of the output signal to a phase difference in the arms is not affected by power recycling: the signal-to-noise ratio is increased by a factor of $\sqrt{G_{\text{rec}}}$ without changing the bandwidth of the interferometer. For a detailed discussion of the frequency response of this and other interferometer configurations, refer to Ref. 5.

Two further points are worth noting. For the case of a single mirror or delay line in each arm, the interferometer, as viewed from the symmetric side of the beam splitter, does indeed look like a simple mirror. It can be (conceptually) replaced, in the limit of perfect contrast, with a mirror of amplitude reflection coefficient $r_{\text{equiv}} = (r_{\text{arm}})^b$, where r_{arm} is the amplitude reflection coefficient of an arm mirror and b is the number of bounces in an arm. For the configuration with cavities in the arms, however, the interferometer must be replaced with a mirror that has the more complicated amplitude reflection coefficient of a Fabry-Perot cavity. The model for the recycled interferometer is now a three-mirror cavity, as shown in Fig. 1(b). This cavity leads to some interesting mode-coupling phenomena, which will be discussed in more detail in Section V.

The other point is that in the Fabry-Perot configuration, in order for the loss in the arm cavities to be small, the transmission of the cavity-input mirrors must be much greater than the mirror loss. To investigate recycling with a significant power gain, we have chosen a cavity finesse as high as possible within the limitation of keeping the cavity losses low. For the cavity loss to be not much greater than a few percent, the mirror loss of ~ 100 parts in 10^6 in this experiment requires that the input-mirror transmission be at least a few percent.

III. Description of Apparatus

We have carried out our work on a small-scale, fixed-mirror interferometer in air; this is a much simpler system than the in-vacuum, suspended-mirror design required for a gravity wave antenna, and it allows us to concentrate on the optical configuration. This configuration requires that noise measurements must be made at frequencies > 20 kHz, where ambient acoustical and mechanical excitations are much reduced, and that the servo systems must be tailored for types and levels of excitation not found in an in-vacuum, suspended design. The optical and servo system that we used is depicted in Fig. 2. The mechanical and optical construction is very similar to the apparatus described in detail in Ref. 11. A main difference from that description is that our laser light, a single frequency at 514.5 nm produced by a Spectra-Physics 2020 Ar⁺ laser, is frequency stabilized to a separate reference cavity (length 30 cm, finesse 200) rather than to one of the interferometer arm cavities.

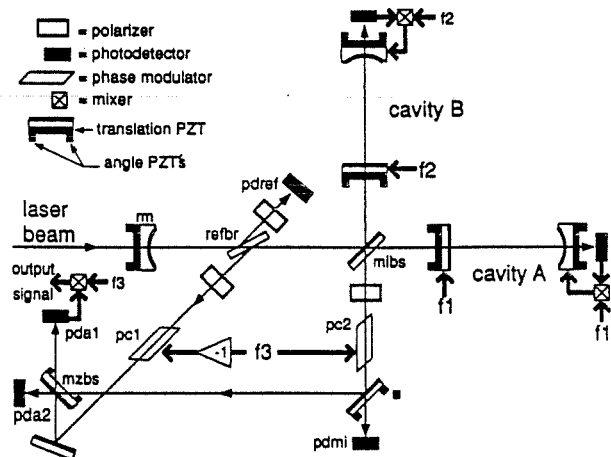


Fig. 2. Experimental arrangement.

Each interferometer mirror is mounted on a piezoelectric transducer (PZT) that allows $\sim 1 \mu\text{m}$ of translational control. In addition, each mirror is held in a mount outfitted with two PZT's, which provide ~ 3 mrad of remote alignment control in each of the two pertinent angular degrees of freedom.

Each arm cavity is 47 cm long and is constructed of a flat, 2.8% transmission input mirror and a 1-m radius of curvature, maximum reflectivity rear mirror; the finesse is thus ~ 220 and the linewidth is 1.4 MHz. These mirrors are special low-loss mirrors that are made of superpolished substrates with ion-beam sputtered dielectric coatings. The average loss per arm-cavity mirror is about 1.2×10^{-4} ; this loss leads to an on-resonance loss on reflection of $\sim 3.3\%$ for each cavity. The fraction of the input power coupled into the TEM_{00} mode of each cavity (without recycling) is $\sim M = 95\%$. To within $\pm 5\%$, we measure no difference in the matching, finesse, or losses of the two cavities. We are able to measure these properties of the individual cavities with the recycling mirror in place by merely misaligning the recycling mirror so that there is no interference in the optical path between the recycling mirror and the interferometer. The alignment of the beam to the interferometer is not significantly changed by this recycling-mirror motion. The fact that we do not have to remove the recycling mirror means that measurements of power gain and loss can all be made in a short period of time.

The cavity made up of the recycling mirror, rm; the mirror formed by the two arm-input mirrors is referred to as the recycling cavity. The recycling mirror has a 1-m radius of curvature and is placed 53 cm from the arm-input mirrors, so the TEM_{00} mode in the recycling cavity is matched, at the arm-input mirrors, to the TEM_{00} mode in the arm cavities. Ideally, the transmission of the recycling mirror should be equal to the total loss in the interferometer; the closest match available to us was an ordinary commercial laser mirror of 8.3% transmission and 0.3% estimated loss. The recycling mirror is also provided with PZT controls for one translational and two angular degrees of freedom.

Each arm cavity is held on resonance with a lock-in detection method: The length of a cavity is modulated with the input-mirror PZT at a frequency (f_m) lower than the cavity band width; the light transmitted by the cavity is detected and this signal is demodulated at f_m ; the resulting error signal is applied to the rear-mirror PZT of the cavity. Different length-modulation frequencies are used for the two cavities— $f_1 = 70$ kHz for cavity A and $f_2 = 90$ kHz for cavity B—so that the two servo systems do not couple to one another (see Section V on cavity-coupling phenomena). The Michelson antisymmetric output power is monitored with photodiode pdmi. The fringe operating point is controlled by using the PZT's to manually adjust the positions of the arm cavities with respect to the Michelson beam splitter. The setup is stable enough so that a servo control to keep the output on a dark fringe is not needed. Servo control of the recycling cavity length is also not needed, as we will explain below.

IV. Measurements

Measurements are made of the signal $\phi_d(f)$ and the noise at the antisymmetric output and of the optical power sampled at three points in the interferometer; in the recycling cavity; in the arm cavities; and at the antisymmetric output (giving a measure of the contrast).

The output signal from the interferometer is detected with the external modulation technique⁸; many of the experimental techniques in the realization of this scheme were first discussed by Schilling and Schnupp.¹² A small fraction ($\approx 2.5 \times 10^{-4}$) of the intrarecycling cavity power is reflected by a near-Brewster's-angle beam splitter, refbr, and forms the reference arm of a Mach-Zehnder interferometer. By taking the reference beam from the Michelson beam splitter symmetric output inside the recycling cavity, we can make the path lengths of the reference beam and the Michelson output beam the same. The Mach-Zehnder relative phase is $\phi^{\text{MZ}} = \phi_{\text{ref}} - \phi_{\text{MI}}$, where the phases of the reference beam (ϕ_{ref}) and the Michelson output beam (ϕ_{MI}) are defined with respect to their common phase at the Michelson beam splitter. The measurement is transferred to a high frequency, where the laser power is shot-noise limited, by modulating the phase ϕ^{MZ} at $f_3 = 5.38$ MHz in the arms of the Mach-Zehnder interferometer with Pockels cells pc1 and pc2. After the reference beam and the Michelson output beam are combined on the 50–50 Mach-Zehnder beam splitter mzbs, the photodetector pda1 output is demodulated at f_3 to retrieve the Michelson phase-difference signal.

The static Mach-Zehnder relative phase, ϕ_0^{MZ} , is controlled with a bias voltage on the Pockels cells so that the Michelson signal at 70 (or 90) kHz, as indicated by the demodulated output of pda1, is a maximum. The Michelson signal detected by the Mach-Zehnder interferometer is proportional to $\sin(\phi_0^{\text{MZ}})$, so when the system has maximum sensitivity to the Michelson phase difference ($\phi_0^{\text{MZ}} = \pi/2$), this sensitivity depends on the Mach-Zehnder relative phase only in second order. The combination of

this insensitivity and the mechanical stability of the system means that accurate measurements of the signal can be made without servo controlling ϕ^{MZ} .

When the contrast is less than one, we find that a signal with first-order sensitivity to ϕ^{MZ} does remain, but this signal is smaller than the Michelson signal by a factor of $\sim [2/(1 - C_{00})]^{1/2}$, where C_{00} is the Michelson contrast for the TEM_{00} component of the antisymmetric output beam. Inspection of the spatial intensity pattern at the antisymmetric port of the interferometer shows that the majority of the contrast defect in our system is caused by wave-front distortion: The light at the dark fringe is dominated by modes of higher order than the TEM_{00} mode. Thus the measured contrast $C < C_{00}$ can be used to obtain an upper limit for this factor; this inequality gives $[2/(1 - C_{00})]^{1/2} \geq 80$.

The system is brought into angular alignment and resonance in steps. First, with the recycling mirror misaligned, we align the two arm cavities for maximum coupling to the TEM_{00} modes. Then, with the arm cavities locked on resonance, we adjust the Michelson phase to the dark fringe and give the arm mirrors further small alignments to achieve the minimum dark fringe. We then bring the recycling mirror into rough alignment (the arm cavities do not remain resonant for this step). With an arbitrary initial length of the recycling cavity, we adjust the two arm-cavity lengths for resonance and hold them there with the servos. The recycling-cavity length is then adjusted for resonance in the recycling cavity, and each mirror is aligned for maximum power in the system. Because of the phase shift on reflection from an arm cavity (π rad on resonance, ≈ 0 rad off resonance), the recycling-cavity resonance length depends on the length of the arm cavities.

Measurements of the recycling-power gain were made for three configurations of the Michelson interferometer: a simple Michelson using only the input mirrors of the arm cavities (the light paths to the rear mirrors are blocked); the Michelson with the two Fabry-Perot cavities in the arms; and the asymmetric Michelson, with a Fabry-Perot cavity in one arm and a simple mirror (the second arm-cavity input mirror) in the other. Photodiode *pdref* monitors the signal reflected from *refbr* and gives a measure of the input power when the recycling mirror is misaligned and a measure of the power gain when the system is recycled. The polarizer between the reference splitter *refbr* and the photodiode *pdref* ensures that only light in the (horizontal) polarization of the input beam is detected; the polarizers on the other side of the reference splitter and at the antisymmetric output serve the same purpose.

In the simple Michelson case, we observe the maximum power gain to be $G_{rec} = 19.5$. To compare this gain with the expected value, we make an accounting of the measured and estimated loss as shown in Table I.

The estimated losses are based on experience with other optics that have the same kind of dielectric

Table I. Losses for the Recycled Simple Michelson Interferometer

Loss Element	Loss per Pass (%) ^a	Round-Trip Loss (%)
Cavity input mirror: Transmission	2.8 (m)	2.8
Cavity input mirror: Reflection from antireflection-coated surface	0.2 (m)	0.4
Beam splitter: 50-50 surface	0.3 (e)	0.6
Beam splitter: antireflection-coated surface	0.15 (e)	(1/2) × 0.3
Reference beam splitter	2 × 0.015 (m)	0.06
Recycling mirror	0.3 (e)	0.3
Contrast defect	0.02 (m)	0.02
Total round-trip loss		4.33

^am, Measured; e, estimated.

coating. The factor of 1/2 for the round-trip loss of the beam splitter antireflection-coated surface accounts for the fact that this loss occurs only in one arm; the factor of 2 in the loss per pass of the reference beam splitter accounts for the two surfaces of the splitter. The contrast defect refers to the average fractional power coming out the antisymmetric port of the Michelson beam splitter. Using the values of $T_1 = 8.3\%$, $A_1 = 0.3\%$, and $A_2 = 4.03\%$ in Eq. 3 gives us an expected power gain of 20.6. The measured factor of 19.5 is the ratio of the recycling-cavity internal power to the total input power. If we correct for the fraction of the input power that is in the TEM_{00} mode of the cavity, $M = 0.95$, we find that the measured increase in the TEM_{00} mode is $G_{rec}^{TEM_{00}} = 19.5/0.95 = 20.5$; the agreement between the expected and measured values is quite good.

For the configuration with Fabry-Perot cavities in the arms of the Michelson interferometer, we find the maximum observed gain to be $G_{rec}^{TEM_{00}} = 18.0$, which is corrected for the recycling-cavity TEM_{00} mode-matching of $M = 0.95$. $G_{rec}^{TEM_{00}}$ is the ratio of the recycling-cavity internal power to the input power; the power in the arm cavities, as measured by the cavity transmissions, also increases by this factor (to within $\pm 5\%$). In this case we show the loss accounting in Table II.

The effect of the slightly differing loss in the two cavities has been approximated by using the average cavity loss for the round-trip loss from the cavities. The expected value of the recycling gain, with $T_1 = 8.3\%$, $A_1 = 0.3\%$, and $A_2 = 4.6\%$ in Eq. 3, is $G_{rec}^{predicted} = 18.9$. With these losses the recycling gain for the optimal recycling mirror, $T_1 \approx A_1 + A_2 = 4.9\%$, would be 20.4; the penalty for using a recycling mirror with a transmission somewhat higher than optimum is not high.

In each configuration, we measure the 70- (or 90-) kHz signal (ϕ_d) with the Mach-Zehnder interferometer. The increase in the signal with recycling is found to be equal, within $\pm 5\%$, to the increase in the recycling-cavity internal power, verifying that the signal does increase with the circulating power. The absolute signal size, given the applied mirror motion,

Table II. Losses for the Recycled Fabry-Perot Arm Michelson Interferometer

Loss Element	Loss per Pass (%) ^a	Round-Trip Loss (%)
Cavity A reflection	3.1 (m)	1/2(3.1 + 3.4)
Cavity B reflection	3.4 (m)	
Cavity A and B input mirrors: reflection from antireflection-coated surface	0.2 (m)	0.4
Beam splitter, mibs: 50-50 surface	0.3 (e)	0.6
Beam splitter, mibs: antireflection-coated surface	0.15 (e)	1/2 × 0.3
Beam splitter, refbr	(2) × 0.025 (m)	0.1
Recycling mirror	0.3 (e)	0.3
Contrast defect	0.1 (m)	0.1
Total round-trip loss		4.9

^am = measured; e, estimated.

the intensities in the Mach-Zehnder interferometer, and the Mach-Zehnder modulation depth, is compared with the level predicted by the theory of Ref. 6. In each case the measured signal is found to be less than the predicted level by a factor of ~1.2. This is a reasonable agreement, considering the ~10% uncertainties in the above parameters. The signal is also found to increase proportionally with $J_1(m)$ up to the maximum modulation index we can achieve, which is $m = 0.83$ (the maximum of J_1 occurs for $m = 1.82$). The sensitivity to the Mach-Zehnder phase, ϕ^{MZ} , is measured to be 200-1000 times less than the sensitivity to the Michelson phase, which is consistent with the lower limit calculated above.

The output noise is also examined with the Mach-Zehnder interferometer by measuring the power spectrum of the output of photodetector pd1. For the recycled Fabry-Perot Michelson interferometer, we find that the output noise is much larger than the contribution caused by the shot noise and that it is limited by various unidentified mechanical resonances. In addition, relatively large low-frequency signals saturate the photodetector for Mach-Zehnder modulation depths in excess of $\sim m = 0.025$. It is clear that a fixed-mass, in-air system is not suitable for detailed noise studies.

The results of the asymmetric Michelson interferometer, consisting of a Fabry-Perot in one arm and a simple mirror (the cavity-input mirror) in the other, address the question of how the interferometer contrast changes with recycling. In the nonrecycled asymmetric configuration, the contrast is poor for the following reason. Light in the cavity arm that does not couple into the cavity does not experience the additional cavity π -rad phase shift, but in the simple-mirror arm all the light experiences the same phase shift at the mirror. Therefore, at the antisymmetric output, the higher-order modes from the two arms constructively interfere at a Michelson path-length difference from which the TEM₀₀ modes destructively interfere. The contrast we measure in the nonrecy-

clad case is $C = 0.77$, which corresponds to ~10% of the light contained in higher-order modes. The recycling cavity rejects these higher-order modes to some degree when this system is recycled. The contrast becomes $C = 0.98$. If this contrast defect is still caused by higher-order modes, this implies that the mode matching of the recycling-cavity light into the arm cavities is $M = 0.99$.

The contrast also improves for the symmetric arm configurations when the system is recycled. For a contrast near unity, we find that the fractional power lost at the antisymmetric output is $A_C \approx (1 - C)/2$. The measured loss in our system for the various configurations is as follows. Simple MI (Michelson): $A_C = 5.6 \times 10^{-4}$; recycled simple MI: $A_C = 1.5 \times 10^{-4}$; FPMI (Michelson with cavities in the arms): $A_C = 1.7 \times 10^{-3}$; recycled FPMI: $A_C = 3.4 \times 10^{-4}$. The figures refer to the minimum power detected with *pdmi*. In the FPMI configurations, large residual low-frequency signals ($f \sim 100$ Hz) make the average power (averaged over ~0.1 s) on *pdmi* ~3-4 times the minimum. It is the average power loss that appears in the loss accounting in Tables I and II as the contrast defect. The fractional power lost through the antisymmetric output decreases by a factor of 4-5 when the system is recycled for both the simple MI and the FPMI. We are still investigating the mechanism to explain this phenomenon.

V. Cavity Coupling

As was mentioned in Section II, the recycled Fabry-Perot arm interferometer can be modeled by a three-mirror cavity, as shown in Fig. 1(b). It is convenient to view this as a two-mirror cavity, formed by replacing the middle and rear mirrors (i.e., the arm cavity) with a mirror that has the amplitude reflection and transmission coefficients of a Fabry-Perot cavity, $(\tilde{r}, \tilde{t})_{\text{cav}}$ [Fig. 1(c); the tilde denotes a complex quantity]:

$$\tilde{r}_{\text{cav}}(\theta) = \frac{r_1 - r_2(r_1^2 + t_1^2)\exp i\theta}{1 - r_1 r_2 \exp i\theta}, \quad \tilde{t}_{\text{cav}}(\theta) = \frac{t_1 t_2 \exp i\theta/2}{1 - r_1 r_2 \exp i\theta}, \quad (6)$$

where r_i (t_i) is the amplitude reflection (transmission) coefficient of the input mirror ($i = 1$) or the rear mirror ($i = 2$), and the independent parameter $\theta = 2\omega l/c$ is a dimensionless expression for the optical frequency deviation from the cavity resonance. In this expression, ω is the optical frequency in radians per second, l is the cavity length, and c is the speed of light. An imperfect contrast can be accounted for by multiplying \tilde{r}_{cav} by a factor of < 1 . The three-mirror cavity then consists of an input (recycling) mirror characterized by r_{rec} and t_{rec} , and a rear mirror characterized by \tilde{r}_{cav} and \tilde{t}_{cav} . In general the resonance properties of such a cavity are quite complex, with the mode losses depending on the field distribution between the two cavities; see Ref. 13 for a discussion. For example, the ratio of the field inside the recycling cavity to the input field is

$$E_{\text{rec}}/E_0 = \frac{t_{\text{rec}}(1 - r_1 r_2 \exp i\theta)}{1 - r_1 r_2 \exp i\theta + r_{\text{rec}}(r_1 - r_2(r_1^2 + t_1^2)\exp i\theta)\exp i\theta}, \quad (7)$$

where $\theta_c = 2\omega l_{\text{cav}}/c$ and $\theta_r = 2\omega l_{\text{rec}}/c$. The double resonance condition of recycling corresponds to $\theta_c = 2n\pi$ and $\theta_r = 2m\pi$.

The linewidth of the combined cavity, $\Delta\nu_{\text{rec}}$, is defined as the full width at half maximum of the recycling-cavity internal power curve as a function of the optical frequency. The pole frequency of a cavity, the point where the magnitude of the frequency response is down by 3 dB and the phase is at -45 deg, occurs at half the cavity linewidth. When the loss is dominated by the arm cavity and the optimum recycling mirror has been chosen ($T_1 = \text{loss}$), some manipulation of Eq. (7) gives

$$\Delta\nu_{\text{rec}} \approx \Delta\nu_{\text{cav}}(1 - R_{\text{cav}})/2 = \Delta\nu_{\text{cav}}/2G_{\text{rec}}, \quad (8)$$

where $\Delta\nu_{\text{cav}}$ is the linewidth (full width, half maximum) of the isolated arm cavity and $R_{\text{cav}} = |\bar{r}_{\text{cav}}(0)|^2$ is the power reflection coefficient of the arm cavity on resonance. This is a much narrower linewidth than that of an arm cavity. For our system, a numerical solution of Eq. (7) gives the combined linewidth as $\Delta\nu_{\text{rec}} \approx 50$ kHz, compared with the individual arm-cavity linewidth of $\Delta\nu_{\text{cav}} \approx 1.4$ MHz. The 70- and 90-kHz modulation frequencies of the arm-cavity lengths are much lower than the 700-kHz pole frequency of an isolated arm cavity, so when the system is not recycled the 70- and 90-kHz sidebands have nearly zero phase shift with respect to the carrier. With recycling the pole frequency of the system becomes ~ 25 kHz. The 70- and 90-kHz sidebands thus acquire an additional phase shift of about 70 deg because of the coupled-cavity response. The consequence is that the servos require a compensating shift in the phase of each lock-in local oscillator.

The addition of the recycling mirror also couples the two arm cavities to one another. For example, fluctuations in the length of cavity A produce fluctuations in the amplitude and phase of the field reflected from cavity A. Because of the recycling mirror, these fluctuations appear in the input field to cavity B, and thus also in the reflected and transmitted fields of cavity B. Our cavity-length modulation servos work by holding to zero the signal at f_m transmitted by each cavity. If the cavities were modulated at the same frequency and one of the cavities, e.g., A, were slightly off resonance, some of the signal at f_m transmitted through cavity B would be caused by the field reflected from cavity A. The cavity B servo would misinterpret this signal and cavity B would not necessarily be held to a local maximum of the internal power. We thus have to modulate the two arm cavities at different frequencies so that length changes of cavity A will not be interpreted by the cavity B servo as length changes of cavity B. Note that laser amplitude noise can corrupt the servos in the same way, but the amplitude noise of the laser at 70 and 90 kHz is not large enough to be a problem.

The action of the arm servos revealed a further coupling between the recycling-cavity length and the arm-cavity lengths. Consider the case of the three-mirror cavity, Fig. 1(b), initially at the double reso-

nance condition, $\theta_c = 2n\pi$ and $\theta_r = 2m\pi$. This is the point at which the power coupled into the arm cavity, and thus the power transmitted through the system, is a (global) maximum. If the recycling cavity is not resonant, so that $\theta_r = 2m\pi + \Delta\theta_r$, the power transmitted through the system is maximized for $\theta_c \neq 2n\pi$, though at a lower level than the double resonance condition, the explanation is as follows:

With respect to the input field E_0 , the field transmitted through the coupled cavities is

$$E_T/E_0 = \frac{t_{\text{rec}}t_1t_2 \exp i(\theta_r + \theta_c)/2}{1 + r_{\text{rec}}r_1 \exp i\theta_r - r_1r_2 \exp i\theta_c - r_{\text{rec}}r_2(r_1^2 + t_1^2)\exp i(\theta_r + \theta_c)} \quad (9)$$

The magnitude of the transmitted field is a maximum for an arm-cavity length of

$$\theta_c = \tan^{-1} \left\{ \frac{-r_{\text{rec}}t_1^2 \sin \theta_r}{r_1[1 + r_{\text{rec}}^2(r_1^2 + t_1^2)] + r_{\text{rec}}(2r_1^2 + t_1^2)\cos \theta_r} \right\}. \quad (10)$$

If $\theta_r = 2m\pi$ or $r_{\text{rec}} = 0$, this shows that the transmitted power is a maximum at $\theta_c = 2n\pi$, as it must be. In general, however, the maximum occurs for $\theta_c \neq 2n\pi$. A numerical examination of Eq. (10), using the values of r_1 and t_1 for our system, shows that when r_{rec} is not near zero and $\Delta\theta_r \ll 1$, the maximum transmission occurs at a θ_c for which the phase on reflection from the arm cavity (in addition to the on-resonance phase shift of π rad) is very nearly $-\Delta\theta_r$.

That is, if the arm servo is holding the arm cavity to a maximum in transmitted power, then the round-trip phase in the recycling cavity (propagation phase plus arm-cavity reflection phase) is essentially restored to $2m\pi$. The resulting decrease in the power in the arm cavity is determined by the isolated arm-cavity linewidth rather than by the much narrower $\Delta\nu_{\text{rec}}$, because the recycling cavity remains resonant. For our system, with a constant arm-cavity length of $\theta_c = 2n\pi$, the half-power points of the transmitted light, Eq. (9), occur at a deviation from the resonant recycling-cavity length ($\theta_r = 2m\pi$) of $\Delta\theta_r = \pm 0.048$ rad. With the arm cavity under servo control, so that the arm-cavity length is given by Eq. (10), the half-power points of the transmitted light occur for $\Delta\theta_r = \pm 1.75$ rad. The combination of this compensation of recycling-cavity length fluctuations by the arm-cavity servo and the mechanical stability of the system means that accurate measurements (to within $\pm 1\%$) of the signal and power levels at the double resonance condition can be made without actively stabilizing the recycling-cavity length.

VI. Scaling the Optical Configuration

As a technique for increasing the position sensitivity of an interferometer in the practically accessible gravity wave band ($100 \text{ Hz} \leq f \leq 10 \text{ kHz}$), power recycling only makes sense on a large-scale (several kilometer arm lengths) interferometer. The reasoning is as follows. To optimize the position sensitivity, we should

store the light in each arm for a time that is comparable with half the period of the lowest frequency gravity wave, f_0 , the interferometer is designed to detect. For prototype-scale interferometers (arm lengths tens of meters or less), this requirement leads to a large number ($\geq 10^4$) of equivalent bounces in the arms. For a Fabry-Perot interferometer of length l , an input-mirror intensity transmission T_1 , and a total mirror loss A , this requirement translates into choosing the cavity-energy storage time, $\tau_{st} \approx 2l/c(T_1 + A)$, to be $\tau_{st} = 1/4\pi f_0 \approx 1$ ms. This time can be achieved by making the arm input-mirror transmission very low, but then, given the loss in current state-of-the-art mirrors (10–100 parts in 10^6), a majority of the light would be lost (absorbed or scattered) in the arms. In this case power recycling cannot give a significant increase in power. In a full-scale interferometer (arm lengths of a few kilometers), however, the equivalent number of bounces required is much less (~ 100), and the fractional power lost in the arms is a few percent or less. In this case, a power gain of ~ 30 is realistic. For fixed-mirror losses, the power lost in a cavity is inversely proportional to the input-mirror transmission, so the recycling gain is an optimally designed interferometer scales with the arm length, L_{arm} . Thus the increase in position sensitivity that is possible with power recycling scales as $(L_{arm})^{1/2}$.

The servo and signal detection schemes used here are convenient for this type of prototype experiment. Other techniques, such as using rf phase modulation to obtain the cavity-error signals, are possible and might be more appropriate for a full-scale interferometer.

Some comments about the losses in a large system can be made. The cavity finesse in this experiment is appropriate to a full-scale interferometer, but the coating technology has improved and (small) mirrors with a loss up to 10 times less than those used in this experiment are now available. Significant further reductions in the loss could be made by using a Michelson beam splitter and a recycling mirror made with low-loss coatings, and by using V coatings for all antireflection surfaces. The small contrast defect is not a significant loss in this experiment, but the beam is small ($\omega_0 \approx 0.3$ mm) compared with a full-scale system ($\omega_0 \approx 3$ cm). Because the phase-front distortions caused by the optical elements will be different on these two scales, we can make no conclusions about the contrast in a large system. Nonetheless, if the contrast is not less than $C \approx 0.99$, a power gain of at least 30 should be possible.

The vastly different recycling and arm-cavity lengths in a full-scale system produce a mode structure much different from this prototype, but this structure does not present any fundamental problems. For an arm length of 4 km and a recycling gain of ~ 30 , the combined cavity linewidth of such a system is $\Delta\nu_{rec} \sim 5$ Hz; see approximation (8). This linewidth will serve to filter the laser frequency and amplitude fluctuations in the gravity wave band.

VII. Conclusions

We have demonstrated the power recycling of a Michelson interferometer with Fabry-Perot cavity arms and an external modulation scheme for extracting the Michelson signal. The measured increase in power and in signal sensitivity for this system is a factor of 18, which agrees well with the expected gain given the known losses in the system.

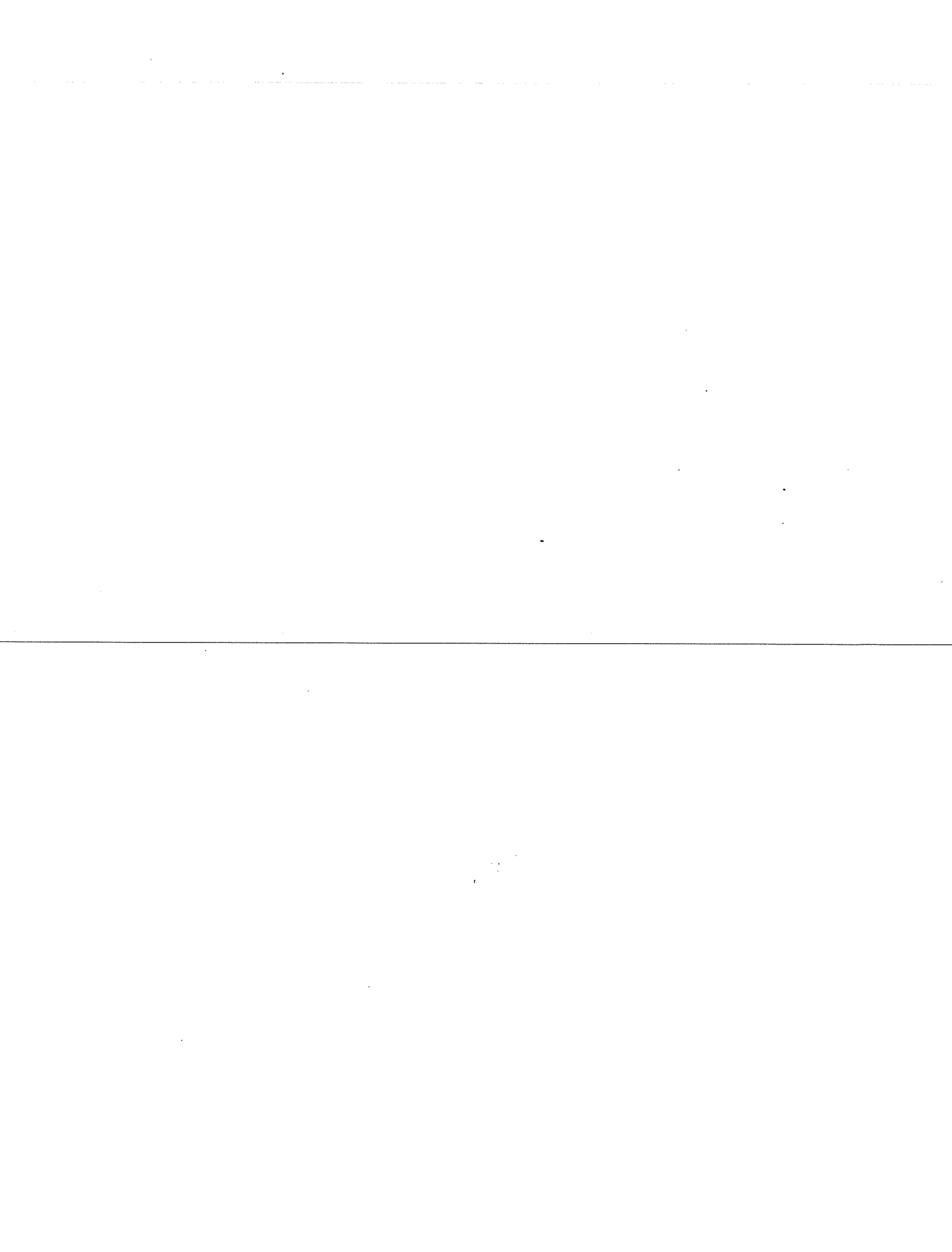
We have also investigated some of the complexities of the resonance properties of a recycled Fabry-Perot arm Michelson interferometer. This investigation provide useful information in the designing of the modulation and servo systems of a full-scale interferometer.

This work is supported by National Science Foundation grant PHY-8803557.

We thank the entire LIGO team at Caltech and MIT for its support and collaboration.

References and Notes

1. D. Shoemaker, R. Schilling, L. Schnupp, W. Winkler, K. Maischberger, and A. Rüdiger, "Noise behavior of the Garching 30-meter prototype gravitational-wave detector," *Phys. Rev. D* **38**, 423–432 (1988).
2. R. Drever, "Interferometric detectors for gravitational radiation," in *Gravitational Radiation, Les Houches 1982*, N. Deruelle and T. Piran, eds. (North-Holland, Amsterdam, 1983), pp. 321–338.
3. J. Y. Vinet, B. Meers, C. N. Man, and A. Brillet, "Optimization of long-baseline optical interferometers for gravitational-wave detection," *Phys. Rev. D* **38**, 433–447 (1988).
4. B. J. Meers, "Recycling in laser-interferometric gravitational-wave detectors," *Phys. Rev. D* **38**, 2317–2326 (1988).
5. B. J. Meers, "The frequency response of interferometric gravitational wave detectors," *Phys. Lett. A* **142**, 465–470 (1989).
6. C. N. Man, D. Shoemaker, M. Pham Tu and D. Dewey, "External modulation technique for sensitive interferometric detection of displacements," *Phys. Lett. A* **148**, 8–16 (1990).
7. K. A. Strain and B. J. Meers, "Experimental demonstration of dual recycling for interferometric gravitational-wave detectors," *Phys. Rev. Lett.* **66**, 1391–1394 (1991).
8. R. Vogt, "The U.S. LIGO project," presented at the Sixth Marcel Grossman Meeting on General Relativity, Kyoto, Japan, 23 June 1991.
9. R. Weiss, "Electromagnetically coupled broadband gravitational antenna," *Mass. Inst. Technol. Res. Lab. Electron. Q. Rep.* **105**, 54–76 (1972).
10. C. Townes and A. Schawlow, *Microwave Spectroscopy* (McGraw-Hill, New York, 1955), p. 426, in the context of microwave spectroscopy; proposed in the present context by R. Drever, California Institute of Technology, Pasadena, Calif. 91125 (personal communication, 1986).
11. D. Shoemaker, P. Fritschel, J. Giaime, N. Christensen, and R. Weiss, "Prototype Michelson interferometer with Fabry-Perot cavities," *App. Opt.* **30**, 3133–3138 (1991).
12. R. Schilling and L. Schnupp, Max-Planck Institut für Quantenoptik, Garching bei München, Germany (personal communication, 1986).
13. A. E. Siegman, *Lasers* (University Science, Mill Valley, Calif., 1986), pp. 524–530.



Mirror Orientation Noise in a Fabry-Perot Interferometer Gravitational Wave Detector

Seiji Kawamura* and Michael E. Zucker

LIGO Project
California Institute of Technology
Pasadena, California 91125 U.S.A.

ABSTRACT

Separations between suspended inertial test bodies in LIGO (the Laser Interferometer Gravitational-wave Observatory) will be monitored to detect and measure astrophysical gravitational radiation, by using the mirrored surfaces of the test bodies to form Fabry-Perot optical resonators. The influence of test body rotation on the apparent length of such a resonator was analyzed geometrically. The resulting model accurately describes the response of the LIGO 40 meter interferometer to mirror control torques, and a substantial sensitivity improvement was achieved by redesigning the interferometer's mirror control systems. Practical criteria for design of full-scale LIGO mirror suspension and control systems are also derived.

1. Introduction

The LIGO (Laser Interferometer Gravitational-Wave Observatory) will employ Fabry-Perot optical cavities to detect and measure small changes in separation, having characteristic durations of a few milliseconds and magnitudes of order 10^{-18} meter, between inertial gravitational test bodies separated by orthogonal 4 kilometer baselines^{1, 2}. The four test bodies, made of fused quartz, will be polished and coated to form two resonant Fabry-Perot optical cavities. Laser light will be split by a beamsplitter and made to resonate in each of the two orthogonal cavities; the resonant fields are extracted and interfered to measure the difference

* Current address: Institute of Space and Astronautical Science, 3-1-1 Yoshinodai, Sagamihara, Kanegawa 229 Japan.

between their phases, which depend sensitively on the mirror separations. To isolate the test bodies from external forces, they will be suspended as pendula whose natural periods, of order one second, are significantly longer than characteristic signal timescales. Band-limited control systems will damp their rotational rigid-body normal modes, which also have periods of order one second, to maintain optical alignment of the resonators. The required displacement sensitivity places a direct limit on the allowable linear momentum imparted to test bodies by seismic noise, thermal fluctuations, and side effects of the control systems.

Excess noise from angular fluctuations of each mirror, arising from external torques, also influences optical cavity length. A simple geometric model predicting the apparent cavity length change due to test body rotation was developed and evaluated on the LIGO 40 m interferometer testbed. The model accurately predicts the interferometer's response to experimental probe torques applied to its test bodies. Substituting the measured power spectra of residual torques from the interferometer's mirror angle control systems into the model exposed these systems as a dominant limit to its sensitivity at frequencies below 700 Hz. New lower-noise control systems were developed and implemented, resulting in a substantial improvement in displacement sensitivity and providing a basis for full-scale LIGO control systems.

2. Optical Cavity Length

The round trip optical phase for the resonator's TEM_{00} mode, which is measured and interpreted as apparent mirror displacement, depends on the *optical length* l , the length of the line segment which lies perpendicular to both mirror surfaces (i.e. the optic axis). Our objective is to quantify the relationship between the measured quantity l and the desired *inertial length* L , the separation between the test bodies' centers of mass, as each body rotates in response to external torques. We will employ the orthogonality of small rotations about the two relevant mutually perpendicular axes ("altitude" and "azimuth") to treat their influences on l independently; thus, in what follows, the normals to both mirrors and the line joining the test bodies can be assumed to lie in a common plane. We will also assume that no net forces are applied (i.e., L is constant).

The optical length of a Fabry-Perot cavity depends on the *deviation angles* θ_1 and θ_2 , defined as shown in Figure 1. These angles are both equal to zero when the optical axis coincides with the line joining the centers of mass of the

test bodies. To second order in θ_1 and θ_2 , which are presumed to be small, the optical length of the cavity is given by

$$l = l_0 + \alpha\theta_1^2 + \beta\theta_2^2 + \gamma\theta_1\theta_2 \quad (1)$$

where, for the half-symmetric cavity geometry illustrated[†],

$$\alpha = \frac{1}{2}(R + a_2 - L) \quad \text{and}$$

$$\beta = -\frac{\gamma}{2} = \frac{1}{2}(R + a_2) .$$

Here R is the radius of curvature of the concave mirror M_2 and $l_0 \equiv L - a_1 - a_2$ is the optical length when $\theta_1 = \theta_2 = 0$. The time evolution $l(t)$ can be computed from (1) for arbitrary $\theta_1(t)$ and $\theta_2(t)$.

For typical cases of experimental interest, θ_1 and θ_2 will be random processes, whose properties are summarized by measured power spectral density functions. We are interested in estimating the power spectrum of the resulting random process l for comparison with expected signals and other noise. Since the power spectrum is the expectation value of the squared modulus of a random process' Fourier transform³, we begin by transforming (1) into the frequency domain[‡]. By the convolution theorem, the transform of (1) can be written

$$\tilde{l}(f) = l_0\delta(f) + \alpha\tilde{\theta}_1 \otimes \tilde{\theta}_1(f) + \beta\tilde{\theta}_2 \otimes \tilde{\theta}_2(f) + \gamma\tilde{\theta}_1 \otimes \tilde{\theta}_2(f) \quad (3)$$

where $\delta(f)$ is the Dirac delta function and the operator \otimes denotes convolution;

$$\tilde{a} \otimes \tilde{b}(f) \equiv \int_{-\infty}^{\infty} a(f') b(f - f') df' . \quad (4)$$

The application to gravitational wave detection permits a significant simplification of (3). Terrestrial gravitational wave detectors will monitor $l(t)$ only at frequencies above a few tens of Hertz, while the alignment errors θ_1 and θ_2 are

[†] Equation 1 and the rest of the discussion can be readily applied to any cavity geometry by suitably redefining α , β , and γ . In the general case, β and γ are not linearly dependent.

[‡] We will later replace each angle fluctuation's Fourier transform with the square root of the spectral density of the corresponding random process, and take the result to be the square root of the spectral density of l . For this substitution to be justified the phases of the Fourier components must truly be random, that is, Fourier components at different frequencies must not on average be correlated. True random noise processes like those considered here will satisfy this criterion⁴.

dominated by static ("D.C.") or slowly varying component (at frequencies below 10 Hz). Faster angle fluctuations, at frequencies within the observation band, will be considerably smaller. Such a spectrum of angle noise arises, for example, from long term thermal drifts and from the increase of seismic vibration amplitude with decreasing frequency. In such a situation we may write

$$\theta_\nu(t) = \bar{\theta}_\nu + \epsilon_\nu(t) \quad (5)$$

where $|\epsilon_\nu(t)| \ll |\bar{\theta}_\nu|$,

$$\bar{\theta}_\nu \equiv \frac{1}{T} \int_{-T/2}^{T/2} \theta_\nu(t) dt$$

is the average taken over some long interval T , and $\nu = 1$ or 2 for mirror M_1 or M_2 , respectively. To leading order in $\epsilon_\nu/\bar{\theta}_\nu$ we find

$$l(t) \simeq l_0 + \frac{1}{2} \bar{d}_1 [\bar{\theta}_1 + 2\epsilon_1(t)] + \frac{1}{2} \bar{d}_2 [\bar{\theta}_2 + 2\epsilon_2(t)] \quad , \quad (7)$$

where the quantities

$$\begin{aligned} d_1 &\equiv 2\alpha\theta_1 - 2\beta\theta_2 \text{ and} \\ d_2 &\equiv 2\beta(\theta_2 - \theta_1) \end{aligned} \quad (8)$$

are the moment arms separating the perturbed optic axis (i.e. the position of the resonating beam on each mirror) from each test body's center of rotation (Figure 1). The Fourier transform of (7) is then simply

$$\tilde{l}(f) \simeq \bar{d}_1 \tilde{\epsilon}_1(f) + \bar{d}_2 \tilde{\epsilon}_2(f) \quad (f \neq 0) \quad , \quad (9)$$

agreeing with the intuitive notion that the apparent displacement of the portion of the mirror at the beam location is given by the angle fluctuation multiplied by the moment arm.

Equation (9) can be generalized if we let $\bar{\theta}_\nu$ be a large (in the mean-square sense) slowly varying, rather than static, misalignment. If the dominant misalignment is confined to a small region of the spectrum $|f| < |w|$, we can write

$$\tilde{\theta}_\nu(f) = \tilde{\theta}_\nu^w(f < w) + \tilde{\epsilon}_\nu(f > w) \quad (10)$$

where

$$\int_{-w}^w |\tilde{\theta}_\nu^w(f)|^2 df \gg \int_{-\infty}^{\infty} |\tilde{\epsilon}_\nu(f)|^2 df \quad (11)$$

(i.e. the low-frequency portion carries substantially more spectral power than the high-frequency portion). We then find the analogous expression to (9), again to leading order, is

$$\tilde{l}(f) \simeq \int_{-w}^w \tilde{d}_1(f') \tilde{\epsilon}_1(f-f') df' + \int_{-w}^w \tilde{d}_2(f') \tilde{\epsilon}_2(f-f') df' \quad (f > 2w). \quad (12)$$

This result can also be derived by restricting the range of the convolution integrals in (3) to frequencies where at least one parent spectrum carries significant power.

For a static misalignment, $\tilde{d}_\nu(f) = \bar{d}_\nu \delta(f)$, we recover Equation (9) and a mirror angle fluctuation at frequency f_0 linearly induces a Fourier component of optical length at the same frequency. This can be shown to give an adequate prediction of the optical length spectrum, without resorting to the more general form (12), if $\bar{d}_\nu \gg d_\nu^{rms}$, where

$$(d_\nu^{rms})^2 \equiv \frac{1}{T} \int_0^T [d_\nu(t) - \bar{d}_\nu]^2 dt = \int_{-w}^w |\tilde{d}_\nu(f)|^2 [1 - \delta(f)] df \quad (13)$$

is the mean-square deviation of the optic axis (excluding the static offset).

On the other hand, if $\bar{d}_\nu \lesssim 2 d_\nu^{rms}$ the optical path length spectrum will not be linearly related to the angle spectra and will contain frequency-shifted sideband products. Nevertheless, in common situations the high-frequency mirror angle spectra $\tilde{\epsilon}_\nu(f)$ are smooth and nearly constant over a band of frequencies $\Delta f \gtrsim 2w$. Such spectra arise from electronic noise in the mirror control system or thermal fluctuations in the suspension, for example. We can then derive the approximation

$$|\tilde{l}(f)|^2 \approx \left[\bar{d}_1^2 + (2d_1^{rms})^2 \right] |\tilde{\epsilon}_1(f)|^2 + \left[\bar{d}_2^2 + (2d_2^{rms})^2 \right] |\tilde{\epsilon}_2(f)|^2 \quad (f > 2w). \quad (14)$$

Under the above conditions, we may replace the squared Fourier transforms with the power spectral densities $S_{\epsilon_1}(f)$ and $S_{\epsilon_2}(f)$ of random processes ϵ_1 and ϵ_2 to obtain

$$S_l(f) \approx \left[\bar{d}_1^2 + (2d_1^{rms})^2 \right] S_{\epsilon_1}(f) + \left[\bar{d}_2^2 + (2d_2^{rms})^2 \right] S_{\epsilon_2}(f) \quad (f > 2w), \quad (15)$$

where $S_l(f) \equiv \lim_{T \rightarrow \infty} 2 |\tilde{l}(f)|^2 / T$ is the power spectral density of induced cavity length fluctuation.

3. Experimental Tests

This model was tested on the LIGO 40 meter interferometer⁵. Briefly, this instrument comprises two orthogonal 40 m cavities whose 1.5 kilogram test bodies are suspended by wires so they are essentially free to translate in a horizontal plane and to rotate about axes perpendicular to the laser beam (Figure 2). Referring to Figure 1, the geometrical parameters of each cavity are $R = 62$ m, $L = 40$ m, and $a_1 = a_2 = 6$ cm.

The pendulum mode and both rotational normal modes of the suspended bodies have eigenfrequencies near 1 Hz. Each is controlled in azimuth (ϕ) and elevation (θ) by a control system which derives appropriate feedback signals from an optical lever sensor and applies magnetic corrective torques to the suspension. Manual offsets can be introduced and trimmed to adjust and optimize (or degrade) the alignment of the two cavities.

The control electronics are provided with summing nodes through which probe signals are introduced to measure the transfer characteristics for various degrees of freedom. The induced rotations are calibrated by measuring the motion of the optical lever reflections. The interferometer's differential displacement output signal, which represents the difference between the cavity optical lengths, is monitored and itself periodically calibrated against a known test force applied electromagnetically to one test body. The differential displacement induced by the probe signal reflects the change in the length $l(t)$ of the probed cavity. This length signal is Fourier analyzed with a digital spectrum analyzer to pick out the components resulting from the probes (while discriminating against other components) and to measure their power spectra.

In the presence of a large static D.C. misalignment \overline{d}_ν between the cavity axis and one mirror's center of mass, Equation (9) implies that the coupling of that mirror's angle to apparent cavity length will be $\tilde{l}(f)/\tilde{\epsilon}_\nu(f) = \overline{d}_\nu$. To test this prediction, a small sinusoidal probe torque resulting in a vertical oscillation $\epsilon_2(t) = a \cos(2\pi f_0 t)$ was applied to one mirror (M_2 in Figure 1) at $f_0 = 250$ Hz. The interferometer cavity length signal was recorded as the vertical distance \overline{d}_2 between the cavity axis and the center of that mirror was varied by adjusting the

alignment controls for both mirrors and the direction of the incident laser beam. The true position of the cavity axis was monitored by photographing scattered light from the resonating cavity mode against the outline of the mirror. Figure 3 shows the measured ratio $\tilde{l}(f_0)/\tilde{\epsilon}_2(f_0)$ vs. \overline{d}_2 . Since the exact position of the test body's center of mass is not accurately known, we have chosen the reference point $\overline{d}_2 = 0$ to best fit the measured data; the slope, however, clearly exhibits the expected proportionality.

In more realistic situations, the mirror angle spectra will consist of many uncorrelated components, so the cross products of many different frequency pairs will generally be superimposed at each frequency in the convolved result. To investigate this case, a band-limited random noise test signal was generated to induce random angle fluctuations of M_2 principally between 200 and 315 Hz ,

$$|\tilde{\epsilon}_2(f)| \approx \begin{cases} 0, & f \lesssim 200 \text{ Hz} \\ K, & 200 \text{ Hz} \lesssim f \lesssim 315 \text{ Hz} \\ 0, & f \gtrsim 315 \text{ Hz} \end{cases} \quad (16)$$

where K is a constant. The cavity length's spectral density was monitored in this frequency band as a function of \overline{d}_2 . As shown in Figure 4, the magnitude of the effective transfer function for this random noise probe signal is approximately proportional to the magnitude of \overline{d}_2 at large offsets, as in Figure 3, but remains essentially constant for very small \overline{d}_2 . To investigate this behavior, the light transmitted through M_2 was analyzed with a position-sensing quadrant photodetector to measure low-frequency fluctuation of the cavity axis position $\tilde{d}_2(f \ll f_0)$. Integrating this position spectrum over frequency (and excluding D.C. as in Equation (13)) gave $d_2^{rms} \approx (0.2 \pm 0.1)$ mm. From Equation (15) we expect the linear proportionality approximation to fail for $|\overline{d}_2| \lesssim 2d_2^{rms} \approx (0.4 \pm 0.2)$ mm, essentially the region in which the data shown in Figure 4 deviate from the linear prediction. While the method used to obtain the data in Figures 3 and 4 can be used for each mirror to empirically adjust all \overline{d}_ν precisely to zero, the average coupling coefficient will generally reach a nonzero minimum of order $2d_\nu^{rms}$.

To quantitatively test (12) a two-frequency probe signal

$$\tilde{\theta}_2(f) = \theta_2^a \delta(f_a) + \epsilon_2 \delta(f_b) \quad (17)$$

was imposed on M_2 with a large low-frequency component ($\theta_2^a = 1.6 \times 10^{-6}$ rad_{rms}, $f_a = 10$ Hz) and a small high-frequency component ($\epsilon_2 =$

$5.0 \times 10^{-9} \text{ rad}_{rms}$, $f_b = 250 \text{ Hz}$). The natural $\tilde{\theta}_2(f)$ spectrum was small enough to be completely dominated by these probe components in their respective frequency regimes. The cavity length signal displayed the expected pair of equal-amplitude Fourier components at 260 Hz and 240 Hz, with measured amplitudes of $(3.9 \pm 1.0) \times 10^{-13} \text{ m}_{rms}$; direct substitution of the probe spectrum (17) into Equation 12 would predict

$$\tilde{l}(f) = 3.4 \times 10^{-13} \text{ m}_{rms} \times [\delta(f_b + f_a) + \delta(f_b - f_a)], \quad (18)$$

agreeing within measurement errors.

The $f_a = 10 \text{ Hz}$ component of the probe rotation was then removed and the 250 Hz test signal was reduced in amplitude to $\epsilon_2 = 1.5 \times 10^{-9} \text{ rad}_{rms}$. Analysis of the cavity length spectrum then revealed natural sidebands, symmetric around the 250 Hz probe. The vertical position of the cavity axis at M_2 was simultaneously measured by the transmitted-beam quadrant photodetector. The detailed spectral shape found for the cavity length signal matches the spectrum of cavity axis position, upshifted by 250 Hz and with an amplitude close to that predicted by Equation 12 (Figure 5). In effect, the monochromatic 250 Hz probe has acted as a virtual delta function in the convolution integral, “picking out” of the convolution an upshifted replica of the residual low-frequency beam offset spectrum.

4. Application to the 40 m Interferometer

Measurements in mid-1991 indicated that mirror orientation fluctuation was a significant source of noise in the 40 m interferometer⁶. High-frequency mirror angle fluctuations can arise from seismic excitation, thermal noise, or other natural phenomena. However, the dominant term in the total angular noise of the 40 m interferometer’s test bodies was actually introduced by the mirror control systems. These terms originated as a combination of direction and intensity noise in the optical lever lasers and electronic noise in the control electronics, and were transmitted to the test bodies as a result of inadequate filtering outside the control band (D.C. to 10 Hz). Measuring the transfer functions from probe signal to mirror angle for each degree of freedom of each test body, and the total noise of the control system for that degree of freedom, allowed an estimate for each test body’s contribution to the instrument’s displacement spectrum. The sum of these contributions coincided closely with the observed noise spectrum at frequencies between 50 and 700 Hz. Temporary noise reductions could be achieved by

iteratively adjusting the cavity alignment to empirically reduce \overline{d}_v for the noisiest of the interferometer mirrors, or by temporarily reducing the gain of the control systems (accepting some degradation in control performance).

Improved orientation feedback electronics were developed and tested to permanently reduce this source of noise without compromising control loop effectiveness. The redesigned system has a lower unity gain frequency (1–3 Hz compared to the previous value of 10 Hz), greatly increased filter attenuation above 20 Hz, and lower intrinsic electronic noise. The improved controllers gave a drastic reduction of displacement noise due to mirror angle fluctuation, by a projected factor of up to 10^5 at some frequencies (lower line of Figure 6), leaving the overall interferometer displacement noise spectrum (middle line of Figure 6) limited by other noise sources except at narrow mechanical resonances.

5. Implications for LIGO Interferometers

Initial LIGO interferometers are expected to achieve total displacement noise spectral densities below 10^{-19} m/ $\sqrt{\text{Hz}}$ in order to achieve sufficient sensitivity at frequencies near 100 Hz¹. Equation (15) implies that in order to contribute negligible additional noise at this level, we can permit angular fluctuations no larger than

$$S_{\theta_v}^{1/2}(f) \lesssim 10^{-17} \frac{\text{rad}}{\sqrt{\text{Hz}}} \times \left(\frac{0.5 \text{ mm}}{d_v^{\text{rms}}} \right) \quad (19)$$

for each of the eight independent angular degrees of freedom of the four cavity mirrors[§] at frequencies $f \sim 100$ Hz.

The spectral density of angular fluctuations induced by the improved 40 m interferometer mirror control systems described above reaches approximately 5×10^{-16} rad/ $\sqrt{\text{Hz}}$ near 100 Hz, principally due to electronic noise in their active filters. Assuming the projected $d_v^{\text{rms}} \sim 0.5$ mm is achievable at remote LIGO sites^{||}, it will be necessary to reduce the product of the electronic noise

[§] Here we have omitted the additional linear contribution due to nonzero \overline{d}_v , since it can be empirically trimmed to zero by monitoring the response of each mirror to probe torques; see Figures 3 and 4 and discussion.

^{||} Remote LIGO sites exhibit approximately one tenth the seismic amplitude found in the campus laboratories at frequencies which determine the RMS mirror angle fluctuation. In addition, current seismic isolation stack and suspension designs show one fifth the resonant amplification effect found to greatly enhance RMS mirror motion in the 40 m interferometer. While the hundredfold increase in length would proportionately increase the d_v^{rms} arising from a given RMS angle fluctuation, these factors should reduce that angle fluctuation by a factor of order fifty, leading us to expect only a doubling in net d_v^{rms} in full-scale interferometers.

in the control circuits with the electromechanical coupling to the mirror by a combined factor of 25.

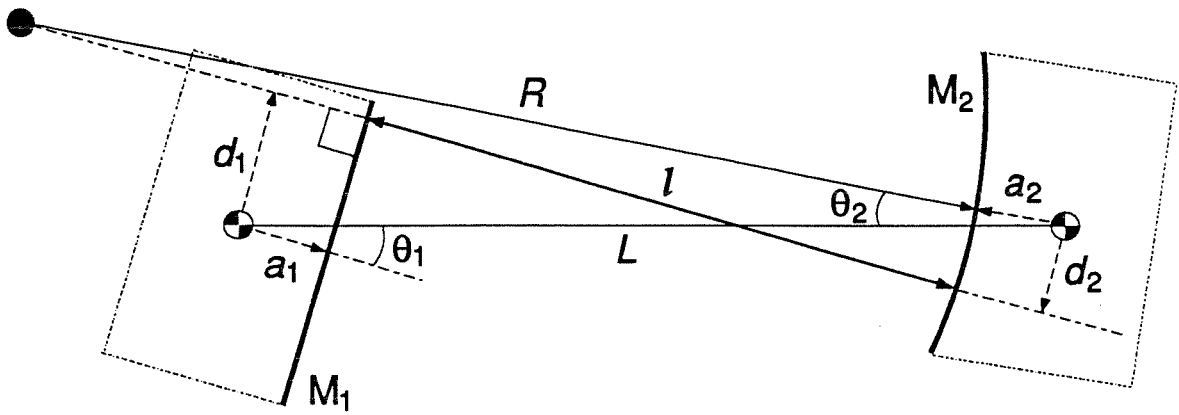
There are several ways to achieve this improvement. Substituting passive or lower-noise active filtering could give a reduction in noise by a factor of order 30 or more at 100 Hz. In addition, if (as preliminary measurements indicate) the remote sites are seismically quieter than the campus laboratory, the dynamic reserve of the controllers can be reduced and the electromechanical coupling of the torque actuators can be cut back accordingly, reducing the torque induced by a given amount of electronic noise in the circuitry. We conclude that with modest improvements of current controller designs, angular motion of cavity mirrors will not limit LIGO sensitivity.

6. Conclusions

Simple geometric considerations appear to adequately model the sensitivity of Fabry-Perot cavities to high-frequency angular rotations of their mirrors, allowing straightforward analysis of torque-induced noise. While the treatment assumes that the mirrors rotate about their principal axes, general mechanical perturbations of optical components can be decomposed into linear translation and rotation about these or other convenient axes.

In addition to guiding the design of improved mirror control systems for the LIGO 40 m interferometer, which greatly enhanced the performance of that instrument, application of the model to planned full-scale observatory interferometers indicates that with available control technology, angular rotations need not compromise LIGO performance at target sensitivity levels.

Acknowledgments: We wish to thank all who contributed to the construction and improvement of the interferometer, and are grateful for the continuing support of LIGO science, engineering and administrative staff. We are especially grateful to Jake Chapsky for designing the improved control electronics and to Aaron Gillespie, Fred Raab, Robert Spero and Stan Whitcomb for their assistance in measuring and analyzing the data and preparing the manuscript. Our work is supported by National Science Foundation grant PHY-9210038.



- center of curvature (M_2)
- ⊕ center of mass

Figure 1 Geometry of a half-symmetric Fabry-Perot cavity consisting of flat (M_1) and concave (M_2) test body/mirrors.

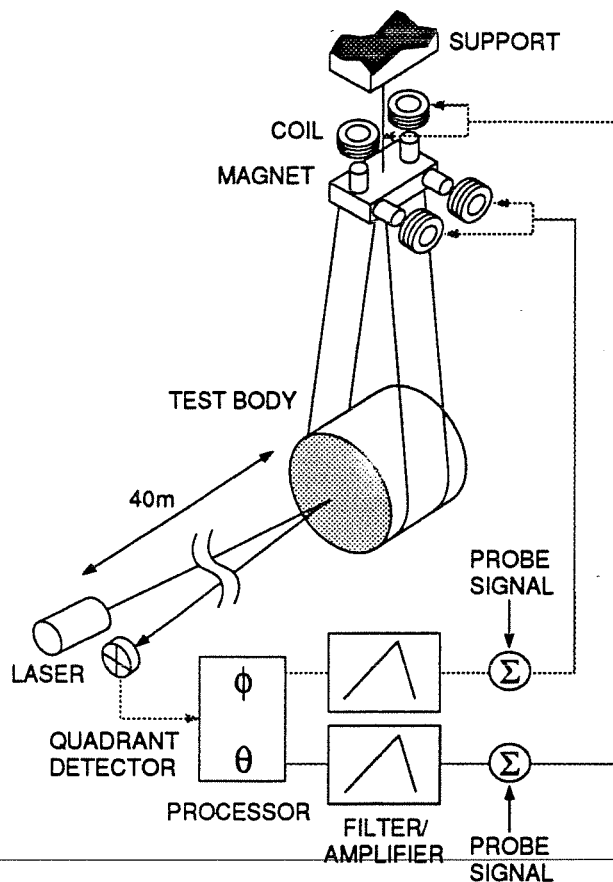


Figure 2 Suspended test body and orientation control system used in the LIGO 40 meter interferometer. The quadrant photodetector and electronic processor determine angular error signals from the position of an auxiliary laser beam reflected from the mirrored surface of the test body. These signals are filtered and amplified and applied to pairs of electromagnetic coils near the suspension point. The coils interact with permanent magnets (poled oppositely to induce torque) on an intermediate platform which is suspended by a single wire so that it is free to rotate. The torque developed on this platform is transmitted to the test body below by the suspension wires, inducing rotation of the mirror and closing the feedback loop. Probe torques are introduced by adding currents to the feedback signals driving the coils.

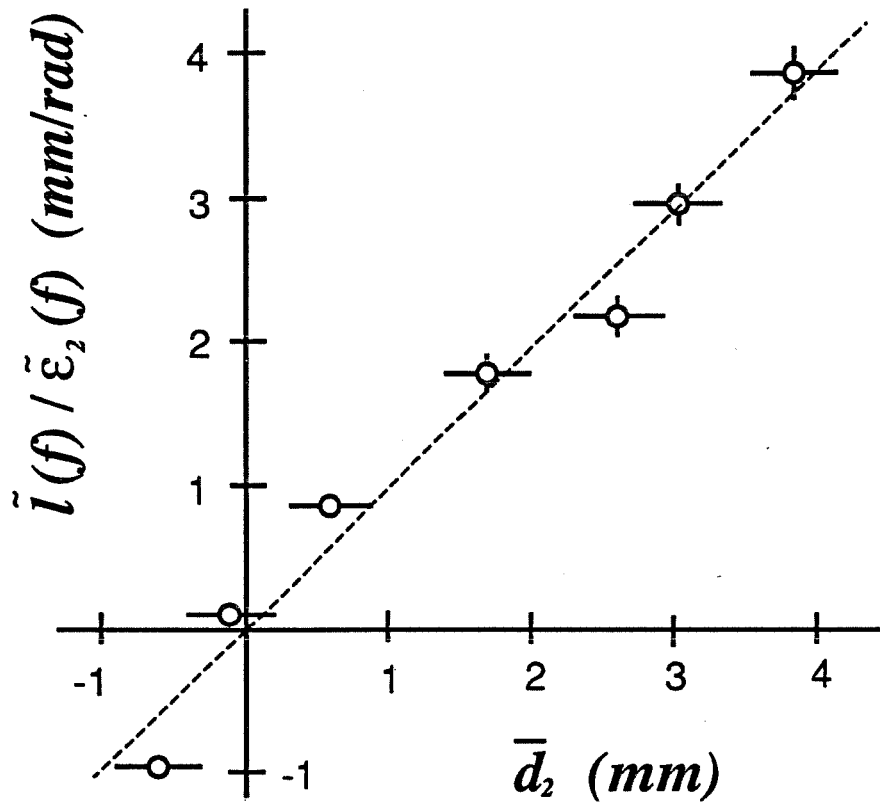


Figure 3 Linear mirror angle—cavity length coupling coefficient $\tilde{l}(f_0)/\tilde{\epsilon}_2(f_0)$ as a function of beam axis position \bar{d}_2 . The dashed line is the curve $\tilde{l}(f_0)/\tilde{\epsilon}_2(f_0) = \bar{d}_2$ predicted by Equation 9. The zero for the \bar{d}_2 axis has been chosen for best fit.

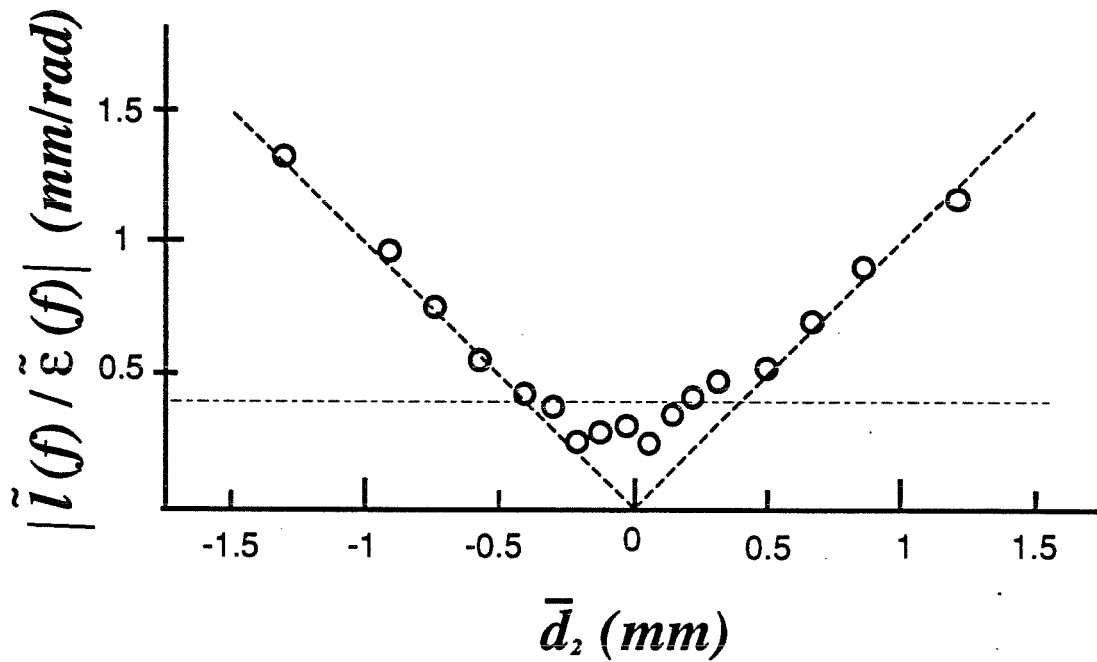


Figure 4 Interferometer displacement due to bandlimited random mirror angle noise as a function of \bar{d}_2 . The coupling magnitude appears proportional to $|\bar{d}_2|$ down to $|\bar{d}_2| \approx 0.4$ mm, below which it is approximately constant. By integrating the spectrum of position fluctuations in the transmitted cavity mode, it was found that $d_2^{rms} \approx 0.2$ mm \pm 0.1 mm during this experiment, in agreement with the transition from linear behavior predicted by Equation (15).

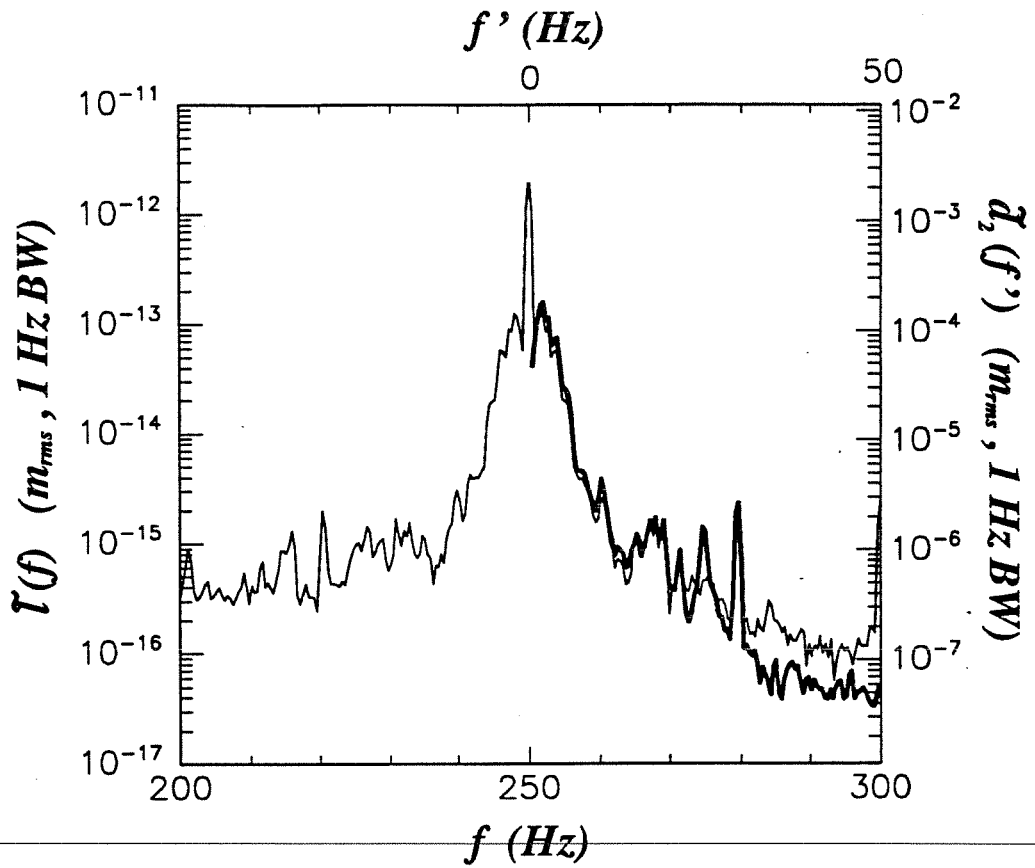


Figure 5 Spectrum of low-frequency beam axis position fluctuations (heavy line, upper frequency scale and right-hand magnitude scale) is replicated as upper and lower sidebands of an artificially induced 250 Hz probe angle fluctuation in the interferometer displacement spectrum (thinner line, lower and left scales). The relative scales are chosen in accord with Equation 12 using the known 1.5×10^{-9} rad_{rms} amplitude of the 250 Hz probe.

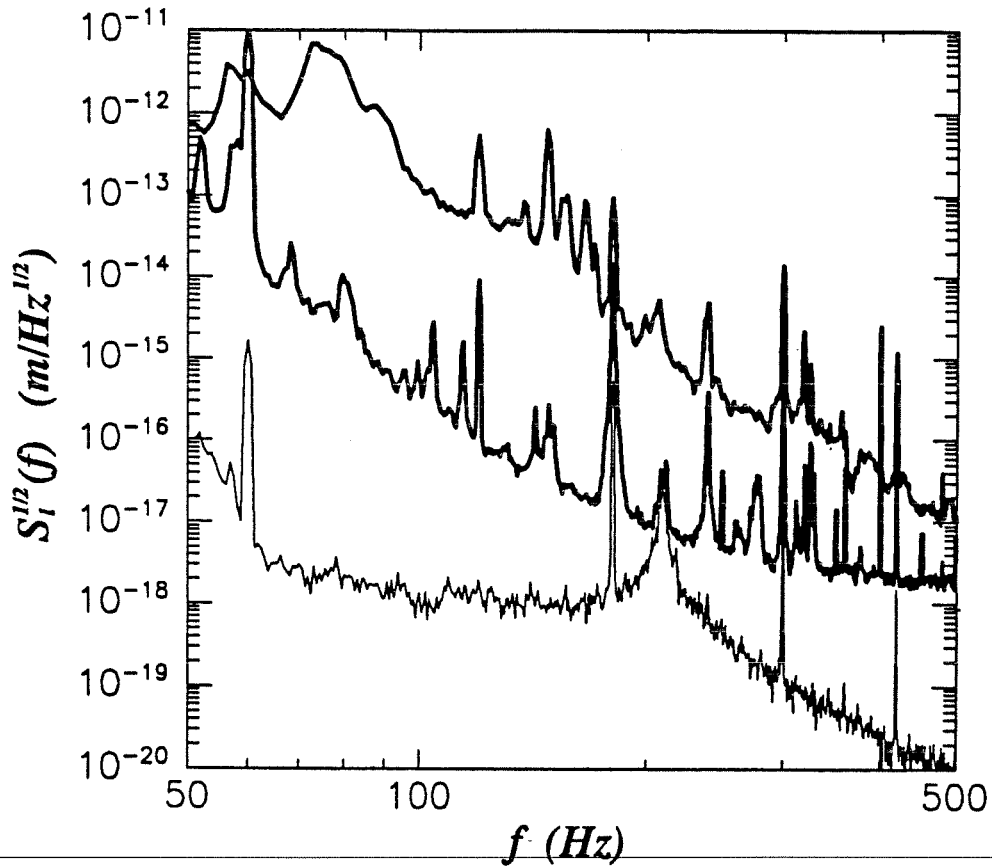
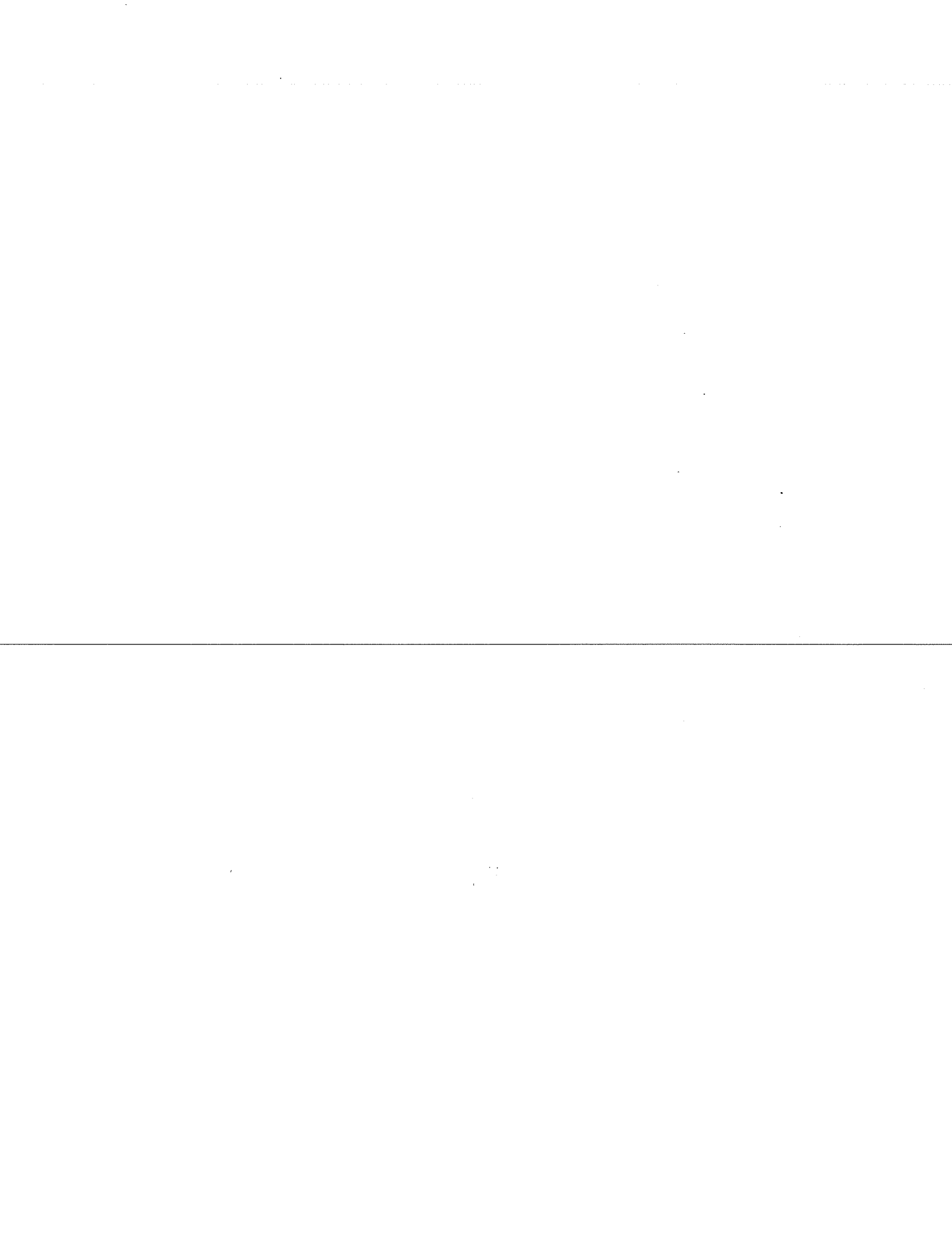


Figure 6 Spectral density of apparent cavity mirror displacement in the 40m interferometer with the original orientation control system (upper curve, heavy line) and after installing the new orientation feedback electronics (middle curve, heavy line). The lower, thin curve depicts the estimated displacement noise induced by residual electronic noise in the new controller for one axis of one test body, using Equation 9 and an assumed $\bar{a}_2 \approx 1$ mm. The peak at 212 Hz is a resonance of the wire suspension system, where the coupling of external torque to the mirror is locally enhanced.

References

1. Alex Abramovici, William E. Althouse, Ronald W. P. Drever, Yekta Gürsel, Seiji Kawamura, Frederick J. Raab, David Shoemaker, Lisa Sievers, Robert E. Spero, Kip S. Thorne, Rochus E. Vogt, Rainer Weiss, Stanley E. Whitcomb, and Michael E. Zucker. LIGO: the laser interferometer gravitational wave observatory. *Science*, **256**, April 17 1992.
2. R. E. Vogt. The U.S. LIGO project. In *Proceedings of the Sixth Marcel Grossmann Meeting on General Relativity, Kyoto, Japan, June 1991*.
3. Robert Grover Brown. *Introduction to Random Signal Analysis and Kalman Filtering*. Wiley, 1983.
4. S. O. Rice. Mathematical analysis of random noise. In Nelson Wax, editor, *Selected Papers on Noise and Stochastic Processes*. Dover, 1954.
5. Michael E. Zucker. The LIGO 40 m prototype laser interferometer gravitational wave detector. In *Proceedings of the Sixth Marcel Grossmann Meeting on General Relativity, Kyoto, Japan, June 1991*.
6. Seiji Kawamura. Test mass orientation noise in the LIGO 40 m prototype. In *Proceedings of the Sixth Marcel Grossmann Meeting on General Relativity, Kyoto, Japan, June 1991*.



A passive vibration isolation stack for LIGO: design, modeling, and testing

Joseph Giaime, Partha Saha, David Shoemaker

LIGO Project, Massachusetts Institute of Technology, Bldg. 20B-145, Cambridge, Massachusetts 02139

Lisa Sievers

LIGO Project, California Institute of Technology, Pasadena, California 91109

(May 21, 1993. DRAFT To be submitted to Reviews of Scientific Instruments.)

Multiple-stage seismic vibration isolation stacks, which consist of alternating layers of dense, stiff material and springs, can provide effective, passive, filtering of ground vibration for experiments that are sensitive to mechanical noise. We describe the design, modeling and testing of a four-stage elastomer/stainless steel stack, consisting of three separate legs of three mass-spring layers each, upon which a single table rests. This design is a prototype isolation system to be used in the Laser Interferometer Gravitational-Wave Observatory (LIGO) project. The stack's transmission of base motion to top motion was measured in vacuum and compared with several 3-D finite-element models. In a particular configuration, designed for use in LIGO prototype experiments, the largest transmission component was measured to be 10^{-6} at 100 Hz.

INTRODUCTION

Interferometric gravitational wave (GW) detectors will use suspended mirrors as gravitational test masses to measure the local strain perturbation in the gravitational metric [1-3]. At the frequencies of interest, from less than 100 Hz to several kHz, the non-gravitational forces on the test masses must be kept as low as possible. Our goal is to develop a prototype seismic isolation system for the Laser Interferometer Gravitational-Wave Observatory (LIGO) [2] that, when used with an appropriate test mass suspension, transmits ground vibration at a level which is small compared with other expected noise sources. Other instrumental applications are possible, for example as a quiet platform for scanning tunneling microscopes [4].

The LIGO interferometers will measure the difference in phase between light that has been stored in two perpendicular 4 km arms. The light is stored in optical cavities formed by freely suspended mirrors which also serve as test masses. Passing gravitational waves cause this phase difference to change with the periodicity of the waves. We expect that the signal-to-noise ratio for the detector will be limited at low frequencies by seismic noise acting on the mirrors and masking the effect of the gravitational waves.

There have been a number of approaches taken to reduce this noise contribution. Multiple pendulums in se-

ries [5,6] attempt to gain isolation by suspending the test masses with wire from a series of similarly suspended "guard" masses. There have been experiments with actively controlled suspension elements [7,8], in which the effective resonant frequency of the isolating harmonic oscillator is lowered using a servo loop.

A straightforward approach, and the one followed here, is the use of a stack consisting of alternating layers of dense stiff material (masses) and light compliant material (springs), which may be roughly described as cascaded lightly damped mass-spring oscillators. Above the resonant frequency of the oscillators, vibration is poorly transmitted. Such stacks are widely used in GW detector prototypes. As the scale and sensitivity of GW detectors grows, it becomes increasingly important to thoroughly understand the seismic isolation system and to have a design procedure in place. Recently, significant progress has been made on this front, for both interferometric and resonant-bar GW detectors. [9,11,12]. We report here on the development of a prototype seismic isolation system for use in the LIGO project.

This mass-spring stack design is based upon the following three features. First, we use elastomers as our spring material. Elastomers have internal visco-elastic damping, which both damps resonances within the spring elements, and damps the overall resonances of the stack structure without compromising high-frequency isolation. Second, the masses are sufficiently compact and stiff so that their internal resonances, which would be difficult to damp, have frequencies of at least several kilohertz, which is far above the important GW band. Finally, the stack consists of separate legs of mass-spring layers, upon which a single table rests. This design allows compact masses to be incorporated in an overall structure that has no resonances within the GW band.

This article is organized as follows. There is a discussion of the requirements and constraints in designing a stack for use in a laser interferometer gravitational wave detector. Matrix notation is defined to be used for the vibration transmission requirements and measurements, and our choice of elastomers, Fluorel and RTV615, is discussed.

Next, there is a description of vibration-transmission tests for two configurations of this basic design. Both configurations used three legs of three 100 kg stainless steel cylinders each as the masses with a 78 kg aluminum table spanning the three legs. What we will call

“stack A” used springs made from Flourel, a fluorcarbon elastomer, between the layers. “Stack B” substitutes RTV silicone rubber springs in the upper two layers. These tests were carried out in vacuum for vertical and horizontal dynamic response to vertical and horizontal excitation, which allowed measurement with a sensitivity to transmission of below 10^{-7} .

Last, we compare the experimental data with three-dimensional finite-element models in order to better understand our measurements, the sensitivity of the design to imperfections, and the usefulness of such models in isolation stack design.

I. STACK DESIGN REQUIREMENTS

There are a number of requirements which constrain our design choices. Some constraints follow from the seismic isolation needed in our system, which determines our vibration transmission requirement. Others result from the stack’s physical properties, including its spring material’s behavior in vacuum, and long term drift.

A. Vibration transmission

1. Stack transfer functions

To explain the isolation requirements, we first set the notation: If the stack’s base and top structures are rigid at the frequencies being considered, its motion may be described by three displacement and three angle coordinates. Let z describe vertical, and x and y horizontal displacements. We label the angles as rotations about each of the displacement coordinate axes, θ_x , θ_y , and θ_z . The displacements at the base and top will be written as vectors in terms of these coordinates. The vibration transmission, $T_{ij}(f)$, from bottom to top is therefore a 6×6 matrix of complex functions of frequency, with i and j ranging over the displacement and angle coordinates. The transmission may be described in the frequency domain because the force-displacement relations for the system’s components are linear over the approximately 10^{-6} m motions encountered in our tests. Motions are transmitted from the base (drive) of the stack to the top as

$$X_{\text{top}}(f) = T(f) X_{\text{drive}}(f). \quad (1)$$

If the stack rests on a structure that is rigid over the frequency span being considered, and whose tilt motions are sufficiently small, then X_{drive} is that structure’s displacement spectral density. For simplicity, and taking into account the roughly cylindrical symmetry of the stack being considered, transmission transfer functions will hereafter be written in terms of only the vertical coordinate, z , and an arbitrary horizontal coordinate, x , although the finite-element (FE) analysis was done in

three dimensions and, of course, the experimental stack was 3-D. This simplification ignores the effects of angular motion in the base and top. As we will describe below, our drive platform can couple horizontal motion to tilting. One might therefore wish to use the tilt angle θ_y , hereafter referred to as θ , as a dynamic variable to supplement the description in terms of x and z under certain circumstances.

Thus, vibration transmission takes the form

$$\begin{pmatrix} x_{\text{top}}(f) \\ z_{\text{top}}(f) \end{pmatrix} = \begin{pmatrix} T_{xx}(f) & T_{xz}(f) \\ T_{zx}(f) & T_{zz}(f) \end{pmatrix} \begin{pmatrix} x_{\text{drive}}(f) \\ z_{\text{drive}}(f) \end{pmatrix}, \quad (2)$$

$$\text{or, } X_{\text{top}} = T X_{\text{drive}}, \quad (3)$$

where the drive and top displacement vectors represent the spectral density of displacement noise applied to the bottom of the stack and measured at the top of the stack, respectively. In the steady-state sinusoidally-driven case, T_{ij} is also the transfer function for acceleration and velocity. We actually measure the acceleration.

With this framework, we can discuss the requirements for the seismic isolation system.

2. Attenuation in the gravity wave band

For the purpose of assessing the ability of the stack to meet our attenuation requirements, we assume the seismic noise that drives the stack to be isotropic along the x , y , and z axes, with the following spectral density: $10^{-9}/f^3$ m/ $\sqrt{\text{Hz}}$ from 0.1 to 1 Hz, 10^{-9} m/ $\sqrt{\text{Hz}}$ from 1 to 10 Hz, and $(10^{-7}/f^2)$ m/ $\sqrt{\text{Hz}}$ from 10 Hz to 10 kHz. This spectrum is based on measurements in a number of laboratories and ground-noise surveys [13,2].

A complete isolation and suspension system for our application in interferometric GW detectors consists of an isolation stack and a pendulum suspension for the test mass. The pendulum suspension offers some isolation in both the vertical and horizontal axes [9,6]. The GW detector is principally sensitive to motion along an x (horizontal) axis, thus constraining T_{xx} and T_{xz} . The earth’s curvature over the 4 km length of the LIGO GW detector gives a coupling in the pendulum suspension from motion in the z axis to motion along the x sensing axis of at least 3×10^{-4} , constraining T_{zz} and T_{zx} . This is because the direction of the earth’s gravity is slightly different at each vertex of the interferometer. Additional cross-coupling in the test-mass suspension may also be possible. The mechanical support structure between the stack and the pendulum, which is not within the scope of this article also converts tilting motion of the stack top plate, θ , into motion along the x axis.

We set a performance goal for this isolation stack so that the seismic noise contribution to LIGO’s expected signal-to-noise ratio (SNR) will not significantly influence the detection rate of predicted GW sources. The mirror

motion noise contributed by seismic noise is the native ground noise, filtered by the stack and pendulum transfer functions. This contribution to the denominator of the SNR is falling very rapidly with frequency in the region above the stack resonances. A competing noise below about 200 Hz is expected from the thermal excitation of the mirror pendulum suspension [14,2]. Above 200 Hz, "shot noise," or photon counting statistics, will dominate. The most important figure-of-merit for our seismic isolation system is the frequency at which its noise contribution equals that of the expected thermal noise of the LIGO pendulum design. The lower this frequency is, the better, but continued reduction leads to diminishing improvement in detection rate [10].

With this in mind, we set as a requirement that the crossover be below 100 Hz. This results in a maximum seismic transmission for our application of 10^{-5} at frequencies above 100 Hz for T_{xx} and T_{zz} , which couple to horizontal motion, and approximately a factor of 10 less for T_{xz} and T_{zx} , which couple to the vertical. Improvements beyond this requirement may improve the sensitivity of the GW detector by reducing indirect contributions from cross-couplings, and are still desirable.

3. Motion amplification at rigid-body resonances

Rigid-body resonances are those for which the solid masses of the stack behave as perfectly rigid bodies applying forces to one another through the low-mass spring elements. The transmission peaks due to rigid-body stack resonances, in the high-ground-noise region below 10 Hz, must be damped well enough that the motion on top does not exceed the gravity wave antenna servo system's ability to suppress this motion because of dynamic range or gain-bandwidth limitations. Since the low frequency (below 1 Hz) motion dominates the integral to calculate x_{rms} , it would seem that high- Q peaks at several hertz wouldn't contribute very much to the displacement noise, if one only considers 'stationary' random ground noise. However, impulse or step excitations might excite high- Q resonances. The optical and control systems may contain non-linearities, which can lead to upconversion of the motion at low frequencies to signals at GW frequencies (roughly 50 Hz to 5 kHz); or, if noise is coupled to the mirrors through magnetic fields, which push the small control magnets to be attached to them, any eddy current sites on the isolation stack would contribute in proportion to their velocity, not position, enhancing the contribution from the rigid-body modes. These considerations suggest against a design with transmission peaks of Q greater than of order ten.

B. Physical properties

a. Static characteristics The top of the prototype stack needs to support a load of up to 150 kg, consisting of various suspension, test mass/mirror, and control elements for the interferometer. With this load, the stack must have a long-term drift consistent with the ability of the rest of the isolation/suspension system to compensate. A stack drift of several mm per year, beginning a few months after assembly, is acceptable. In addition, short-term temperature drifts must not result in motions of the stack which exceed the interferometer servo system's short-term dynamic range.

b. Vacuum compatibility Since interferometric gravity wave detectors will operate in very high to ultra high vacuum, and since the large size of LIGO's vacuum systems precludes high pumping capacity, the materials used for the stack must have low outgassing properties. In addition to the simple outgassing rate, the contamination of nearby low-loss optics must be held to an acceptable level.

II. THE DESIGN

A. Design approach

The basic stack design can be thought of as four cascaded harmonic oscillators. The lower three oscillators consist of layers of three 100 kg stainless steel cylinders resting on layers of 70 durometer Fluorel or RTV elastomer rubber springs, forming three 'legs' of three cylinders each. The final layer is a single 78 kg circular aluminum table supported through three rubber springs on the three legs below. To predict the response of the stack to horizontal motion, it was necessary to carry out numerical simulation. However, the vertical response to vertical excitation, $T_{zz}(f)$, can be accurately described as four cascaded one-dimensional oscillators. At frequencies well below a single oscillator's resonance frequency, f_0 , there is unity transmission. Near the resonance, the transmission is enhanced by approximately the Q of the oscillator. Well above the resonance, the transmission falls with frequency as $(f_0/f)^n$, where n lies between 1 and 2 and depends on the dissipation mechanism in the springs and on the Q . When four such layers are cascaded, the resonance peaks in $T_{zz}(f)$ will be spread in frequency and will correspond with the frequencies of the four rigid-body modes that have predominantly vertical mode shapes. Well above the resonances, $T_{zz}(f)$ will fall approximately as the product of the individual stages' responses.

The stack's response to horizontal excitation is not as easy to predict with simple arguments as the vertical response, since this kind of drive couples into complicated modes involving both tilts and translation of the solid el-

ements; the numerical analysis used to describe the horizontal motions will be discussed below.

There are also high frequency internal modes in the solid mass and spring elements. The approach we took in this design was to make the rigid-body modes low Q , to place them below the frequencies where we needed high isolation, and to make all of the internal modes high enough in frequency that they would be well filtered by the rest of the stack, despite their high Q . This requirement led to compact structures of steel to be used as the masses, and rubber as the springs.

B. Selection of spring materials

A major design concern was to find a material for the springs compatible with vacuum use, which could be incorporated in a stack design which meets the above criteria. Two will be discussed: Fluorel and RTV.

Fluorocarbon elastomers, often known by their trademarked names Viton and Fluorel, for example, are widely used as seal materials for high vacuum systems. We investigated the dynamic properties of injection molded 3M-Fluorel 2176 by measuring the real and imaginary parts of the elastic modulus over the range of interesting frequencies. For the frequency region in which we expect resonances, the ratio of real to imaginary modulus is approximately 3. This means that a harmonic oscillator using this as the spring element will have resonance Q s of that order as well. We found that the real part of the elastic modulus grows slowly with excitation frequency, and that the imaginary part of the modulus grows faster, as approximately the square root of frequency. A system consisting of a viscous (velocity-proportional) damper in parallel with a hooke-law spring, if analyzed in terms of a complex spring constant, would have an imaginary part linearly proportional to the drive frequency. The behavior of the Fluorel is typical of visco-elastic damping found in various materials. The advantage of this form of damping to our application is that while the modal resonance peaks are well damped, well above these frequencies the transmission falls nearly as $(f_0/f)^2$ per oscillator stage, where f_0 is the oscillator's resonance frequency. The transmission of a viscously damped system with a similar resonance Q would fall less steeply, providing less high frequency isolation.

We also characterized GE RTV615 silicone rubber, for which we also had some experience in preparation for vacuum use [15]. The RTV's modulus was lower than that of the Fluorel, and mostly real, indicating that a mechanical oscillator made with RTV springs would have a Q an order of magnitude higher than one with Fluorel. The use of a combination of these materials allows a trade-off between the high damping and low rigid-body-mode resonant frequencies we desire.

Although the modulus vs. frequency data allow the prediction of the system's dynamic response, it is impor-

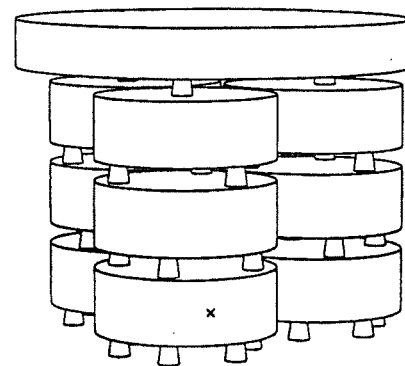


FIG. 1. Perspective drawing of the isolation stack. The overall height is 68 cm. The width is 78 cm.

tant to note that lossy elastomers such as Fluorel strain over time in response to constant stress. For very long times, of order at least hundreds of seconds, these materials often exhibit a creep described by $\delta l/l \sim \log(\text{time})$. We also observed a short-time relaxation of the material, which occurs over tens of seconds after loading. Experimentally, we determined that the overall strain on the springs should not exceed about 20% to limit the creep to acceptable levels; this initial deformation limits the load capacity of the Fluorel. This long-term behavior is not well described by the modulus vs. frequency data, and was not observed in the RTV.

III. EXPERIMENTAL TESTS

A. Configurations Tested

The stack is drawn in perspective in Fig. 1. The leg elements were made from 12.7 cm (5 in.) long by 35.6 cm (14 in.) diameter cylinders of type 304 stainless steel. These pieces were approximately 100 kg each, and we calculate that all of their internal resonances lie above 3 kHz. Springs, to be described below, are held in place between these leg masses by friction. The table, made of aluminum, measures 78.49 cm in diameter and 9.52 cm in height, and consists of a 2.54 cm thick top plate welded to a 7.0 cm by 7.6 cm ring, with 2.54 cm wide radial webbing welded inside, for stiffness. Another of these tables was used as the platform on which the entire stack was constructed. The only table resonances below 1 kHz were measured at 467 Hz and 825 Hz, with Q s of approximately 500.

We present results from tests of two spring configurations: "Stack A" was assembled with springs made with

Fluorel [16]. These springs measure 5.08 cm high, uncompressed, and after compression and settling measured, by layer from top to bottom, 4.52, 4.19, 4.04, and 4.07 cm in height. The number of springs per layer, per leg, top to bottom, was 1-3-4-6, making a total of 42 spring in the stack. The "Stack B" configuration was identical to the first in the lower two layers, but used RTV springs for the upper layers. The RTV springs measured approximately 3.4 cm long uncompressed, and 2.7 cm compressed on both layers.

B. Dynamic Measurements

In order to characterize each stack's dynamic response over the frequency range of 1-350 Hz, three methods had to be used. These tests were performed in a vacuum chamber which was pumped down to less than 10^{-4} mbar for all measurements requiring sonic isolation.

1. Mid-frequency measurements

The most straightforward measurements were made in the frequency range of approximately 20 to 90 Hz, covering the part of the transfer function over which the vibration transmission drops from about a few tenths to about 10^{-4} . For this series of measurements, the stack was built on a base table which itself was resting on three stiff springs. Two electromagnetic shakers were used to excite motion in the base: one mounted horizontally on the drive table side, and one oriented vertically, mounted on the center of the table's underside. Accelerometers were attached to reference points on the lower table and top table, with an accelerometer in each location for each of the directions defined by the two drivers. These reference points were near each table's edge, in order to make them sensitive to both tilt and translation of the tables, so that phenomena involving one or both of these motions would not be missed. We then applied a frequency-swept sine wave drive of approximately $5 N_{\text{rms}}$ to the bottom, vertically, and recorded the transfer functions T_{zz} and T_{xz} , by taking the vector ratios (that is, taking into account both magnitude and phase) of the signals on the top to those on the bottom. Similarly, horizontal drive was used to measure T_{xx} and T_{zx} . This drive level produced very small motions in the drive table, less than a micron at 100 Hz, so we have assumed that the elastomers are behaving approximately as they would for the ground noise drive expected in the intended application.

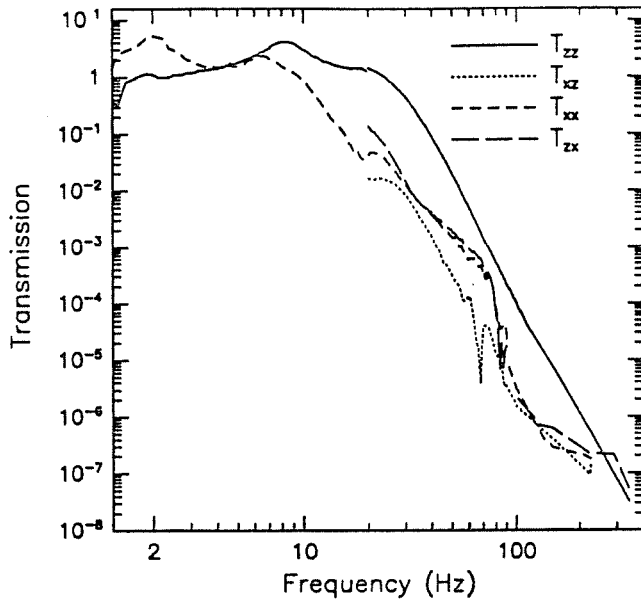
2. Low-frequency ground-noise-driven measurements

At low frequencies, the stack's response is strongly influenced by the exact shapes and frequencies of the

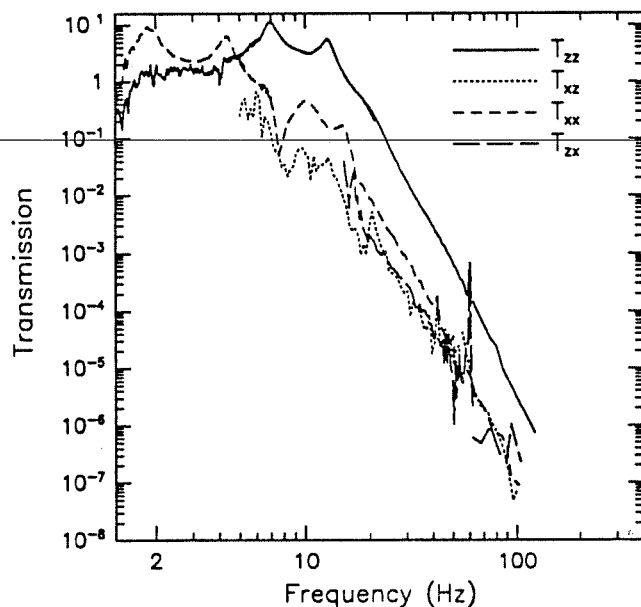
rigid-body modes, which range in frequency from approximately 1.5 to 25 Hz. The configuration we wished to characterize, and the one we modeled on the computer, was with the base fixed to a very large reaction mass. When the stack's base table is placed on springs, as was done for the high-frequency measurements, these low-frequency modes change frequency and shape because the table is a very different reaction mass than the floor-mounted posts. This doesn't greatly affect the high frequency measurements, but would distort any low frequency data taken with the base ungrounded. At frequencies below about 20 Hz, there is sufficient ground noise to drive the stack to measurable levels of excitation when rigidly attached to our vacuum tank mounting posts. Only two transfer functions were taken in this frequency range, the ratio of vertical motion on top to vertical motion at the base, and the same for horizontal motion. These two sets of data approximate T_{zz} and T_{xx} , but do not take into account the contribution of the cross coupling terms on the signal on top. Since we have no easy way of making the measurement with two different drive vectors of ground noise, which is what would be necessary to discriminate the four components, only two traces appear below 20 Hz in the transfer function plot of Stack A, Fig. 2(a). Stack B has somewhat lower normal mode frequencies, and begins to isolate well at lower modal frequencies, as can be seen in Fig. 2(b), so the cutoff for these low-frequency measurements was lower.

3. High-frequency cantilever measurements

In the highest frequency range, above 90 Hz for Stack A, and 60 Hz for Stack B, the stack's high attenuation makes it difficult to take data using the first method. The accelerometers we use (Endevco model 7707-1000) exhibit a slight response to magnetic fields; this becomes important when we wish to measure transmission of 10^{-5} or lower, due to pickup from the motor coils. In addition, the noise floor of our accelerometer amplifiers becomes significant at about this level. We solve this problem by providing mechanical amplification for the accelerometer on the top table, by mounting the accelerometer on the end of an aluminum cantilever. The length (and thus the resonant frequency) is adjusted while under vacuum via remote-control motors. This assembly was mounted on the top table, in place of the simple accelerometer. For each frequency point, the cantilever length was adjusted to the correct length, and clamped. The appropriate drive table shaker was swept in frequency over an interval of approximately 3 Hz around the cantilever resonance, and a transfer function was recorded, with reference to the drive table motion. One such response function appears in Fig. 3. The Q of the cantilever could not be reliably measured at atmospheric pressure (due to sonic coupling and atmospheric drag on the cantilever), so the response as driven through the stack was used to cal-



(a)



(b)

FIG. 2. Measured transmission matrix elements for (a) Stack A, built with all Fluorel springs, and (b), Stack B, built with two lower layers of Fluorel springs and two upper layers of RTV springs. Note that in (b), all transfer function components lie below 3×10^{-6} at 100 Hz.

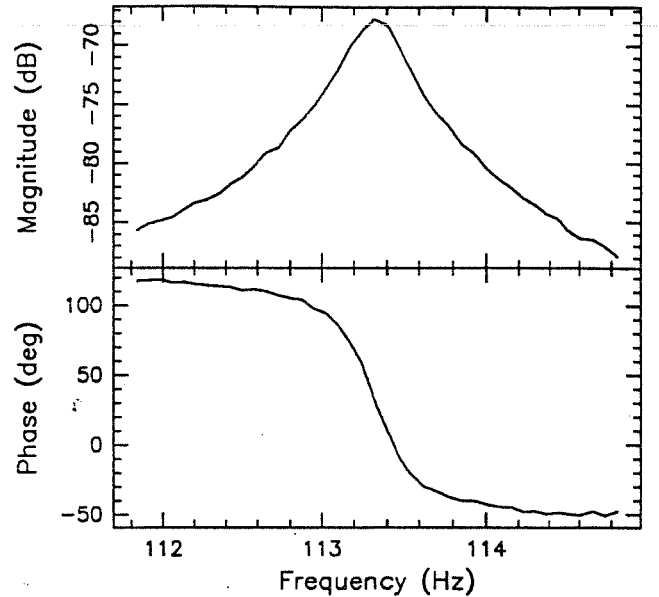


FIG. 3. Transfer function of the signal from the cantilever-mounted accelerometer versus that from the drive table accelerometer. The response closely follows the form of a simple harmonic oscillator at the cantilever oscillator frequency despite the four intervening mass-spring layers.

culate the Q . This Q was taken to be the mechanical amplification factor at the resonance peak. The stack isolation at that frequency was calculated as the measured transfer function of the top accelerometer signal divided by the bottom accelerometer signal, and then divided by the cantilever Q . The accuracy of this procedure was verified by comparison with direct measurements at the lower frequencies. Data were taken at enough points to deduce the stack's response shape, typically 8 for each of the T_{ij} .

C. Summary of measured transfer functions

The largest transmission component in each spring configuration is T_{zz} . After two visible resonance peaks, T_{zz} falls slightly less steeply with frequency than f^{-8} . T_{xx} also appears to have at least two low frequency resonances before dropping at higher frequencies with about the same rate as T_{zz} , displaced downward in magnitude by a factor of about 20. The cross-terms, T_{xz} and T_{zx} , are somewhat more complicated. In Stack A, T_{xz} levels off and then drops suddenly just below 100 Hz, while in Stack B, it has two small-amplitude peaks between 90 and 150 Hz. T_{zz} lurks just below the other components in each case. The rolloff frequencies for Stack B are typically about 2/3 of those for Stack A.

It can be seen that Substituting RTV for the Fluorel in the top layers significantly enhances the isolation, while

only increasing the resonance amplification by a factor of order 2. The peak T_{xx} transmission due to a resonance is 5.3, at 2 Hz for Stack A, and 9.4 at 1.8 Hz for Stack B. T_{zz} peaks at 4.2 at 8.5 Hz in A, and 11.3 at 6.9 Hz for B. This improved isolation is primarily a result of the RTV spring's lower stiffness, rather than its lower loss. The initial deformation under load of the Fluorel, which was mentioned at the end of section II, limited the weight capacity per spring to be about that of the RTV springs despite their higher stiffness.

D. Drift Measurements

The stack exhibits creep under load. To characterize this creep and its temperature dependence, the stack was instrumented with position sensors to measure the distance between the top and bottom plate at three points around the circumference of the stack. Since our tests of the individual elastomers indicate Fluorel would dominate the drift, Stack A was measured. Data were taken for an approximately 10 day period, about 90 days after the initial construction of the stack. The ambient temperature changes, which were recorded as well, were sufficient to allow a robust fit of the data to a sum of a linear drift with time of 1.3×10^{-10} m/sec plus a linear response to temperature of 3.2×10^{-5} m/°C (the stack becomes shorter with increasing temperature) See Fig. 4.

In separate long-term tests of Fluorel under load, we have seen logarithmic drift, which can be expressed as a change in height δh of the stack which evolves with time t as $\delta h = C \log(t)$ with C a constant related to the initial deflection and material properties. Under the assumption that elastomer springs behave this way in the stack, we calculate that the drift after an additional year would be < 2 mm; if the drift rate were constant (the likely worst case) we would accumulate ≈ 4.1 mm/year height change.

IV. FINITE-ELEMENT MODELING AND COMPARISON WITH DATA

A. Pre-experiment model

Our stack design was modeled using a finite element analysis software package. We chose ABAQUS [17], running on MIT's Cray X-MP EA/464. We needed a package which allowed slightly modified versions of a single geometric model to be used to test static stability against buckling and to determine the system's response to dynamic excitation. In addition, we wished to model the rubber with a frequency-dependent complex elastic modulus taken from a lookup table assembled from measured material data.

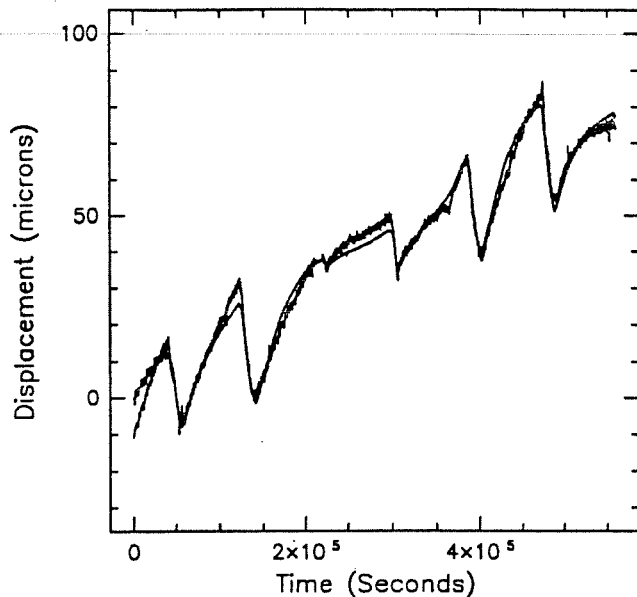


FIG. 4. Drift in the overall height of the stack, data (jagged line) and fit. Daily variations in temperature ($\approx 1^\circ\text{C}$ peak-to-peak) lead to ≈ 25 micron height changes. In addition, over the roughly 7-day period shown, a monotonic shortening of the stack is evident. The fit is described in the text.

A preliminary model was constructed using a geometry slightly different from the stack which we eventually built. The intermediate masses in the legs, as well as the top table, were composed in this model of arrays of quadratically interpolated solid isoparametric elements taken from the ABAQUS element library. A sufficient number of elements were used, 9 each for the intermediate masses, and 81 for the top table, to allow the internal resonances of these parts to influence the stack dynamic response. Because of this, calculations using this model were quite computation intensive.

The results of this preliminary model were the following. The visco-elastic rubber springs damped the rigid-body modes of the stack; most had Q s of less than three. The transfer function component T_{zz} dominated the others for most frequencies above a few hertz. We were convinced that the overall transfer function could be made to meet the isolation specification, with reasonable choices of spring distributions among the layers. The internal resonances of the leg blocks were above the frequencies of interest, so were not studied in detail, but were seen to produce a leveling of the frequency response as they became important. The top table's resonances, which in this model began at a few hundred hertz, resulted in high- Q spikes in the transfer function, only slightly damped by the table's contact with the rubber. With the geometry used, the isolation criteria were not compromised, but it was clear that we must be careful to make a final stack

design with a small and stiff table, so that any resonances occur where there is significant isolation, and with leg elements with resonances well away from the frequencies of interest.

This pre-construction model was also tested for the effects of non-vertical gravity loading, to see if the design was susceptible to toppling. No such instability was found. The gravity loading simulation was also useful, but not necessary, in predicting the percentage compression of the various springs.

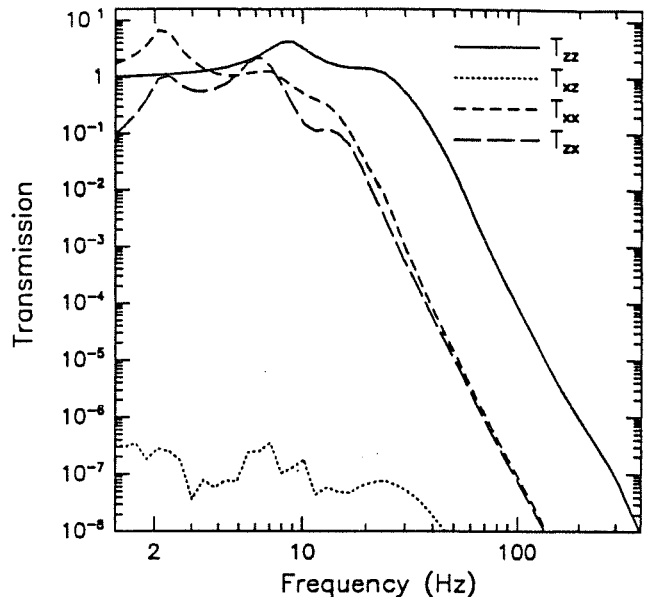
B. Post-experiment model

After the data were taken, we rewrote the ABAQUS code to reflect the geometry, spring placement and properties of the stacks as built. Also, since we had constructed the stacks with structures whose internal resonance frequencies were well above the measured frequencies, this model was written to treat them as nearly rigid bodies. Because of this, the second model required a small fraction of the execution time of the pre-construction model. These after-the-fact predictions are plotted in Fig. 5, and reflect an idealized model in which identical spring elements and identical intermediate mass elements are placed symmetrically below the top table. Also, the bottoms of the bottom springs were mathematically constrained to move together with driven base mass, which eliminates the possible effects of a rocking drive table.

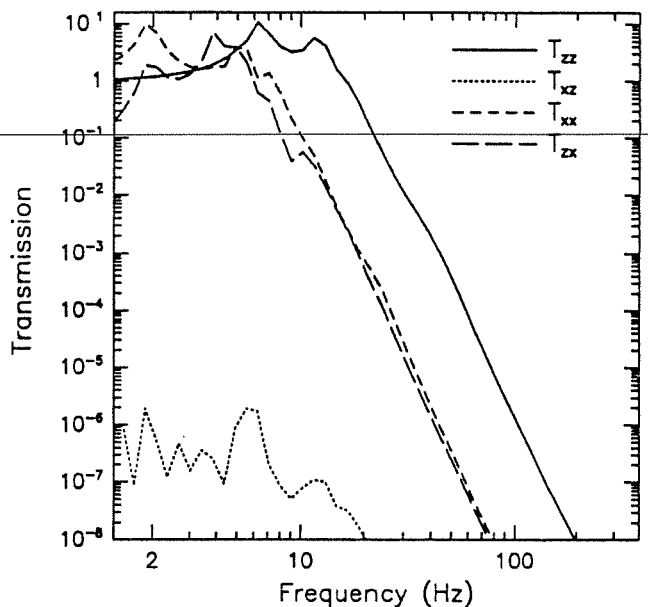
In further simulations, we have attempted to relax these symmetries. These models of imperfections in the system, rather than being useful in exactly duplicating our specific experimental circumstances, which would be nearly impossible, may be used to probe the robustness of such a system to the various defects mentioned. For brevity, we only present these perturbation model results for the Fluorel/RTV stack, Stack B.

1. Stiffness variations

In the symmetric model (Fig. 5), T_{xz} , the modeled coupling of vertical drive to horizontal motion on top, is nearly zero. In the real stacks, slight variations among the springs' stiffnesses break this symmetry. We expect this additional coupling to be larger in the Fluorel springs because some machining had to be done on each spring, and their final sizes varied slightly. The possible effect of this imperfection is modeled by introducing normally distributed Fluorel elastic modulus magnitudes. The predictions of a model with a stiffness standard deviation of 5% are shown in Fig. 6. T_{xz} has become significant. We also tried a standard deviation of 2%, and note that the contribution to T_{xz} is linearly proportional to the standard deviation.



(a)



(b)

FIG. 5. Symmetric ABAQUS model of (a) the all Fluorel (Stack A), and (b) the Fluorel/RTV spring stack (Stack B). This model neglects various imperfections that may exist in the real stack.

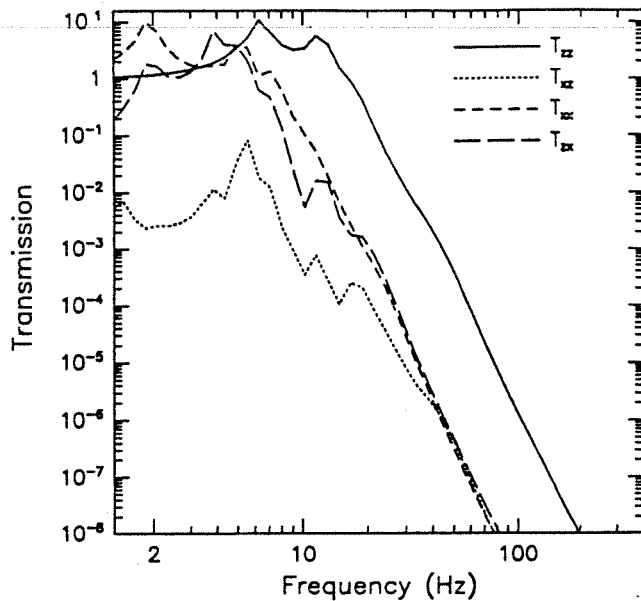


FIG. 6. ABAQUS model of the Fluorel/RTV spring stack (Stack B) with normally distributed spring stiffnesses introduced in the Fluorel stages. The standard deviation is .05 the average stiffness.

2. Response to tilting

Another simplification in the symmetric model is the drive method. The lower table is mathematically constrained not to rock or twist; the nodes at the base of each of the lowest springs move together with a 100 ton reaction mass. A force applied to the reaction mass results in an acceleration of the base nearly perfectly aligned with the force vector. In our lab tests, we measured the response of the base table to the drive motors, and found that a nominally horizontal excitation gave rise to a slight tilting motion (rotation about the x or y axis) of the base table, causing vertical motion at the table edge approximately 10^{-1} of the intended horizontal motion.

We performed a simulation of the effects of pure tilting of the lower stage on the motion above. For this model, the lower faces of the base springs are constrained to lie on a flat, rigid surface which tilts about the x axis in the y direction that lies on the surface with the spring bottoms. We plot two types of response to these conditions in Fig. 7: the coupling of rocking angle, θ , to rocking on the top table, $T_{\theta\theta}$, and the coupling of rocking below to x displacement above, $T_{x\theta}$. $T_{\theta\theta}$ is dimensionless. $T_{x\theta}$ is scaled by 34 cm, the half width of the model's drive table, so that $T_{x\theta}$ multiplied by the z motion resulting from the x shaker drive should give the x motion coupled through this mechanism to the top table.

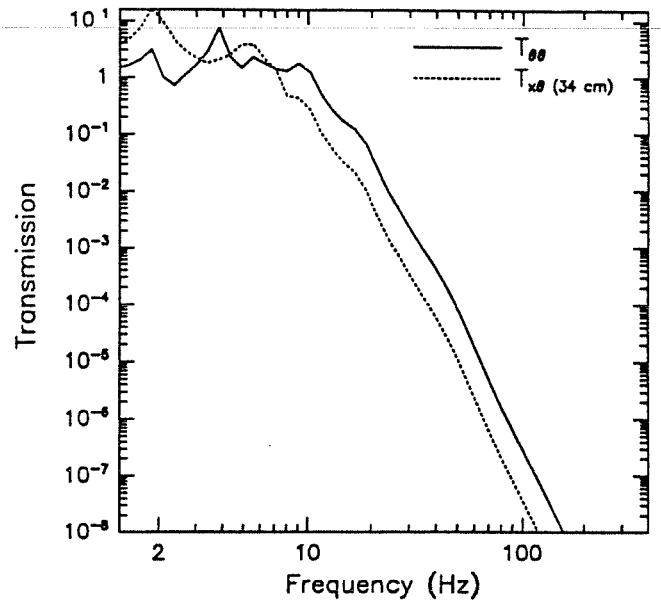


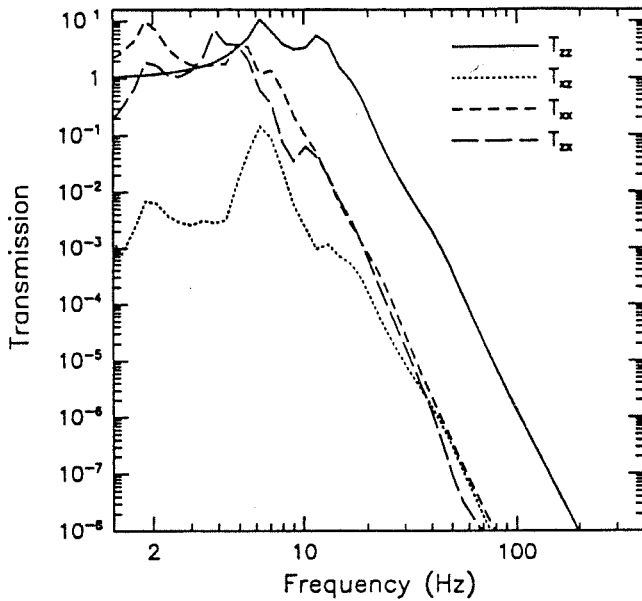
FIG. 7. Stack B ABAQUS model response to pure tilt of the drive table. The two curves represent the coupling to tilt and horizontal displacement, as is explained in the text.

3. Spring alignment precision

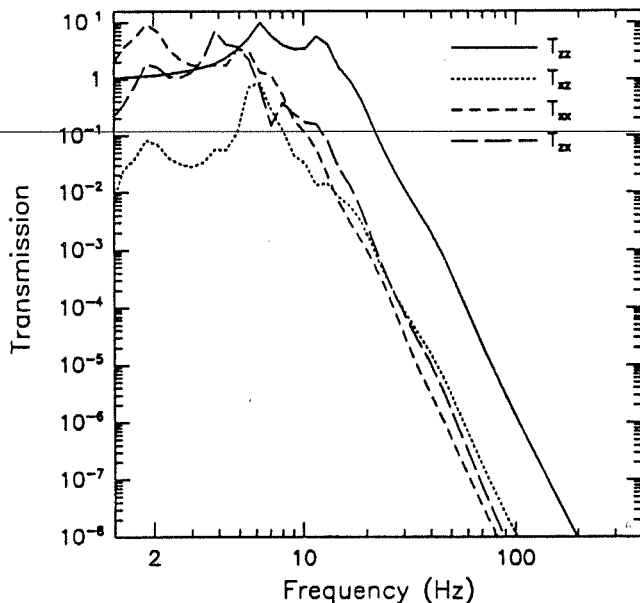
Finally, the symmetric model's fidelity to the stack might be compromised because the individual springs are all mounted in the exact design alignment. In the real stacks, there are variations among the face angles of the Fluorel springs, since one side had to be machined to remove traces of the mounting lug. Also, springs may be horizontally stressed during assembly. These imperfections can result in individual springs cross-coupling x strain to z force and vice-versa.

The simulation of the possible influence of crooked springs was carried out quite differently from the random modulus simulation. Rather than attempt to somehow randomly orient springs, we added one specific cross-coupling spring to each of three of the layers (thus modifying 3 out of 42 springs). These springs had non-zero off-diagonal terms, but zero diagonal ones. That is, these perturbation springs caused a force in the z direction for x or y displacement, and vice-versa, but didn't apply additional forces in the direction of displacement. To see a clear effect, the magnitude of these three perturbation springs' force constants was chosen to be about the same size as the z component of the regular spring's force constant, and all were oriented so that T_{xz} would be enhanced. Fig. 8 shows the stack model's results with these springs added. Two values for the strength of cross coupling are used: .5 and .05 of the regular vertical stiffness.

C. Model agreement with data



(a)



(b)

FIG. 8. Stack B ABAQUS model with extra springs that couple vertical force to horizontal strain and vice-versa. (a) shows results with three cross-coupling springs of strength .05 of the vertical stiffness, and (b) shows the results for .5.

In constructing these finite element models of the LIGO stack prototype, we have the opportunity to evaluate the usefulness of such models in designing seismic isolation stacks. There are four aspects of these models that may offer advantages over analytic modeling. One is the use of a frequency-dependent complex elastic modulus for the spring materials. In the Fluorel, for example, the modulus's imaginary part is of the same order as the real part, so it would be difficult to simulate its properties with some series-parallel combination of springs and dashpots. Another case for which finite element modeling is valuable is the analysis of mechanical systems containing parts with internal normal modes that might affect the overall system response. Third, these models can be very helpful when there are important aspects of the modeled system that are affected by 3D motion. And, finally, we relied on the FE model in testing our design for stability against buckling before actually building it.

The success of the visco-elastic modeling can be judged by how well the vertical-vertical transfer function prediction, T_{zz} , which is less complicated by other effects, matches the data. We need to compare both the Q s of the low-frequency stack modes, which reflect how loss and restoring force compare at the resonance frequencies, and the high-frequency transfer function slope, which reflects the same far above the resonances. The data and models, we believe, agree well over the entire T_{zz} curve.

The second result sought from the FE modeling is a prediction of how the stack transmission is influenced by internal modes in the leg and table elements. The qualitative predictions of the pre-construction models, described above, indicate that the internal modes should not appear in the frequency band of interest; to the extent that no unexplained features were seen, this was verified experimentally. The post-data-taking models, whose results are presented here, were specifically constructed to save computation time by ignoring these internal effects.

The fidelity in three dimensions of the numerical modeling is somewhat more difficult to judge. In the symmetric stack, which consisted of identical springs perfectly aligned, the purely vertical normal modes, which number only 8, are the sole contributors to T_{zz} . An analytic model might be sufficient to understand these. The other transfer functions involve the other 52 modes. In a stack with the symmetry broken with random spring strengths or crooked springs, in general all 60 contribute to each the transfer function components, but to lowest order, the non- T_{zz} components will be most sensitive to the modeling of motions involving all three dimensions.

The transfer function predicted by the symmetric identical-spring model of the mixed-rubber stack differs from the measured data in several ways. T_{zz} is predicted to be zero, as is discussed above. Two of the modeled perturbations, the randomized moduli, and the off-axis

springs, were shown to predict non-zero T_{xz} , although we have not attempted to duplicate the data with some ad hoc combination of these effects. While T_{xx} falls at approximately the same rate at high frequencies as the prediction, it occurs at an overall larger transmission. The crooked spring perturbation can add to T_{xx} but again it is not possible to reconstruct the exact vector contribution in the measured stack without much more detailed measurements. Finally, T_{zz} is lower in the symmetric model than the measured data. The tilt model can be employed to make a plausible explanation of this discrepancy. The horizontal drive motor is known to produce rocking, introducing of order 0.1 of the horizontal motion as vertical motion at the lower table edge. If we multiply the $T_{x\theta}$ curve from Fig. 7 by 0.1, the result would add, with a difficult-to-predict phase, to any measurements of T_{xz} .

The stack showed no signs of instability when the 20% limit on the strain was observed, in agreement with the finite element model. A brief experiment with greater ($\approx 30\%$) loads showed a tendency for the stack to tilt dangerously to one side, probably due to a particularly 'soft' spring element. We believe that the stack as measured is safe and stable.

We have found finite element analysis to be a reasonably inexpensive and fast way to test ideas for mechanical isolation systems. A system which costs thousands of dollars for the steel and spring molding can be pre-tested using a few hours of supercomputer time.

V. SUMMARY AND PLANS

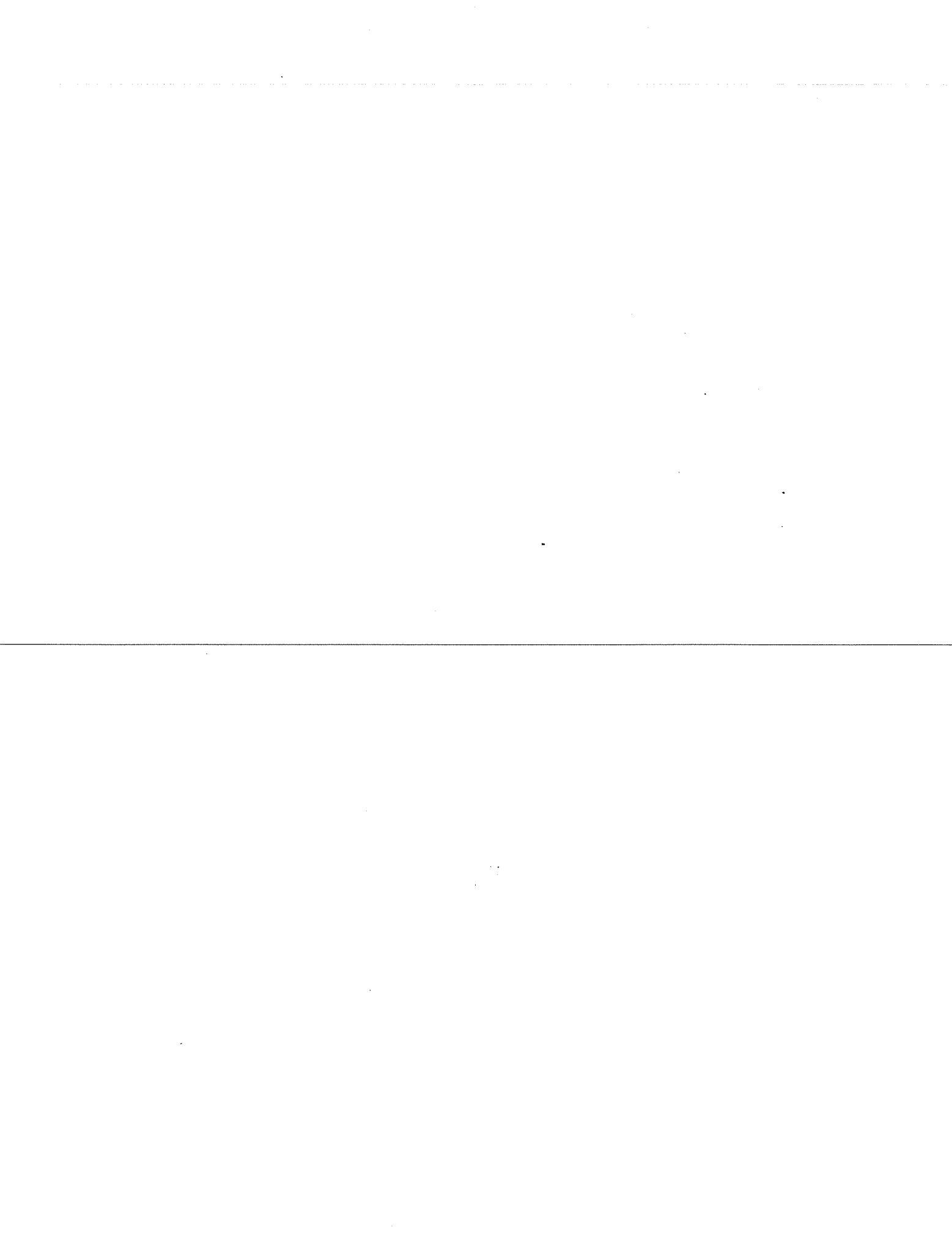
The three choices made in designing a prototype stack for the LIGO project — visco-elastic springs, stiff compact masses, and a separated leg design — are shown to lead to a useful passive seismic isolator. Two workable variations are tested, giving us confidence that this simple design can meet the diverse requirements for the seismic isolation system for the LIGO interferometer. Finite element software is able to predict and explain stack performance, making it a useful tool in the design of these passive seismic isolation system. A stack of this basic design is being incorporated in a LIGO prototype experiment. This will make it possible to test the actual noise spectrum on the top, driven by ground noise, to see if the response is the same for sinusoidal drives of 10^{-6} m , which is what was used for our tests, and $10^{-11} \text{ m}/\sqrt{\text{Hz}}$ random noise, the expected ground excitation at 100 Hz. Any additional noise sources should also be evident.

ACKNOWLEDGMENTS

The authors would like to thank Justin Greenhalgh of Rutherford Appleton Laboratory for discussions and exchanges of stack development results which helped lead

us to this design. We would also like to thank the rest of the LIGO team, especially Rainer Weiss and Stanley Whitcomb, for help in carrying out this work. This research was supported by the NSF grants PHY-8803557 and PHY-9210038.

-
- [1] R. Weiss, Quarterly Progress Report of the MIT Research Laboratory of Electronics **105**, 54 (1972).
 - [2] A. Abramovici, W. Althouse, R. Drever, Y. Gürsel, S. Kawamura, F. Raab, D. Shoemaker, L. Sievers, R. Spero, K. Thorne, R. Vogt, R. Weiss, S. Whitcomb and M. Zucker, *Science* **256**, 325 (1992).
 - [3] C. Bradaschia, R. Del Fabbro, A. Di Virgilio, A. Giazotto, H. Kautzky, V. Montelatici, D. Passuello, A. Brilliet, O. Cregut, P. Hello, C. N. Mann, P. T. Manh, A. Marraud, D. Shoemaker, J. Y. Vinet, F. Barone, L. Di Fiore, L. Milano, G. Russo, J. M. Aguirregabiria, H. Bel, J. P. Duruisseau, G. Le Denmat, P. Tourrenc, M. Capozzo, M. Longo, M. Lops, I. Pinto, G. Rotoli, T. Damour, S. Bonazzola, J. A. Marck, Y. Gourghoulon, L. E. Holloway, F. Fuligni, V. Iafolla, G. Natale, *Nucl. Instrum. Methods Phys. Res.* **A289**, 518 (1990).
 - [4] A. Oliva, V. Sosa, R. de Coss, R. Sosa, N. López Salazar, and J. Peña, *Rev. Sci. Instrum.* **63**, 3326 (1992).
 - [5] R. DelFabbro, A. DiVirgilio, A. Giazotto, H. Kautzky, V. Montelatici, D. Passuello, *Phys. Lett. A* **132** (5), 237 (1988).
 - [6] M. Stephens, P. Saulson, J. Kovalik, *Rev. Sci. Instrum.* **62** (4), 924 (1991).
 - [7] N. Robertson, R. Drever, I. Kerr, J. Hough, *J. Phys. E: Sci. Instrum.*, **15**, 1101 (1982).
 - [8] P. Saulson, *Rev. Sci. Instrum.* **55**, 1145 (1986)
 - [9] D. Shoemaker, R. Schilling, L. Schnupp, W. Winkler, K. Maischberger, and A. Rüdiger, *Phys. Rev. D* **38**, 423 (1988).
 - [10] Interferometer Conceptual Design Handbook, Version 1.0, internal LIGO document.
 - [11] J. Greenhalgh, internal report of the Rutherford Appleton Laboratory, GEO/207/TCG (1990).
 - [12] T. Aldcroft, P. Michelson, R. Taber, and R. McLoughlin, *Rev. Sci. Instrum.* **63** (8), 3815 (1992).
 - [13] E. J. Douze, *Bull. Seism. Soc. Am.* **57** 55-81 (1967).
 - [14] P. Saulson, *Phys. Rev. D* **42**, 2437.
 - [15] A. Abramovici, T. Lyons, and F. Raab, in preparation.
 - [16] These springs were obtained from the Karman Rubber Company, of Akron, Ohio. They used an injection mold from their catalog part number K132, but with 70 durometer Fluorel instead of the neoprene usually used.
 - [17] Finite element analysis program ABAQUS, version 4.9 (Hibbit, Karlsson and Sorenson, Inc., Providence, RI.)



Thermal Noise in the Test Mass Suspensions of a Laser Interferometer Gravitational-Wave Detector Prototype

A. Gillespie and F. Raab

LIGO Project, California Institute of Technology, Pasadena, California, 91125.

Abstract

The thermal noise of the test mass suspensions of a prototype gravitational-wave interferometer was calculated and found to be in agreement with the measured noise near the resonant frequencies of the suspensions. The damping mechanism of the suspension modes was characterized and found to be nearly independent of frequency.

1. Introduction

A Laser Interferometer Gravitational-wave Observatory (LIGO) interferometer [1] consists of a Michelson interferometer with each mirror replaced by a long (4 km) Fabry-Perot optical cavity (see Figure 1). To approximate a free test mass, each mirror of the interferometer is suspended by wires as a pendulum inside of a vacuum vessel. Laser interferometry is used to detect differences between the lengths of the two optical cavities induced by gravitational-waves. The principal sources of noise expected to limit the sensitivity of the interferometer to gravitational-waves are seismic noise that is transmitted to the test masses, photon shot noise (the uncertainty in the measurement of the differential length due to the quantum nature of light), and thermal noise.

Thermal noise in a gravitational-wave detector was first detected in an early resonant-mass detector by Weber [2]. Associated with each mode of oscillation of a physical system in equilibrium with a thermal reservoir is $k_B T$ of thermal energy, of which half will, on average, be kinetic energy and half will be potential energy (k_B and T are Boltzmann's constant and the temperature of the reservoir, respectively). In order to minimize the effects of this thermal noise in a laser interferometer, it is desirable to concentrate the energy in a very narrow frequency band centered on the resonant frequency (that is, to have a large quality factor, Q) of each mode which couples to the motion of the mirrors of the interferometer. These narrow frequency bands can then be filtered out of the gravitational-wave spectrum with negligible loss of observing bandwidth.

The suspension wires of a gravitational-wave detector have several classes of modes which may contribute thermal noise to the interferometer output. We consider here the double wire-loop suspension of the test masses in our 40-meter arm length prototype interferometer [3],

as shown in Figure 2. In the first class are the pendulum modes. These include a motion along the axis of the incident light, a transverse motion, and a torsional mode. In the next class of modes are the vertical spring modes, where each wire may be thought of as a spring. These include a common mode vertical motion of the mass, a tilt mode, and a roll mode. Of these six modes only the pendulum mode, moving along the axis of the light, will produce an interferometer signal directly; the other modes contribute only if the resonant optical mode is misaligned from the central axis of the mirror [4].

In this letter we will concentrate on the modes of the suspension in which the wire vibrates like a violin string, henceforth referred to as "violin modes," investigating their contribution to the thermal noise and their role as a diagnostic for the thermal noise in the pendulum mode. The violin modes have two polarizations per wire. These are weakly coupled to the interferometer output in the sense that there is a large mechanical impedance mismatch between the wires and the test mass, but their resonant frequencies lie in the region of several hundred hertz (an important region of the interferometer's observational bandwidth), making them both a significant source of thermal noise and a diagnostic for the pendulum thermal noise at frequencies far from the pendulum mode's resonant frequencies.

2. Violin Resonances and Thermal Noise

By examining the violin resonances in detail one can probe the specific lineshapes of the resonances and test thermal noise models. A general model to describe damping in a harmonic oscillator is a form of Hooke's law where the spring constant is taken to be complex [5]:

$$F = -k[1 + i\varphi(\omega)]x. \quad (1)$$

F , x , ω and $k[1 + i\varphi(\omega)]$ are the force, displacement, angular frequency and complex spring constant. The specific damping mechanism is parametrized by the frequency dependence of the imaginary part of the spring constant, $\varphi(\omega)$. Applying the Fluctuation-Dissipation Theorem [6] to this model, a general form for the spectral density of displacement due to thermal noise for a simple harmonic oscillator can be derived [7]:

$$\tilde{x}^2(f) = \frac{4k_B T}{\omega} \frac{k\varphi(\omega)}{(k - m\omega^2)^2 + k^2\varphi^2(\omega)}. \quad (2)$$

m and f are the mass and frequency, respectively; $\tilde{x}(f)$ has the dimensions of distance \cdot Hz $^{-\frac{1}{2}}$.

For the system of a point mass suspended by a single finite mass wire and constrained to move in one dimension (which is mathematically simpler than our four wire system but contains the relevant modes), there are a large number of modes which contribute to thermal noise. The thermal fluctuations of the point mass can be described by a multimode expansion [7,8]:

$$\tilde{x}^2(f) = \sum_n \frac{4k_B T}{\omega\mu_n} \frac{\omega_n^2\varphi_n(\omega)}{[(\omega_n^2 - \omega^2)^2 + \omega_n^4\varphi_n^2(\omega)]}. \quad (3)$$

ω_n is the angular resonant frequency of the n^{th} mode; μ_n is the corresponding reduced mass. μ_n is approximately equal to m , the mass, for the pendulum mode ($n = 0$), and $\frac{m}{2}\left(\frac{\omega_n}{\omega_p}\right)^2$ for the violin modes ($n > 0$); ω_p is the pendulum angular resonant frequency. For the remainder of this section we will discuss the violin modes; the pendulum mode will be discussed in Section 4.

It is instructive to examine this model for the familiar case of viscous damping (where the damping acceleration is proportional to the velocity with a proportionality constant γ), commonly used to describe mechanical systems damped by external forces, such as in eddy current damping of moving conductors or as in gas damping of a pendulum. In this case $\varphi_n(\omega) = \gamma\omega/\omega_n^2$ and the resulting lineshape of the n^{th} mode is

$$\tilde{x}_n^2(f) = \frac{4k_B T}{\mu_n} \frac{\gamma}{(\omega_n^2 - \omega^2)^2 + (\omega\gamma)^2}. \quad (4)$$

A damping mechanism which may be appropriate for the violin modes in a gravitational-wave interferometer corresponds to φ_n being independent of the frequency [9]. We add the assumption that the damping mechanism is the same for each violin mode, which we believe to be approximately true in the case of the harmonics of a thin violin wire. "Thin" means that the potential energy stored in the bending of the wire along its length is negligible compared to the energy in the bending at the endpoints and in the tension of the wire. In the case of a thin wire, the distribution of energy between bending near the ends and tension is the same for all harmonics, and therefore

the damping, if its origin is internal to the wire, ought to be the same. In this case, $\varphi = 1/Q$ is the mechanical quality factor of a violin mode; all violin modes have the same Q and the thermal noise lineshape is

$$\tilde{x}_n^2(f) = \frac{4k_B T}{\omega\mu_n} \frac{\omega_n^2/Q}{[(\omega_n^2 - \omega^2)^2 + \omega_n^4/Q^2]}. \quad (5)$$

Notice that when ω is near a particular ω_n the two lineshapes given by formulae (4) and (5) are approximately equal ($Q_n = \omega_n/\gamma$ for viscous damping). In fact in the limit that Q_n becomes very large, all lineshapes converge to the same shape near ω_n for any choice of $\varphi_n(\omega)$ which varies smoothly over the bandwidth ($\Delta\omega = \omega_n/Q_n$) of the system. With the 40-meter interferometer the thermal noise of the violin modes dominated other noise only in a narrow band centered on the violin resonance frequencies, and therefore the noise spectrum of the interferometer did not directly indicate the thermal noise lineshapes or the nature of the damping mechanism. However the Q 's of the lower few harmonics of the violin modes could be measured; by examining the frequency dependence of the Q 's of those harmonics, one can assign some frequency dependence to φ .

3. Measurements on the 40-m Interferometer

The Q 's of individual suspension wires in the 40-m interferometer were measured by exciting the violin resonance, turning off the excitation, and measuring the decay times ($Q_n = \omega_n\tau/2$; τ is the measured amplitude decay time). Magnets and actuator coils were attached to the end test masses (shown in Figure 2) for applying calibration signals and to maintain resonance between the cavities and the light. On all masses a piezoelectric transducer was normally used to damp the residual pendulum motion. For measurements on the end masses the driving signal was applied to the actuator coils. The vertex masses were driven using the damping transducers on their control blocks. To verify that neither the pendulum damping transducers nor the interferometer control servomechanisms damped the wire resonances, the decays were measured with and without servomechanism signals applied to the actuators.

The frequencies and Q 's of the fundamental violin modes of the suspension systems of the 40-meter interferometer are given in Table 1. The uncertainties in the Q measurements are approximately 10%. The differences in frequencies among the different masses are explained by differences in the suspensions (which arose through various modifications to the interferometer). One end mass (E1) uses 150 μm -diameter wire. The other end mass (E2) uses 100 μm -diameter wire. Both of the vertex masses use 75 μm -diameter wire. Steel music wire is used for all masses; the length of all of the suspension wires is 25 cm, and each test mass is 1.5 kg. For a

thin wire the resonant frequency of the n^{th} mode is given by $f_n = n/ld \times \sqrt{T/\pi\rho}$, where l and d are the length and diameter of the wire, T is the tension, and ρ is the density of the wire material.

The differences in the Q's of the violin modes for the different masses might partly depend on the wire diameters, which affect both the tensile stress and the stiffness of the wires. However there were also significant variations in the connections of the wires to the masses. In all cases a small glass wedge was used to define the point where the wire connects to the test mass, and a similar metal wedge was used where the wire meets the control block. Unfortunately fine details (such as how the wedges and wires were bonded to the mass) varied among the wires. Furthermore, the end masses and the vertex masses had different types of control blocks, for historical reasons.

The Q's of the second harmonics of 5 wires were measured and are also shown in Table 1—two wires from E1, two wires from E2 including both a high and a low Q wire, and a high Q wire from the vertex mass V1. In addition two additional higher order harmonics of the V1 wire were measured. The Q's of all harmonics were the same as the corresponding fundamental resonance Q within 25%. This result is consistent with a damping model which is independent of frequency in the range of hundreds of hertz. We will adopt this model for the remainder of this letter.

4. Estimate of the Damping and Noise of the Pendulum Mode

A full description of the noise of the suspension must include the thermal noise from the pendulum mode. Due to the impedance mismatch between the wires and the test mass, the violin resonances contribute to the overall noise spectrum only in narrow bands (tenths of hertz) centered at their resonant frequencies. The thermal noise of the pendulum mode, which couples directly to the interferometer output, can be the principal noise at frequencies of order 100 Hz, a region of peak interest for LIGO interferometers. Predicting this thermal noise requires knowing the damping of the pendulum mode, $\varphi_p(\omega)$, at these frequencies. Since direct measurement of the losses of a high Q mechanical system far from its resonant frequency can be extremely difficult [5], we use the Q's of the violin modes to estimate the damping of the pendulum at frequencies of hundreds of hertz.

If we assume that all of the losses in both the pendulum and the violin modes are concentrated near the endpoints of the wire, where the bending is most severe, we can estimate the pendulum damping directly from the violin damping. These endpoint losses need not be restricted to intrinsic bending losses in the wire itself, but may also include losses due to flexing or friction in the clamps or the points of attachment at either the top or the bottom of the wire. The model only requires that the

losses be associated with the motion of the wire in the region near the clamping through some angle θ from the vertical equilibrium position. This calculation assumes that there is some loss of energy per cycle $\Delta E(\theta)$ whenever the wire is bent through some angle θ . The strategy is to calculate the total energy of both the pendulum (E_p) and the violin (E_v) modes as functions of θ , and by comparing $E_p(\theta)/\Delta E(\theta)$ with $E_v(\theta)/\Delta E(\theta)$ to deduce the relationship between their respective damping.

The energy in the pendulum mode is, to second order in θ ,

$$E_p(\theta) \approx mgl \frac{\theta^2}{2}. \quad (6)$$

g is the acceleration due to gravity and l is the equilibrium length of the loaded wire. If we approximate the wire as having no stiffness, which is reasonable for the parameters of the 40-meter interferometer test mass suspensions as far as the total energy of the lower order violin modes is concerned, the potential energy of the violin modes is stored in the tension of the wire, and the shape of the modes is sinusoidal. In this case, the energy of the violin mode is, to second order in θ ,

$$E_v(\theta) \approx Tl\theta^2/4. \quad (7)$$

T is the tension of the wire. This result is independent of which harmonic is chosen. The pendulum has the same amount of energy at a given angle regardless of the number of wires. Since each wire in a four wire system is only supporting one quarter of the mass, the tension of each wire in our system is $mg/4$, and $E_v = mgl\theta^2/16$. Therefore for a given angle θ , the pendulum mode has 8 times as much energy as a violin mode, $E_p = 8E_v$.

For the violin modes, the loss of energy per cycle, ΔE_v , is given by

$$\Delta E_v(\theta) = 2\pi E_v(\theta)\varphi_v. \quad (8)$$

If the losses for both the violin mode and the pendulum mode are primarily in the bending of the wire, then the losses in the pendulum would equal the losses in the four wires :

$$\Delta E_p(\theta) = \Delta E_{v1}(\theta) + \Delta E_{v2}(\theta) + \Delta E_{v3}(\theta) + \Delta E_{v4}(\theta). \quad (9)$$

We have assumed that the mass is constrained by the four wires so that it does not rotate and the wire bends at both ends in the pendulum mode. We can then estimate the damping of the pendulum as

$$\varphi_p = \frac{1}{8}(\varphi_{v1} + \varphi_{v2} + \varphi_{v3} + \varphi_{v4}). \quad (10)$$

With this estimate of the damping, the thermal noise due to the pendulum mode at frequencies near the violin

mode resonant frequencies can be derived by substituting $\varphi(\omega) = \varphi_p$ into the general thermal noise lineshape [equation (2)], giving:

$$\hat{x}_p^2(f) = \frac{4k_B T}{m\omega} \frac{\omega_p^2 \varphi_p}{(\omega_p^2 - \omega^2)^2 + \omega_p^4 \varphi_p^2}. \quad (11)$$

This result depends on the wires being sufficiently thin that essentially all of the bending occurs near the ends, an approximation which is true for the physical parameters of this prototype interferometer. LIGO interferometers will use larger masses which will require correspondingly thicker wires; these wires may have non-negligible stiffness. In this case a more detailed analysis treating the finite stiffness of the wire is required, but the principle of estimating the total thermal noise of the suspension system from the Q's of the violin modes can still be applied [10].

5. Comparison of Estimated Suspension Thermal Noise with Experiment

The lineshapes of the violin resonances of mass E1 were compared with the thermal noise prediction. The thermal noise lineshape of a pendulum with a finite mass single wire is given in equation (3). For a four-wire system the lineshape of an individual violin mode becomes

$$\hat{x}_n^2(f) = \frac{2k_B T}{\omega m} \frac{\omega_n^2/Q}{(\omega_n/\omega_p)^2 [(\omega_n^2 - \omega^2)^2 + \omega_n^4/Q^2]}. \quad (12)$$

This comparison is shown in Figure 3. Next to two of the resonances are smaller peaks. We believe that they are polarization modes of the wires which are nearly but not completely orthogonal to the optical axis. A finer comparison between theory and experiment is given in Figure 4 where the data points (for the middle resonances in Figure 3) are plotted on a linear scale with their associated error bars. The uncertainties in the data points are statistical errors due to the limited number of averages in the power spectrum. The systematic uncertainty of the calibration is 10%. The uncertainty in the theoretical curve due to the uncertainties in the Q's is smaller. The agreement with the thermal noise calculated using the measured resonant frequencies and Q's is quite good. The predicted rms fluctuation of the test mass corresponding to a single violin resonance is about 0.06 fm.

Using the measured Q's and assuming that the pendulum mode is damped as derived above, the total thermal noise of the wire suspensions can be predicted:

$$\hat{x}^2(f) = \sum_{4 \text{ masses}} \left[\hat{x}_p^2(f) + \sum_{4 \text{ wires}} \sum_n \hat{x}_n^2(f) \right]. \quad (13)$$

Figure 5 shows this thermal noise prediction and compares it to the measured interferometer noise of June 1992. As can be seen from the figure, thermal noise contributed to the 40-meter interferometer by the suspension wires is much smaller than other noise sources except in narrow frequency bands centered on the resonant frequencies of the violin modes. The increase in the predicted suspension noise below 200 Hz is due to the pendulum mode. The resonances near 320 Hz are excited above thermal noise by a factor of two by excess noise in the current version of the pendulum damping control electronics; when that control system is turned off (which degrades the overall performance of the interferometer) those peaks are at thermal noise (see Figure 3). The peaks in the noise between 1800 and 2000 Hz which appear to coincide with the violin resonances are due to residual frequency noise from the laser, not due to the violin resonances.

6. Conclusion

We have observed thermal noise of the violin modes near resonance in a 40-meter interferometer. We have used the measured Q's of the harmonics of the violin modes to conclude that the primary damping mechanism of the violin modes is frequency independent. Taking that conclusion and the assumption that the losses in the suspension occur primarily near the endpoints of the wires, we have estimated the total suspension thermal noise spectrum in the region of hundreds of hertz of the LIGO 40-meter prototype interferometer.

The estimated suspension thermal noise background for the 40-m interferometer was dominated by the low Q wires. Our data indicate that wire Q's of at least 3×10^5 are achievable using the basic design of the current suspension. If this Q were achieved on all wires, the resulting thermal noise would be $\sim 2 \times 10^{-19} \text{ m}/\sqrt{\text{Hz}}$ at 100 Hz, comparable to the goal for initial LIGO interferometers [1]. Understanding the variations in the wire Q's and the scaling with tension and wire diameter is the subject of an ongoing investigation. Similar studies can be used to characterize the expected thermal noise from candidate suspension materials which have shown much higher Q values in low frequency oscillators [11].

Acknowledgments

We thank R. Vogt and the entire LIGO team for making this work possible. We are especially grateful to P. Saulson, R. Weiss and S. Whitcomb for stimulating conversations and M. Zucker and S. Kawamura for their help in setting up the measurements. This work was supported by the National Science Foundation cooperative agreement number PHY-9210038.

References

- [1] A. Abramovici, W.E. Althouse, R.W.P. Drever, Y. Gursel, S. Kawamura, F.J. Raab, D. Shoemaker, L. Sievers, R.E. Spero, K.S. Thorne, R.E. Vogt, R. Weiss, S.E. Whitcomb, and M.E. Zucker, *Science* 256 (1992) 325.
- [2] J. Weber, *Phys. Rev. Lett.* 17 (1966) 1224.
- [3] M.E. Zucker, in: *Proc. of the sixth Marcel Grossman meeting on general relativity*, ed. H. Sato (World Scientific, London, 1993) Vol. 1 p. 224.
- [4] S. Kawamura and M.E. Zucker, *Mirror orientation noise in a Fabry-Perot interferometer gravitational wave detector*, (1993), private communication.
- [5] A.S. Nowick and B.S. Berry, *Anelastic relaxation in crystalline solids* (Academic Press, New York, 1972).
- [6] H.B. Callen and T.A. Welton, *Phys. Rev.* 83 (1951) 34.
- [7] P. Saulson, *Phys. Rev. D*, 42 (1990) 2437.
- [8] N. Mio, *Jpn. J. Appl. Phys.* 31 (1992) 1243.
- [9] J. Kovalik and P. Saulson, *Mechanical loss in fibers for low noise pendulums*, (1993), private communication.
- [10] G. Gonzalez and P. Saulson, *Brownian motion of a mass suspended by an anelastic wire*, (1993), private communication.
- [11] V.B. Braginsky, V.P. Mitrofanov, O.A. Okhrimenko, *Phys. Lett. A* 175 (1993) 82.

Figure Captions

Figure 1

A schematic view of a LIGO interferometer. E1 ("end mirror 1"), E2, V1 ("vertex mirror 1"), and V2 are arbitrary labels for the four mirrors.

Figure 2

Test mass suspension details.

Figure 3

E1 Violin Resonances. The solid line is the interferometer noise spectrum; the dashed line is the thermal noise prediction. The large peak at 327.5 Hz is a calibration signal. The thermal lineshape has been averaged over each 0.025 Hz bandwidth channel to produce the prediction.

Figure 4

This spectrum is an expansion of Figure 3 plotted on a linear scale to emphasize the peaks and show the detail.

Figure 5

The solid line is the interferometer noise; the dashed line is the thermal noise prediction. The data were taken at two different bandwidths: 1.25 Hz from 100 to 1000 Hz, and 6.25 Hz from 1000 to 2000 Hz. The thermal noise prediction was generated by averaging the lineshape over the appropriate bandwidth. Due to this averaging the violin modes appear broadened.

Table 1: The measured Q's of the violin resonances

Test Mass	Frequency (Hz)	Q	Q of n th Harmonic; n
E1	319.65	13,000	
	324.90	16,000	19,000; 2
	326.08	19,000	
	328.45	15,000	16,000; 2
V1	594.35	240,000	
	596.68	280,000	260,000; 2 220,000; 3 220,000; 4
	598.15	43,000	
	605.02	110,000	
E2	505.85	66,000	
	506.88	120,000	110,000; 2
	512.85	23,000	23,000; 2
	514.90	16,000	
V2	592.70	295,000	
	592.80	295,000	
	596.42	356,000	
	600.22	163,000	

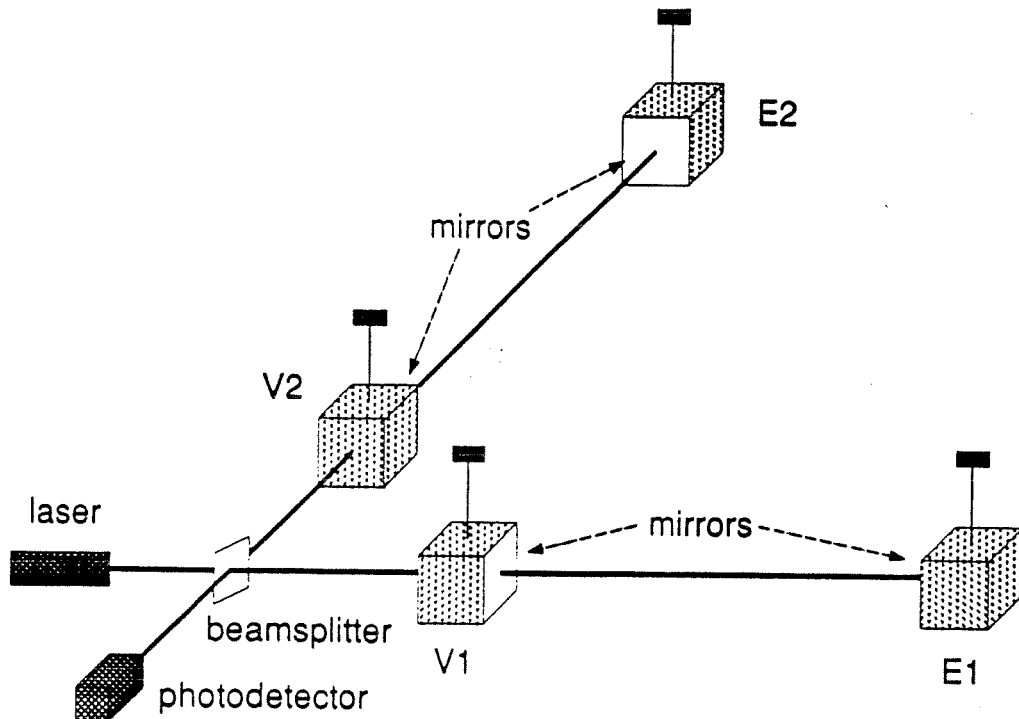


Figure 1

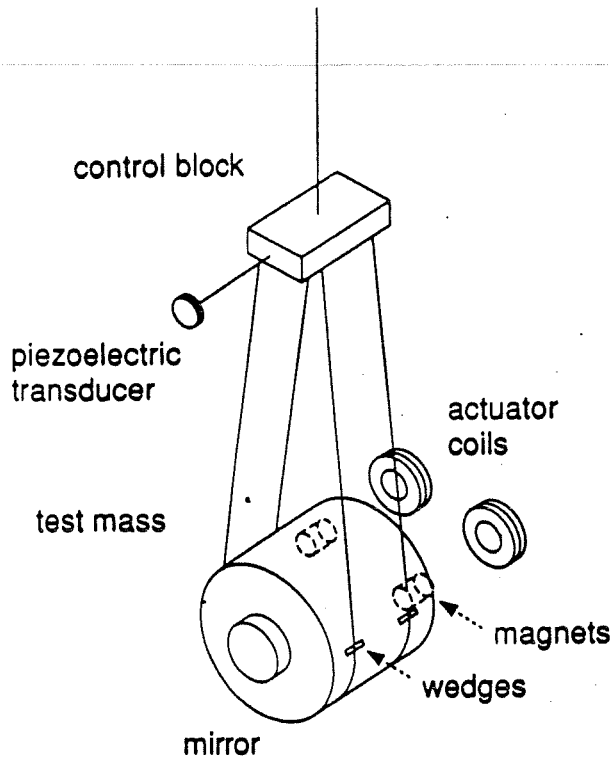


Figure 2

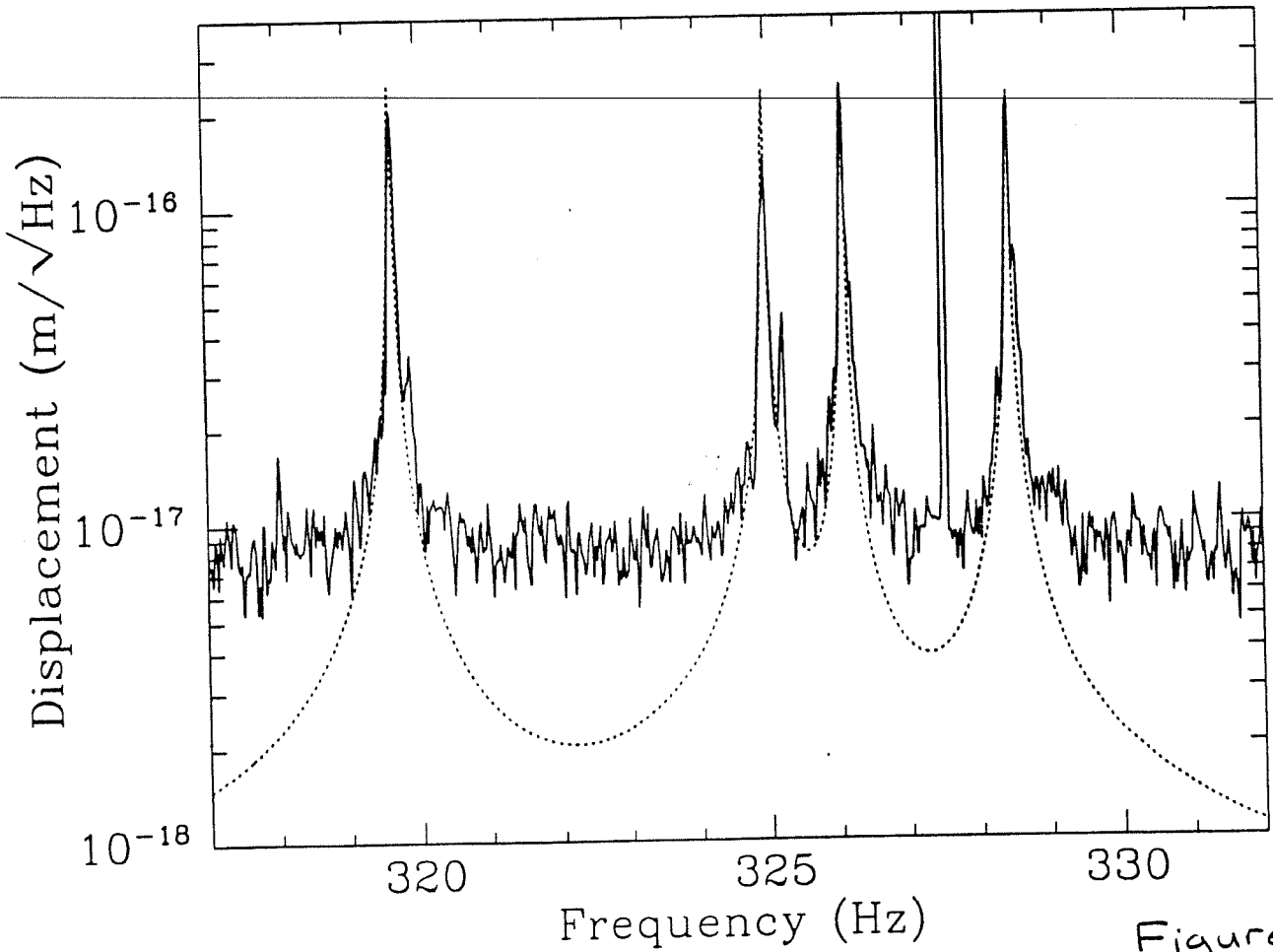


Figure 3

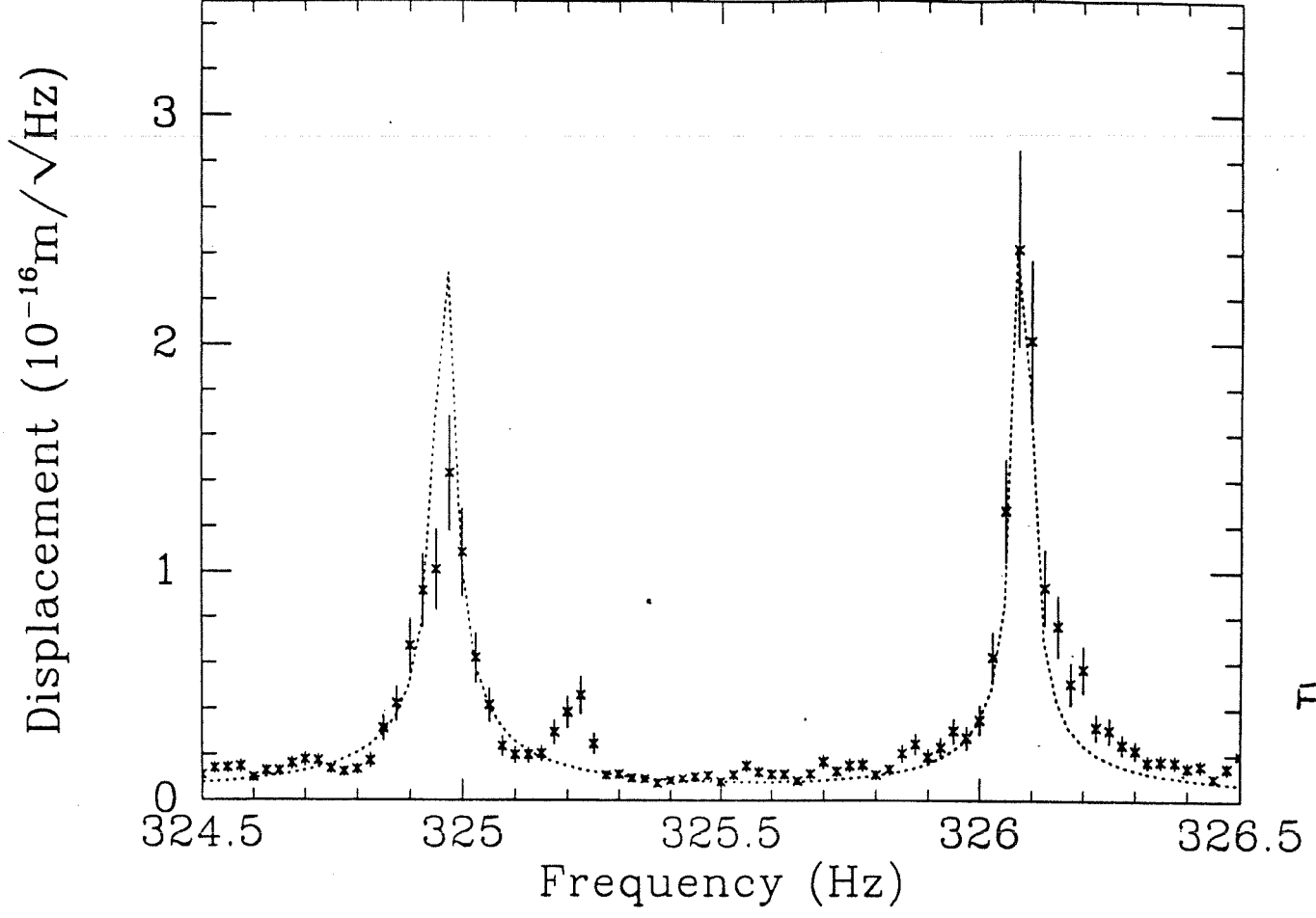


Figure 4

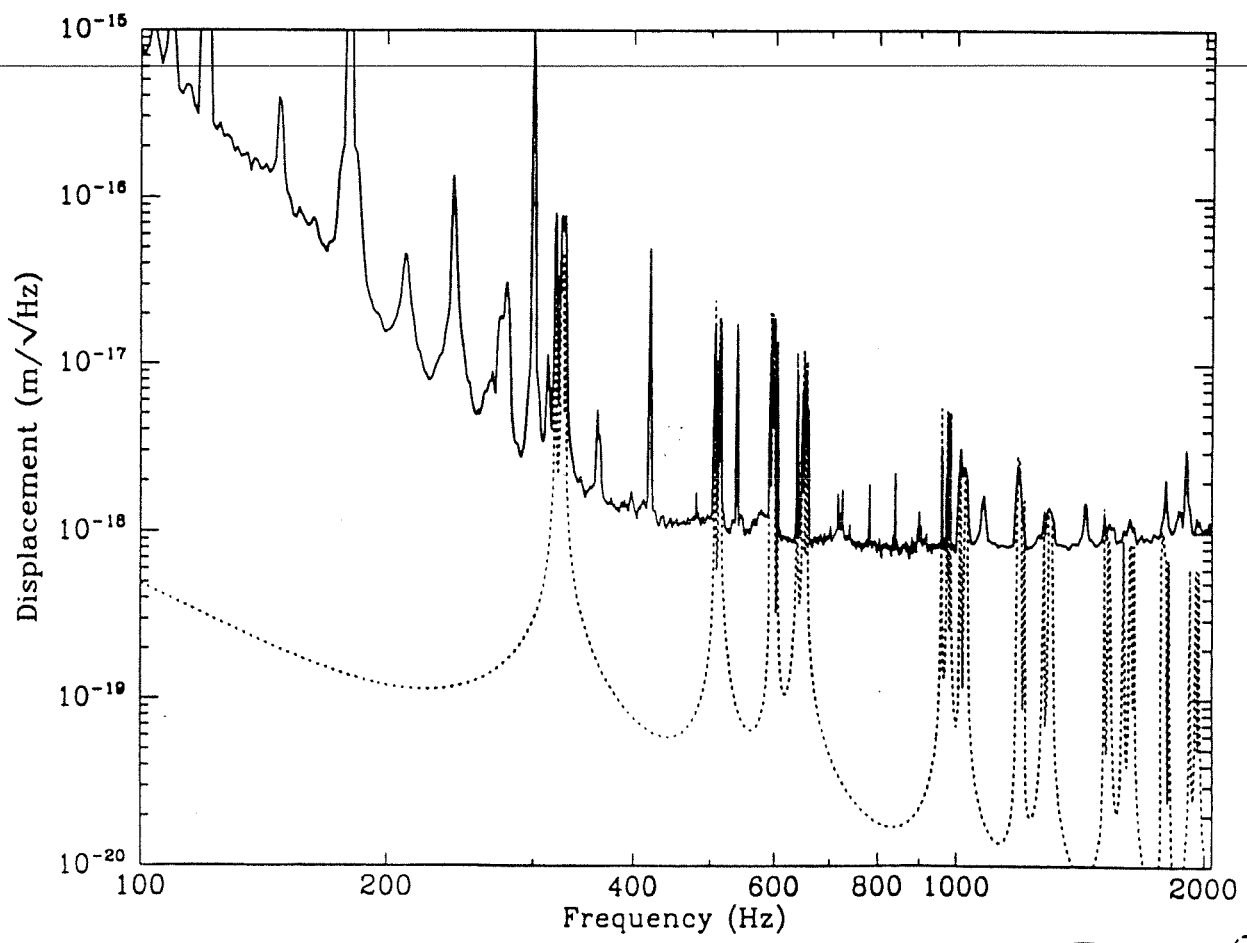


Figure 5